On the Growth of Semiconductor-Based Epitaxial and Oxide Films from Low Energy Ion Beams

by
Olivier P.J. VANCAUWENBERGHE

Ingénieur en Sciences des Matériaux
Université Catholique de Louvain
(1987)

Submitted to the Department of
Materials Science and Engineering
in Partial Fulfillment of the Requirements for the Degree of

DOCTOR OF PHILOSOPHY
in Electronic Materials

at the
MASSACHUSETTS INSTITUTE OF TECHNOLOGY
February 1992

Signature redacted
Signature of Author ....
Department of Materials Science and Engineering
Janurary 10, 1992

Signature redacted
Certified by ....
Nicole HERBOTS
Assistant Professor, Electronic Materials
Thesis Supervisor

Signature redacted
Accepted by ....
Linn W. HOBBS, Chairman
Departmental Committee on Graduate Students
Department of Materials Science and Engineering

On the Growth of Semiconductor-Based Epitaxial and Oxide Films from Low Energy Ion Beams

by

Olivier P.J. VANCAUWENBERGHE

Submitted to the Department of Materials Science and Engineering on January 10, 1992 in partial fulfillment of the requirements for the degree of Doctor of Philosophy in Electronic Materials

ABSTRACT

Ion Beam Deposition (IBD) is a low temperature growth technique where a thin film is grown directly from a low energy ion beam (< 1 keV). Through atomic collisions, the atomic mobility and chemical reactivity are athermally enhanced, allowing epitaxial growth and compound formation by IBD to occur at low temperatures. In this work, several aspects of IBD growth of semiconductor-based epitaxial and oxide layers are investigated both theoretically and experimentally.

Epitaxial growth by IBD is modeled in a continuum model (DRIVIC) taking into account the ion-solid interactions and the thermal diffusion and recombination of point defects. Simulation results for IBD of Si on Si show that a model including mobile interstitials can account for various experimental observations specific to IBD growth and establish an upper limit for the ion energy to achieve epitaxial growth by IBD, which is a function of the point defect diffusivities. Monte-Carlo simulations of IBD of Si on Si are also performed and give an atomistic picture of the IBD epitaxial process which agrees with the predictions of the continuum model DRIVIC.

Low energy Ion beam Oxidation (IBO) of Si, Ge, $Si_{1-x}Ge_x$ and GaAs at room temperature is investigated experimentally as a function of ion energy from 100 eV to 1 keV. We report for the first time the formation by IBO of new SiGe-dioxide layers. The results show that properties of the IBO films, such as phase formation, stoichiometry, thickness, and interface width, are strongly dependent on the ion energy.

In order to explore the kinetics of IBO and to account for the observed relationship between ion energy and films properties, computer models of IBO are developed taking progressively into account oxygen incorporation and sputtering (model IS), ion beam mixing (ISR), and oxygen diffusion (ISRD). The simulation results with the three models highlight the role of each phenomena in the IBO process and show that experimental observations such as growth stages, film thickness and interface width, can be accurately accounted for only by the complete model ISRD including oxygen diffusion.

Similarities are then pointed out between epitaxial growth by IBD and oxide layer formation by IBO in terms of the importance of using low energies and the role played by the point defect creation, diffusion and annihilation.

We conclude by presenting the electrical characterization of a first MOS test circuit using the IBO Si- and SiGe-dioxide films as the gate dielectric.

Thesis Supervisor: Dr. Nicole HERBOTS
Title: Assistant Professor of Electronic Materials

TABLE OF CONTENTS

LIST OF FIGURES

LIST OF TABLES

LIST OF PUBLICATIONS

This thesis is partially based on the following publications:

Chapter 3 and 4.

- "Semiconductor-Based Heterostructure formation using Low Energy Ion Beams: Ion Beam Deposition (IBD) & Combined Ion and Molecular Beam Deposition (CIMD)", N. Herbots, O.C. Hellman, P.A. Cullen, O. Vancauwenberghe, in DEPOSITION AND GROWTH: LIMITS FOR MICROELECTRONICS, American Vacuum Society Series **4**, 259 (1988).
- "The Role of Point Defect Diffusion and Recombination in Low Temperature Growth of Semiconductor Heterostructures using Low Energy Ion Beams", O. Vancauwenberghe, N. Herbots, O.C. Hellman, in GROWTH OF SEMICONDUCTOR STRUCTURES AND HIGH T_C THIN FILMS ON SEMICONDUCTORS, SPIE Proceedings vol. **1285**, 47 (1990)
- "Atomic Collisions, Elastic Recombination, and Thermal Diffusion during Thin Film Growth from Low Energy Ion Beams", N. Herbots, O. Vancauwenberghe, O.C. Hellman, Y.C. Joo, Nuclear Instruments and Method **B59/60**, 326 (1991)
- "A Quantitative Model of Point Defect Diffusivity and Recombination in Ion Beam Deposition (IBD) and Combined Ion and Molecular Deposition (CIMD)", O. Vancauwenberghe, N. Herbots, O.C. Hellman, J. Vac. Sci. Technol. **B9**, 2027 (1991)

Chapter 5

- "Oxides and Nitrides of metastable group IV alloys and nitrides of group IV elements and semiconductor devices formed thereof", N. Herbots, O.C. Hellman, O. Vancauwenberghe, U.S. Patent pending (April 29, 1991)
- "New SiGe Dielectrics Grown at Room Temperature by Low Energy Ion Beam Oxidation (IBO) and Nitridation (IBN)", O. Vancauwenberghe, O. C. Hellman, N. Herbots, W.J. Tan, to appear in the October 21, 1991 issue of Applied Physics Letters

- "Room Temperature Nitridation and Oxidation of Si, Ge and MBE-grown SiGe Using Low Energy Ion Beams (0.1 - 1 keV)", O. Vancauwenberghe, O.C. Hellman, N. Herbots, J.L. Olson, W.J. Tan, and W.J. Croft, accepted for publication in LOW ENERGY ION BEAM AND PLASMA MODIFICATION OF MATERIALS, Mater. Res. Soc. Proc. Vol. **223** (1992)
- "Comparative study of low energy ion beam oxidation of Si (100), Ge/Si (100) and $Si_{1-x}Ge_x$/Si (100)", O. Vancauwenberghe, O.C. Hellman, N. Herbots, W.J. Tan, J.L. Olson, W.J. Croft, accepted for publication in Mat. Sci. Eng. B
- "Formation of Metastable SiGe-Oxide Films by Direct Low Energy Ion Beam Oxidation", O. Vancauwenberghe, O.C. Hellman, N. Herbots, W.J. Tan, J.L. Olson, R.J. Culbertson, W.J. Croft, accepted for publication in Nucl. Instrum. Meth. B
- "Ion Beam Oxidation of GaAs: the Role of Ion Energy", O. Vancauwenberghe, N. Herbots, H. Manoharan, M. Ahrens, J. Vac. Sci. Technol. **A9**, 1035 (1991)

Chapter 6:

- "The role of ion energy in ion beam oxidation of semiconductors: experimental study and model", O. Vancauwenberghe, O.C. Hellman, N. Herbots, paper to be presented at the 38th Annual AVS Conference, Seattle, Washington, November 11-15, 1991, in preparation for J. Vac. Sci. Technol. A

Chapter 8:

- "Thin oxides of Si and $Si_{0.8}Ge_{0.2}$ grown by low energy ion beam oxidation: experimental study and applications", O. Vancauwenberghe, M.F. Lu, N. Herbots, paper to be presented at the 38th Annual AVS Conference, Seattle, Washington, November 11-15, 1991, in preparation for J. Vac. Sci. Technol. A

ACKNOWLEDGEMENTS

All along my Ph.D., Christel, my wife, was always present to encourage me and to help me as much as she could. It was not always easy on her, but she showed a lot of patience, and I especially thank her for that.

My advisor, Professor Nicole Herbots, gave me the unique opportunity to conduct an exciting research and to manage the exceptional CIMD laboratory. Her inputs in the realization of the experiments, the papers and the present thesis were always the most helpful and welcome. She also never hesitated to send me to conferences that were really useful in gaining scientific knowledge and professional experience. For all these reasons, I want to express to her my deepest gratitude.

Nicole had a nice little group with wonderful people: Olof Hellman, David Eng and Pat Cullen, without forgetting her secretary, Amy Sklivas. They were always ready to help and contributed to a good atmosphere for working at M.I.T. I want to thank more particularly Olof for the characterization of the IBO samples by RBS and TEM and his occasional help in the CIMD lab, and David for his useful discussions and support.

The undergraduate students who joined temporarily the research did also a wonderful job that I really appreciate. Betsy Srichai, Wee-Jyn Tan, and Desmond Lim worked for their UROP project a lot more than required. John Olson and Mike Ahrens performed for their Senior thesis a research of excellent quality. Last but not least, Hari Manoharan and Michael Thayer took advantage of their (prestigious) MPC summer fellowship to contribute significantly to the setting-up of the CIMD laboratory and other aspects of the IBD and MBE research.

Thanks to the time and kindness of Bob Culbertson, Wendy Kosik and Bill Croft at the U.S. Army Materials Technology Laboratory at Watertown, the characterization of the IBO samples was completed by a comprehensive RBS analysis and cross-section TEM observation. More particularly, Bob did a wonderful job in teaching the undergraduate students, Betsy, Hari, and both Mike's, the RBS technique and in helping them in the interpretation of their results. His scientific contribution and technical help were greatly appreciated.

I am also thankful to the members of my thesis committee, Professor L.A. Kolodziejski and Professor R.W. Balluffi, who improved the scientific quality of this thesis by their useful and to the point comments.

Among the M.I.T. staff, I particularly want to thank May Fang Lu who spent a month with me fabricating the SiGe MOS circuit, John Martin and Libby Shaw who made possible the first IBO experiment with GaAs and always provided great help all along these years and especially in the realization of this thesis, and Rich Perrilli and Tim McClure for their help and support.

Being in charge of the CIMD lab got me involved with many technical problems that needed to be fixed quickly. This would not have been possible without the help of the application engineers that I contacted. I want more especially to thank the ESCA customer service of Perkin-Elmer for its great help and quick servicing of the ESCA system, and the team of S.V.T., Peter Chow, Jim Tolan, Dave Seibel and Dana Johnson, as well as Mike Longerbone, for their useful advices and technical "tricks" for running the MBE system.

There were many more other nice people who were available and supportive, both at M.I.T., students, professors and staff, and outside M.I.T. Even if I do not cite them all, it does not mean that I did not think of them while writing these acknowledgements.

Lastly, I would also like to thank my funding sources, and more particularly the Belgian American Educational Foundation (BAEF) for its fellowship which allowed me to come to MIT in the first place, and IBM for its predoctoral fellowship which guaranteed my funding at the very end of my Ph.D.

1. INTRODUCTION

In recent years, techniques for depositing, growing and processing thin films for electronic and optoelectronic applications have become the subject of intensive research in the field of electronic materials. The need for control of the crystalline quality and of the compositional profile in semiconductor heterostructures has led to the development of new techniques such as Molecular Beam Epitaxy (MBE) and Chemical Beam Epitaxy (CBE).

Similarly, the use of ions in semiconductor materials growth and processing offers numerous advantages and has been investigated for several years. At intermediate energies (10 keV - 300 keV), ion implantation is used to obtain well-controlled doping profiles to high concentrations. Ion Beam Synthesis (IBS) allows the formation of buried layers: the most successful application of IBS is the formation of dielectric layers (Semiconductor IMplantation by OXygen and by NItrogen, SIMOX and SIMNI) for Silicon On Insulator (SOI) technologies and etch stop structures. The use of low energy ions also expands considerably the range of conditions for electronic materials processing and hence the possibilities for metastable heterostructure formation. Ion beam doping is one of the techniques now used in MBE to achieve high dopant incorporation with sharp profiles. Ion Beam Deposition (IBD) has been demonstrated to be a low temperature technique able to grow epitaxial and dielectric layers. The main advantage of IBD resides in the low temperature nature of the IBD process. The kinetic path is modified in such a way that athermal steps are controlling the growth kinetics. This allows the growth of epitaxial layers at lower temperature than by MBE, and chemical reaction such as oxidation at room temperature. This athermal enhancement of the growth mechanisms adds greatly to the flexibility and range of the film formation while keeping the amount of defects to a minimum due to the low energy.

OUTLINE OF THE RESEARCH

In the present research, several aspects of semiconductor thin film formation using low energy ion beams were investigated both on the theoretical and experimental levels.

Theoretically, quantitative models taking into account the physical phenomena involved in IBD were developed in order to describe epitaxial and dielectric film formation. Correlations between simulations and experimental results brought new insight into the mechanism of IBD growth.

Experimentally, the issue of thin dielectric film formation on semiconductors was explored, with special emphasis on formation of new oxides of strained heteroepitaxial $Si_{1-x}Ge_x$ layers on Si (100) and of GaAs (100). A detailed study of the dependence of phase formation upon ion energy was made possible by performing the ion beam processing in Ultra-High Vacuum (UHV) with in situ X-ray Photoelectron Spectroscopy (XPS) analysis. This experimental setup avoids any interference with background gas incorporation and possible modification after exposure to atmosphere. The unique combination of ion beam processing in an XPS chamber connected with an MBE apparatus also enabled us to study for the first time the formation of new dielectrics based on $Si_{1-x}Ge_x$. Both nitrides and oxides were formed and studied in situ by XPS. The present graduate thesis focused on Ion Beam Oxidation (IBO) while the graduate research of Olof C. Hellman [1] focused on Ion Beam Nitridation (IBN).

OUTLINE OF THE THESIS

The second chapter is an introduction to thin film growth using low energy ion beams. The IBD technique is first reviewed in terms of concept, previous work, advantages and limitations. A new technique is then presented: Combined Ion and Molecular Deposition (CIMD) [2]. The basic idea of the CIMD technique is to combine Molecular Beam Epitaxy (MBE) and Ion Beam Deposition (IBD), in order to create a thin film processing technique where an independent control of temperature and kinetics can be achieved. In CIMD, elemental or compound thin films are grown by simultaneous deposition from a low energy ion beam (10 to 500 eV) and one or several molecular beams. The interest of CIMD is that it combines the advantages of both MBE and IBD while circumventing their respective limitations. Experimental evidence of the CIMD advantages are also presented. This introductory chapter is concluded by presenting the motivation and goals of the present thesis in light of the previous work.

Chapters 3, 4 and 6 presents our quantitative models for the IBD (and CIMD) growth of semiconductor-based epitaxial and dielectric films. Chapter 3 describes qualitatively the physical phenomena involved in IBD and introduces the specific models for homodeposition by IBD and CIMD, developed in chapter 4, and for oxide layer formation in single or multi-element targets by IBO, developed in chapter 6. Correlations between previous experimental observations and the present theoretical calculations were possible in the first case while additional experimental study was necessary in the second.

Chapter 5 thus presents the experimental study of ion beam oxidation of Si, Ge, and MBE-grown $Si_{1-x}Ge_x$ layers, as well as GaAs. This experimental study provides the experimental set of observations that the computer model in chapter 6 will account for.

In chapter 7, the previous results are summarized and correlations between observations made in the different systems presented. Comparison with the parallel study of Ion Beam Nitridation (IBN) is also briefly discussed. Features common to the IBD, IBO and IBN processes are then pointed out and discussed in light of both the theoretical computer modelling and the experimental observations.

In the last chapter 8, we present the electrical characterization of the IBO Si- and SiGe-dioxide films by Capacitance-Voltage measurements. Preliminary MOS test circuits using the IBO films as the gate dielectricwere also fabricated and characterized.

2. OVERVIEW OF THIN FILM GROWTH FROM LOW ENERGY ION BEAMS

2.1. ION BEAM DEPOSITION (IBD)

a. CONCEPT

Ion Beam Deposition is a growth technique where a thin film is directly deposited from a low energy (10 - 500 eV) ion beam which is the only source of materials. IBD has been investigated for several years and significant results have been obtained. Table 2.1 summarizes the results of IBD of thin semiconductor [3-22], dielectric [23-36] and metallic [37-47] overlayers, with their most important characteristics. In general, IBD produces a thin surface film. In the specific case where the ion species is either oxygen or nitrogen, a chemical reaction occurs and the denominations of Ion Beam Oxidation (IBO) and Ion Beam Nitridation (IBN) are used, respectively.

The energy and direction of the ion beam are two key parameters for IBD. To obtain net deposition, the sputtering yield, S, fixed by the ion energy and incidence must be lower than unity, i.e. that for each ion deposited, less than 1 atom is removed from the substrate. Normal incidence of the beam favors incorporation of the ions versus sputtering of the target [48]. At normal incidence, the ion energy should be low enough to have $S < 1$. This sets an upper limit for the ion energy which is less than 1 keV for most ion-substrate combinations. If the ions have an energy higher than the threshold energy to penetrate the surface layer, IBD of materials occurs in the first

Table 2.1: IBD Experiments ($E_{ion} \leq 1$ keV)

Ion	E_{ion} (eV)	Substrate	T (°C)	Remarks	Ref.
				IBD of Si & Ge	
Si	100 - 200	Si (100)	R.T. - 740	Amorph. at R.T., poly. at 600 °C & epi. (+defects) at 740 °C	[3]
Si	50 - 100	Si (100)	R.T. - 600	Epitaxial at 400 K	[4]
Si	20 - 40	Si (100)	350 - 600	Epitaxial (1 Å/sec), Buried defects at high T°, less at low T°	[5-8]
Si	10 -200	Si (100)	R.T. - 800	Epitaxial films @ 10 - 40 eV, 350 - 550 °C,	[9]
Si	50 - 100	Ge (100)	R.T. - 600	Epitaxial at 400 K	[4]
Si	250 - 500	Sapphire	R.T.	"Well-crystallized" (by XRD)	[10]
Ge	100 - 200	Ge (100)	R.T. - 350	Epitaxial at 300 °C (by RHEED)	[11]
Ge	30	Ge (100)	200 - 400	Epitaxial at 400 °C	[8]
Ge	100 - 200	Si (100)	R.T. - 350	Epitaxial relation but defective layers (dislocation loops)	[3,11]
Ge	40 - 200	Si (100)	R.T. - 400	Amorphous, uniform and high density	[5-8]
Ge	40	GaAs (100)	400	Epitaxial	[8]
				IBD of Semiconductors (≠ Si, Ge & C)	
Ti...	100	Si (100)	500	Silicides of Ti, Ni, Co & Fe up to 3000 Å, bulk-like ρ	[8,12]
Ga/As	10 - 100	Si(100)	400	Switching back and forth between Ga & As, 1 ML/cycle	[13]
Ga/As	10 - 100	Ge (100)	400	Epitaxial & ± stoichiometric	[13]
Ga+As	40 -240	Si (100)	500	Double IBD, epitaxy at 40 eV, very slow (125 Å/hr)	[14]
				IBD of C	
C	40	Si	R.T.	First diamond-like carbon films (1970)	[15]
C	50 - 100	various	R.T.	Polycristalline films with crystalline regions	[16]
C	30 - 100	Ni, Si, KCl	R.T.	Polycristalline films with crystalline regions	[17]
C	< 1 keV	Diamond	500 - 800	Epi. diamond (900 eV, 700 °C, clean surf.), no perfect films	[18]
C	300 - 600	Si, Al	R.T.	Diamond-like carbon	[19]
C^-	10 - 100	Si (100)	R.T.	IBD with negative ions	[20]
C	120	Si (111)	R.T.	Amorphous diamond-like films	[21,22]

Table 2.1 (cont.): IBD Experiments ($E_{ion} \leq 1$ keV)

Ion	E_{ion} (eV)	Substrate	T (°C)	Remarks	Ref.
				IBD OF SEMICONDUCTOR-BASED DIELECTRICS	
O	200	Si (100)	R.T. - 400	stoichiometric & uniform SiO_2, with bulk density, sharp interface (3.5 Å), & thickness limited to 70 Å	[7,8,23]
O	200	Ge (on Si)	400	stoichiometric GeO_2 on Ge	[23]
O_2 + Ar	< 150	Si (100)	R.T. - 650	stoichiometric 50 Å SiO_2 used as a MOS gate, thickness limited, athermal growth (same thick. at 650 °C)	[24,25]
O_2	100 - 1 k	Si,Ge,$Si_{1-x}Ge_x$	R.T.	phase formation & thick. depend on E_{ion},	[26,27]
O_2	100 - 1 k	GaAs (100)	R.T.	Mixture of Ga_2O_3 + As_2O_3 depend on E_{ion}	[26,28]
N_2	30 - 3 k	Si	R.T.	Thin Si_3N_4 (19Å @ 500 eV), thick. not dependent on E_{ion}	[29]
N_2	30 - 3 k	Gr. IV sc.	R.T.	Si, Ge and Sn nitrides, thick. not dependent on E_{ion}	[30]
N_2	500 - 5 k	Si	R.T.	Nearly stoich. Si_3N_4 , thick increases with E_{ion}	[31]
N_2	100 - 1 k	Si, $Si_{1-x}Ge_x$	R.T. - 400	Si & $Si_{1-x}Ge_x$-nitrides, thick. & stoich. depend on E_{ion} & T	[1,27]
N_2	100	GaAs (100)	R.T.	formation of a 15 Å $Ga_{0.67}As_{0.33}N$ film	[32]
O_2, N_2	100 - 500	Si, Sapphire	100	SiO_2 & Si_3N_4 by IBD + Ion Cluster Beam Dep. (ICBD)	[33]
O_2, N_2	60	BK7	R.T.	Thin SiO_2 and Si_3N_4 films (e^- beam evaporation of Si)	[34]
N_2	500	Si, Sapphire	R.T.	SiN films up to 1 µm (e^- beam evaporation of Si)	[35]
O_2, N_2	500	various	R.T.	SiO_x, TiN_x by IBD + ICBD	[36]

Table 2.1 (cont.): IBD Experiments ($E_{ion} \leq 1$ keV)

Ion	E_{ion} (eV)	Substrate	T (°C)	Remarks	Ref.
				IBD OF METALS AND METAL-BASED DIELECTRICS	
Ag, Zn	30 - 300	Al, steel, Cu	R.T.	Dislocations or twins increase with E, non uniform films	[37]
Pb, Cu	50 - 60	Si	R.T.	Discontinuous at 150 Å, continuous at 600 Å	[38]
Pb, Mg	24 - 120	C, NaCl	R.T.	Discontinuous at low and high energies	[39]
Pd	50 - 100	Si (111)	R.T.	+post-anneal at 400 °C, $PdSi_2$, selective deposition observed	[40]
Fe	40	Ag (001)	200	Epitaxial films	[41]
Pb/Mg	50	Pb	R.T.	Metastable $Pb_{0.5}Mg_{0.5}$ alloy (Polycrystalline)	[42]
Cu	20 - 200	Cu (100)	150	Epitaxial films if clean and undamaged surface	[43,44]
O_2	30 - 180	Cr, Ni	R.T.	Thin oxides for tunneling junctions	[45]
O_2	60 - 200	Si	R.T.	Stoich. Ta_2O_5 by IBD + ICBD	[46]
O_2, N_2	60 - 200	Si	R.T.	WO_x, MoO_x, TaN_x by IBD + ICBD	[47]
				LOW ENERGY ION BEAM ETCHING	
Ge	500	Ge (100)	R.T.	+ annealing (600 °C, 30 min)	[8]
Cl, F	10 - 50	Si (100)	R.T. - 600	good for epitaxial growth, (R.T. + short anneal)	[8]
H		GaAs	R.T.	for heteroepitaxy of Ge	[8]
Cl	300 - 5 k	GaAs (100)	R.T.	below 500 eV, cleaning of GaAs without excessive damage	[43]
F, CF_x	0 - 2.5 k	Si (100)	R.T.	(x=1,2,3) Etching rate increases with F/C ratio	[11]

few monolayers below the surface, i.e. in the subsurface region, which we call "layer anchoring". This threshold energy, equal to the displacement energy, E_d, is of the order of 10 - 40 eV for most materials and sets a lower limit for the deposition energy.

With the models proposed by Herbots et al. [5] and later by Lifshitz et al. [49], thin film growth by IBD can be understood as a three step process (Fig. 2.1): 1) implantation of the ions in the subsurface region, 2) formation of a continuous layer of the implanted species, and 3) growth of the IBD film from the ion beam.

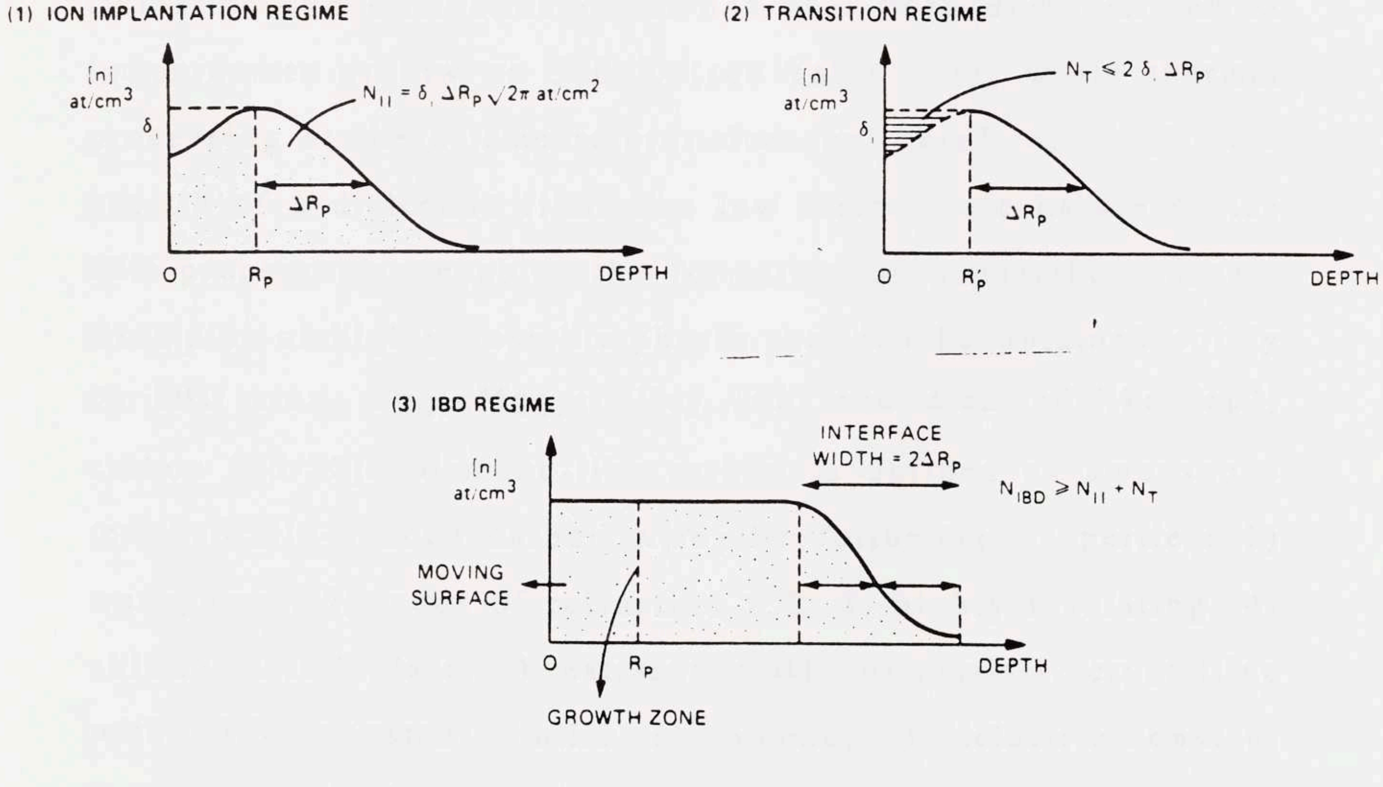
(1) ION IMPLANTATION REGIME

(2) TRANSITION REGIME

(3) IBD REGIME

Figure 2.1. Macroscopic IBD growth model [5]

b. ADVANTAGES OF IBD

The main attraction of IBD is the low temperature nature of the process. Through atomic collisions between incoming ions and target atoms, point defects are athermally generated and bonds between substrate atoms are broken. This leads to an athermal enhancement of atomic mobilities and chemical reactivities in the subsurface region, resulting in lower processing temperatures for epitaxial growth and compound formation. Examples of low temperature epitaxy and compound formation are listed in Table 2.1. Epitaxial Si on Si has been grown by IBD [3-9] with significant growth rates and thicknesses substantially larger than the limiting thickness for MBE established by Eaglesham [50] at the same temperatures. Oxidation and nitridation of Si has also been demonstrated at temperatures as low as 300 K (see Table 2.1), while thermal processing at these temperatures does not result in significant growth of a dielectric film. The low temperature nature of the IBD process also enables the formation of metastable phases. Examples of highly unstable phases that can be obtained solely by IBD are: $Pb_{0.5}Mg_{0.5}$ alloy [42] and diamond-like (sp^3) carbon [15-22]. Diamond-like carbon is defined as amorphous tetrahedrally-bonded carbon with the following properties: 1) transparent, 2) index of refraction > 2, 3) highly insulating, 4) able to scratch glass, 5) resistant to HF, 6) partially crystalline with lattice constant similar to diamond, 7) dielectric constant between 8 and 14

Moreover, accurate control over critical processing parameters such as ion energy, species, directionality, and flux provides new degrees of freedom to tailor the film properties, such as thickness and stoichiometry. The low temperature of the IBD process allows the growth of very thin insulating films with well controlled thicknesses and properties. IBD is also a technique compatible with an UHV environment: the ion beam is electrostatically confined to the deposition area and introduces no contamination in the UHV chamber.

Other advantages of IBD are layer anchoring, ion compaction and lateral uniformity. When deposition occurs by penetration of the ion underneath the surface (Fig. 2.1), the growing film is anchored in the substrate; the original substrate surface and its associated defects are buried in the overlayer and a new interface is formed with the substrate. In these conditions, the IBD films are also characterized [5-8] 1) by a density close to the bulk density due to ion compaction and 2) by a very good uniformity and sharp interface throughout the deposition area, due to the uniform nucleation of the film induced by the ion beam impingement.

c. ATHERMAL NATURE OF THE IBD PROCESS

The athermal enhancement of atomic mobilities and chemical reactivities can be described as follows. The kinetic path for epitaxial growth and/or compound formation during IBD can be modified in two ways. Thermally activated steps can be either eliminated or substituted by different athermal steps. The activation energy for the modified kinetic steps can also be provided by the ion kinetic energy lost during its incorporation.

In epitaxial growth by IBD, the athermal enhancement of the atomic mobilities results from both types of modifications in the kinetic path. The mediating species leading to epitaxial growth at low temperature are the point defects *athermally* created in the collision cascade by the ions, while surface diffusion is enhanced by collisions of the ions with the adatoms. In the particular case of semiconductors, the interstitials are believed to be highly mobile even at low temperature such as 300 K, while the vacancies are thought to be immobile below 800 K. The growth is then mediated by the fast diffusing interstitials. These can recombine with the surface, leading to thin film growth or annihilate the vacancies, resulting in a film with few residual defects. Interstitial diffusion and surface recombination are thus the rate-limiting steps in IBD. These steps with a very small activation energy make the epitaxial growth by IBD virtually an athermal process in the low temperature range (300 - 700 K).

Examples of kinetic path modifications can also be illustrated by comparing conventional oxidation to ion beam oxidation of $Si_{1-x}Ge_x$ layers and GaAs. Fig. 2.2 illustrates schematically the differences in kinetic paths between thermal oxidation and IBO. During thermal oxidation (Fig. 2.2a), the several steps leading to oxidation, namely surface absorption, dissociation, diffusion and the reaction itself, must be all

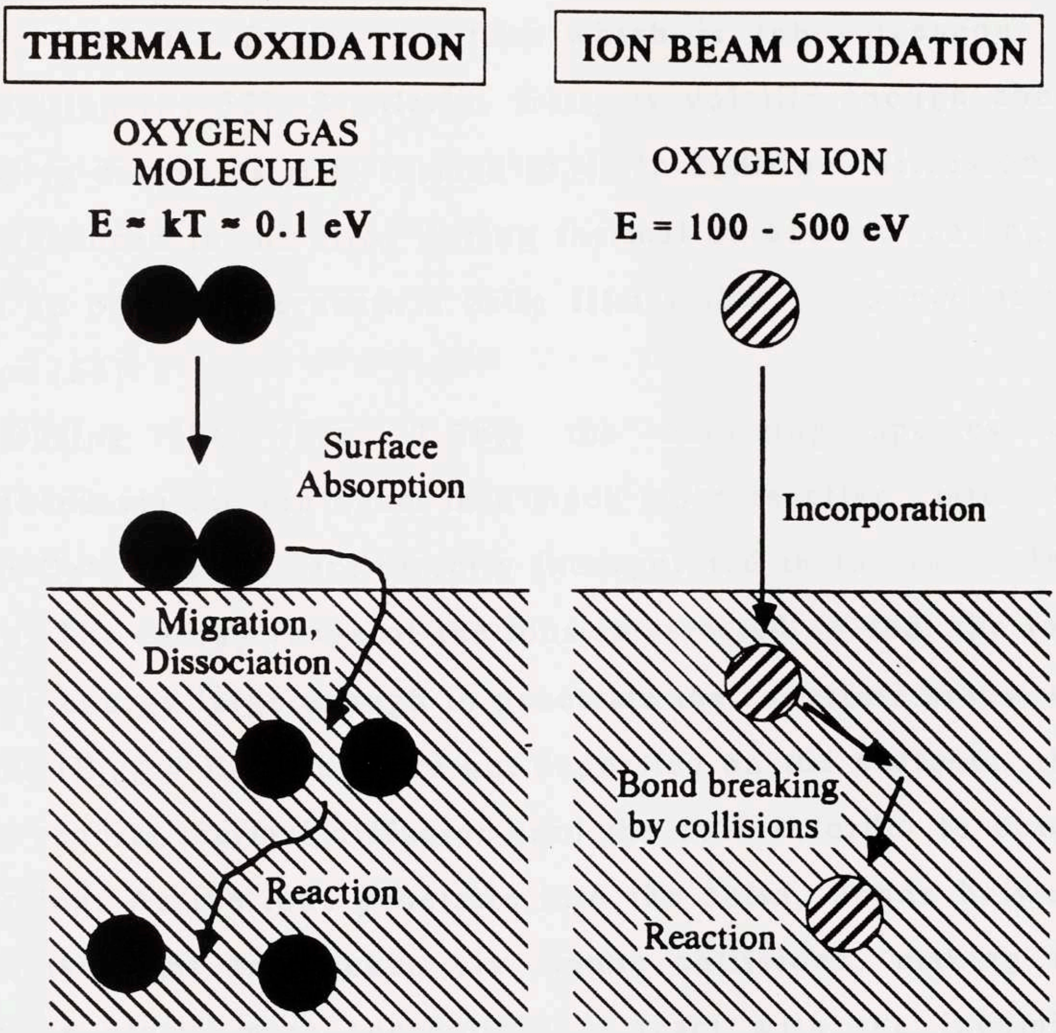

Figure 2.2. Kinetic path of conventional thermal oxidation versus Ion Beam Oxidation

thermally activated. The activation energy associated with each step must be provided thermally by heating the substrate to high enough temperatures (above 700 °C for $Si_{1-x}Ge_x$ and 500 °C for GaAs). However, at these high temperatures, other processes compete with the desired oxidation. The arsenic oxides, highly volatile at the oxidation temperature, evaporate upon formation, leaving behind a Ga_2O_3-rich film which is inhomogeneous in composition [51-52]. Similarly, GeO_2 is volatile enough above 500 °C to desorb as it is formed [53]. In addition, diffusion of Si is enhanced in the alloy during thermal oxidation, leading to a pile up of Ge underneath a SiO_2 film which is formed at the surface [54].

During IBO (Fig. 2.2b), the oxidizing species are introduced via the ion beam in a much more reactive state: O^+ and/or O_2^+. The ions are directly incorporated in the subsurface region. The energy range of the ions is selected so that the ions have an energy large enough to penetrate the substrate below the surface ($E_{ion} > E_d$). They are not deposited on the surface; this would require thermal diffusion into the bulk in order to obtain a reaction. As the ions penetrate into the solid, bonds between substrate atoms are broken via atomic collisions, making the substrate atoms more succeptible to react with the incoming oxygen species. Ion incorporation, atomic collision and bond breaking are all athermal, leading to a kinetic path for oxidation that requires little or no thermal activation.

The interest of IBO versus thermal oxidation is thus twofold: IBO either substitutes the thermal activation energy of a given step in the oxidation reaction by the kinetic energy of the ions, or it modifies the kinetic path of the reaction by directly eliminating or substituting a step by an athermal one. For instance, IBO with an atomic oxygen ion beam eliminates the dissociation step of molecular oxygen. The athermal bond breaking induced by collisions substitutes for the process by which substrate atoms bonds are broken and oxide bonds are formed at higher temperatures. Both effects lower the thermal budget during IBO to the point that room temperature processing becomes possible.

d. IBD VERSUS OTHER ION BEAM TECHNIQUES

IBD is the low energy case of Ion Beam Synthesis (IBS). Low energy IBD growth of thin surface films can be put in parallel with high energy IBS formation of epitaxial and/or compound buried layers. Results from high energy IBS can sometimes be extended to low energy IBD growth. Such similitude has been pointed out for example between the formation of buried SiO_2 layers by SIMOX and the growth of SiO_2 surface films by IBO [55].

On the other hand, IBD should be distinguished from other deposition techniques involving low energy ions, such as plasma deposition and Ion Beam Assisted Deposition (IBAD) techniques [56]. In IBAD, ions are used to modify the kinetics of a conventional thin film growth technique such as Chemical Vapor Deposition (CVD). Generally, inert gas ions such as Ar are used. They are not intended as a constituent of the deposited film, although significant incorporation of the ions can occur and affect the film properties. In plasma deposition techniques, the energy and direction of the deposited species are not well defined. Several active species such as ions, radicals and neutral species are participating in the growth process. In IBD, however, a monoenergetic, directional, and optionally mass-analyzed beam of low energy ions is the only source of materials to form the films. IBD thus offers a much better control of processing parameters such as ion energy, direction, flux, and species. It is then possible in IBD to separate the effects of each of these parameters on the kinetics of IBD growth and to take advantage of these effects to taylor the thin film properties.

e. TECHNICAL ASPECTS OF IBD

Implementation of IBD can be of very different types (Fig. 2.3). The ion beam can be generated (Fig. 2.3a) by an ion implanter (10 keV - 200 keV), mass-separated by an analyzing magnet to have an isotopically pure beam and finally decelerated close to the target to the low energy required for deposition. This is the most desirable configuration for IBD because of its capability of producing ion beams with a high flux and a high purity. It is also UHV compatible with appropriate differential pumping. Small ion sources (Fig. 2.3b) generating low energy beams (10 eV - 5 keV) such as the Collutron, Kauffman or even electron impact ion sources can be used. They suffer from contamination of the beam and lower beam current density. The

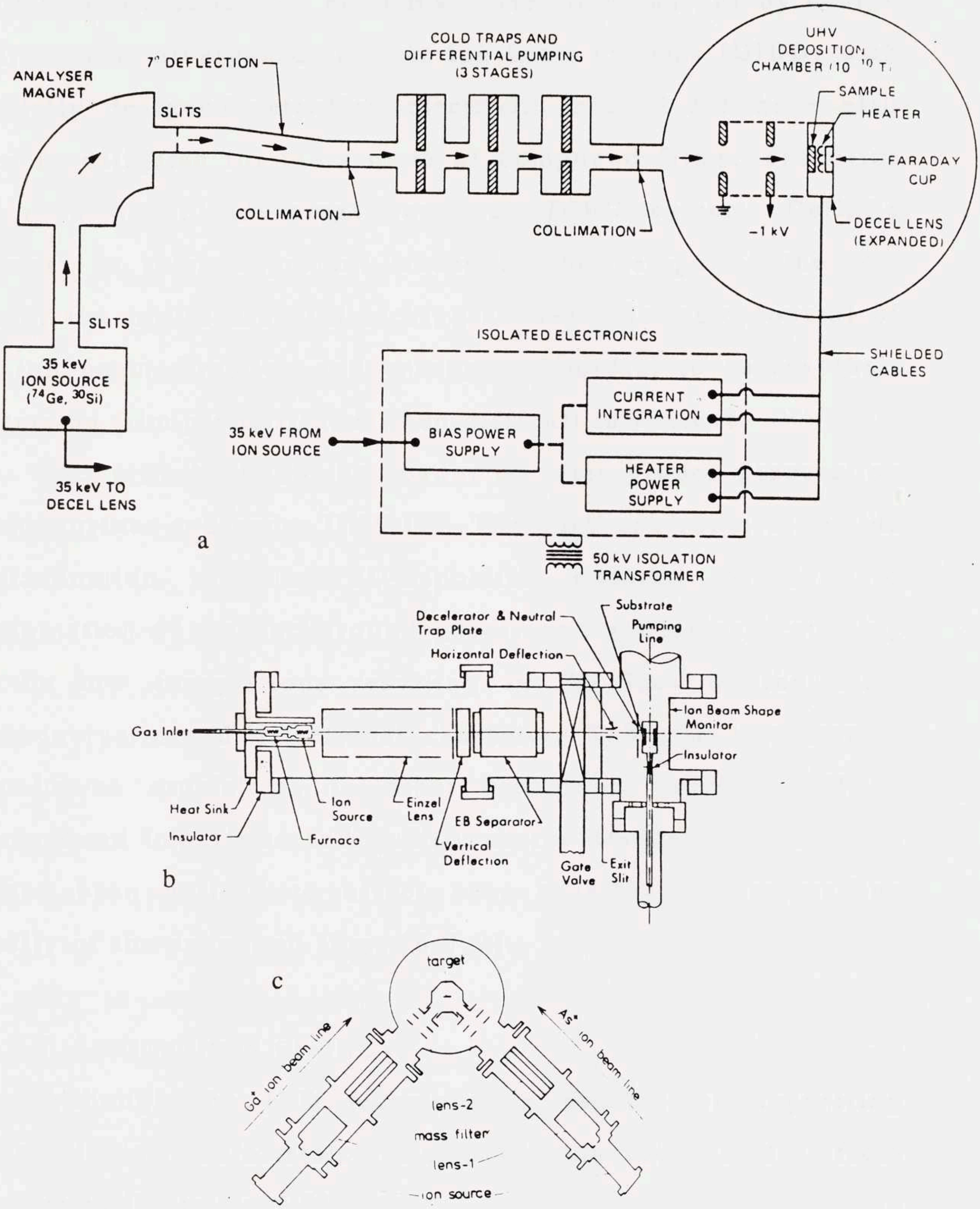

Figures 2.3. Possible implementations for IBD

a) Acceleration-deceleration scheme using an ion implanter connected to a UHV chamber [5]

b) Low energy ion source (Collutron source) [39]

c) Double Ion Beam Deposition system (DIBD) [14]

Kauffman source is also not UHV compatible and has by design a large beam divergence. Double ion beam systems (DIBD) with specially designed retarding electrode (Fig. 2.3c) have also been investigated for the growth of compound films. The price tag is a big disadvantage for such DIBD system. Definite answers to some important issues in the design of the low energy ion optics are still lacking as well. Reliable control of the ion beam direction and energy, primordial to assess their effects on film properties, is then difficult to achieve.

IBD growth should be conducted after proper preparation of the surface and under UHV [7]. The UHV environment avoids contamination of the IBD-deposited material by forward implantation of the background gases, and excessive scattering of the low energy ions resulting in the loss of the beam monoenergetic and directional character. Substrate preparation can be as crucial as in other techniques such as MBE. Background impurities and quality of the starting surface have indeed been noticed to affect very sensibly the crystalline quality of the deposited films [6,7,9].

f. LIMITATIONS OF IBD

Although the IBD technique is capable of depositing epitaxial films and/or stoichiometric compounds, it suffers from three main limitations [7].

The major disadvantage of IBD is its low growth rate due to the rather low fluence of the ion beam. The ion current density must be high enough to achieve reasonable growth rate in practical deposition time and to minimize the background contamination. Two reasons, one physical and the other technical, limit the production of low energy ion beams with a high current density. The first one is the space-charge effect of beam broadening resulting from the coulombic repulsion between the ions in the beam. This effect is more pronounced for higher current densities, lower energies and heavier ions. The second reason is the limited efficiency of ion sources in the extraction of ions at low voltages: this efficiency decreases with the extraction voltage. These two reasons explain why an acceleration-deceleration scheme is the most efficient implementation for IBD. The ions are produced at higher energies with a high current density. They are then decelerated before impinging the substrate, either by a retarding lens in front of the grounded substrate or by biasing the substrate itself which acts as the final retarding electrode. This minimizes the beam spreading due to space-charge effects and produces a significant current density at the target.

The second disadvantage of IBD is directly connected to its main advantage in epitaxial growth. The low energy ions, while impinging the substrate, create in a controllable way a non-equilibrium concentration of point defects, vacancy and interstitials, responsible for the athermally enhanced atomic mobility. However, in pure IBD, this generation of defects is too effective for the amount of materials being deposited, resulting in an excess of defects remaining in the film and/or in the structure after growth [5-7]. A critical parameter is then the ratio of the number of defects created per ion to the number of deposited species, or R_d. The ratio R_d is a measure of the athermal enhancement of the atomic mobility, but also of the amount of residual defects that will be left in the structure after growth. In IBD, this ratio is equal to the number of defects per deposited ions. It is fixed for a given ion energy and cannot be controlled independently of the ion beam flux or growth rate. With the ion energy larger than the displacement energy, R_d is large enough so that the mobility enhancement is sufficient to lead to growth and epitaxial ordering at low temperature. However, R_d is too large in the sense that too many defects are created per deposited ions and the fraction of defects not contributing to film growth is responsible for residual damage in the structure (see Chapter 4).

Finally, IBD used alone is a limited technique for the formation of compound materials. Indeed, compound films formed by reaction of the substrate with the ions (e.g. SiO_2 on Si) have been observed to be thickness limited due to a rapid saturation of the growth [7,27]. Compound overlayers such as GaAs can be deposited by IBD only by using special techniques such as switching the ion beam back and forth between the different species of the material [13,42] and taking advantage of the ion beam mixing occurring during IBD, or by using a double IBD system [14,46,47]. This latter technique has the disadvantage to double the cost of the ion production system, while the former necessitates a stable ion source with small transients and is intrinsically rate-limited by the hysteresis of the mass-separating magnet.

2.2. COMBINED ION AND MOLECULAR BEAM DEPOSITION (CIMD)

In order to circumvent the limitations of IBD, a new growth technique has been proposed, Combined Ion and Molecular beam Deposition (CIMD) [2]. CIMD is the implementation in the same UHV chamber of MBE and IBD, where materials are deposited simultaneously from a low energy ion beam and one or several molecular beams. The interest of CIMD is that it combines the advantages of both MBE and IBD while removing their respective limitations. We introduced the limitations of IBD used alone in the preceding paragraph. We will briefly recall some important aspects of MBE before discussing CIMD.

a. MOLECULAR BEAM EPITAXY (MBE): A BRIEF REVIEW

MBE [57,58] enables controlled growth of epitaxial layers with sharp interfaces from molecular beams generated by Knudsen cells or electron beam evaporators. Monolayer by monolayer growth is possible because MBE growth occurs far from equilibrium, i.e. the supersaturation of the deposited species is so high that a single atom forms a stable nucleus on the surface. However, MBE is still controlled by the kinetics of surface absorption and desorption, and epitaxial ordering. This involves the sticking coefficient, surface residence time and adatom diffusivity. Therefore, the growth temperature must be carefully chosen to be high enough to achieve sufficient surface mobility for migration to epitaxial sites, but also low enough for the sticking coefficient to be as close to unity as possible. This temperature window, though low compared to conventional thermal processes such as CVD and Liquid Phase Epitaxy (LPE), can limit the dopant incorporation because of low sticking coefficients as well as the possibilities of growth of artificially structured materials because of interdiffusion, intrinsic metastability (e.g. in quaternary compounds), and mechanical stresses generated by thermal expansion mismatch during thermal cycling (in strained layers limited by the critical thickness).

The UHV environment also limits the selection of elements or growth conditions that can be used because of vacuum integrity and cross-contamination problems. In a III-V dedicated system, materials like As and P are difficult to control because of their very high vapor pressures. The pumping system must be carefully designed in order to stand the high pressures required for stoichiometric growth. Moreover, the sticking coefficient of the group V elements is very low, requiring one to work with high V/III flux ratios, typically 2 for As/Ga but as large as 50 to 100 for P/In. It is thus difficult to control precisely the layer composition, especially when both As and P are incorporated into the compound. Finally, the material deposited on the walls of the chamber can also be of serious problem because it can cause degradation of the ion pumps and emanation of toxic gases when venting the system.

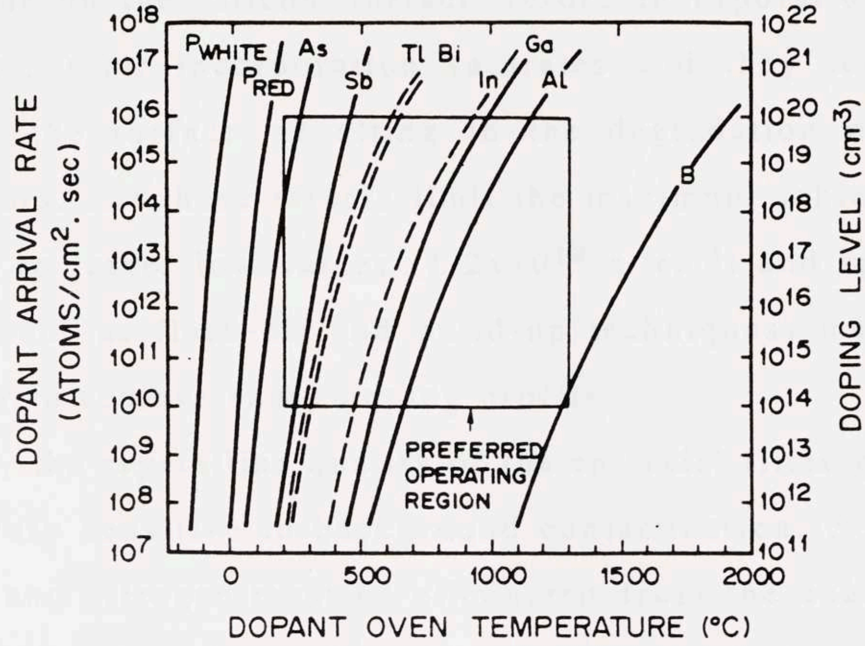

Figure 2.4. Dopants for Si MBE [59]

In an MBE dedicated to group IV semiconductors, the most common dopants (As, P and B) cannot be used as illustrated in Fig. 2.4 [59]. Indeed, the extremely high vapor pressures of arsenic and phosphorus cause cross-contamination by the dopants themselves and after growth of an As doped n-type layer, no uncompensated p-type materials can be grown. Vapor pressures of boron are too low for practical incorporation. To achieve higher doping levels, the effusion cell must be operated at such high temperatures that contamination due to outgassing of the cell itself becomes a problem. For Si MBE [60], suitable dopants are then Ga and Sb, but these dopants present other problems. Their sticking coefficients are strongly dependent on substrate temperature and very small at useful growth temperatures (typically less than 0.01). They also have a long residence time on the silicon surface before incorporation. At higher fluxes, their incorporation saturates and they tend to segregate on the surface, resulting in the degradation of the epitaxial layers. All these effects limit the maximum achievable doping level to rather low values (1-2x10^{18} at/cm^3) and special techniques (such as flash-off and build-up techniques) must be used in order to achieve sharp doping profile.

Finally, the crystalline quality of the epitaxial films grown by MBE is very sensitive to background contamination. Species like oxygen and nitrogen must be eliminated from the chamber. Therefore, dielectric oxide and nitride films cannot be formed in the MBE system, unless special techniques are used to confine the contamination to the deposition time and area.

Although MBE is a highly versatile technique capable of producing sophisticated heterostructures, it suffers from serious limitations in some material systems for doping, metastable material growth and passivation of semiconductors.

b. ADVANTAGES OF CIMD VERSUS IBD AND MBE

While CIMD maintains the athermal enhancement of atomic mobility and compound formation provided by IBD, CIMD eliminates the three main disadvantages encountered in IBD.

1. During CIMD, high growth rates can be achieved by the combination of high molecular beam fluxes with the ion beam.

2. During CIMD, a greater flexibility in the growth conditions and process optimization can be achieved, due to the control over the ratio of defects generated per deposited species, R_d . An effective control of R_d is possible during CIMD because the deposited species come from two independent sources: the ions from the ion beam and the atoms or molecules from the molecular beam(s). For a given ion energy, the ratio of ion beam flux to molecular beam flux can be chosen in order to obtain a sufficient athermal enhancement of atomic mobility for epitaxial growth at low temperature and at the same time, to control the defect generation and annihilation processes in such a way as to minimize the formation of residual damage in the structure.
3. Lastly, compounds can be easily formed by CIMD without thickness limitations, by providing one constituent through the ion beam and the other(s) via the molecular beam(s).

When compared to MBE, CIMD also offers interesting capabilities. CIMD maintains the primary advantage of IBD, i.e. the athermal enhancement of atomic mobility and compound formation. The kinetic energy of the ions replaces the thermal activation energy necessary for atomic diffusion and/or chemical reactions. Athermal processes controlling the growth mechanisms, the substrate temperature can be lowered further than in MBE. Better quality and/or new materials such as metastable alloys, thicker strained layers and metastable oxides are thus expected by CIMD growth. With ion doping by CIMD, better incorporation of dopants can also be achieved while enhancing the epitaxial growth at lower temperature. This results in a better control of the sharpness of the dopant profiles and in higher doping levels achievable without degradation of the film quality. Cross-contamination problems caused with incompatible materials for a dedicated MBE system are solved by introducing these species through the ion beam. For example, this allows the growth in vacuo of oxides, nitrides, GaAs, GaP, and InP in a *single* Si-MBE system while keeping the system uncontaminated and capable of growing high purity intrinsic silicon epilayers.

Because of the versatility of the CIMD technique, or more precisely, because almost any element can be introduced in the MBE chamber via the ion beam with no danger of cross-contamination, it is possible to conduct in the UHV environment most of the processing steps involved in the fabrication of a semiconductor device:

- *Epitaxial growth:* CIMD growth of high crystalline quality and high purity films of Si and $Si_{1-x}Ge_x$ at low temperatures
- *Dopant incorporation:* high doping levels (similar to those achieved in conventional ion implantation, i.e. $> 10^{21}$ at/cm^3) with common dopants (As, P, B) and precise control of the doping profile (δ-doping)
- *Dielectric deposition:* the possibility of growing high quality gate dielectrics and passivating layers in situ

and at low temperature is of great importance for contamination, out-diffusion and defect generation problems.

- *Metallization* and other conductive film deposition: metallic films used as gate or interconnect can be deposited by CIMD at low temperatures with good properties such as uniformity and bulk-like resistivities. In addition, the possibility of selective deposition has been demonstrated [7,40].
- *Etching:* the use of low energy reactive ions to selectively etch a layer while minimizing the radiation damage is another possibility offered in the CIMD system and has already been investigated during IBD experiments (F^+, CF^+ & Cl^+ for Si [8,11], H^+ & Cl^+ for GaAs [8,43], see Table 2.1).

To complete the in situ processing facility, methods to perform *in situ lithography* have to be implemented in the UHV system. To realize in situ lithography, a new selective laser ablation technique and an UHV compatible resist (Al, CaF2) [61] are presently under development.

The interest of in situ processing is to provide an unparalleled control of contamination by particulates and other impurities. The complete in situ fabrication of an integrated circuit can lead to new observations regarding the quality of the materials, their interfaces and other structural and electrical defects. In summary, the possibility for complete in situ processing adds to the attraction of the CIMD technique.

c. EXPERIMENTAL EVIDENCES OF THE CIMD ADVANTAGES

1. EARLY FORMS OF CIMD

The effect of a low energy ion beam on the MBE growth has been partially investigated by a few groups. Indeed, two techniques can be considered as precursors or early forms of CIMD where low energy ions are directly deposited in a film growing from a molecular beam and have a significant effect on the growth conditions such as lowering the growth temperature. These techniques are (Partially) Ionized MBE (PIMBE) [62-64] and Ion Implanted MBE (I^2MBE) [65-67], also referred to as Ion Beam Doping in MBE.

In Partially Ionized MBE, a fraction of the molecular beam is ionized by electron impact and the ions are accelerated to the substrate which is negatively biased. Shimizu and Komiya [63] studied the epitaxial growth of Si On Sapphire (SOS). They found that the epitaxial temperature, i.e. the minimal temperature at which epitaxial silicon is grown, as determined by Reflected High Energy Electron Diffraction (RHEED) could be lowered by 150 °C when the Si beam contained at least 1 % of Si ions with energies between 30 and 180 eV. They did not observe further reduction in the epitaxial temperature for ionized fractions larger than 1 % (up to 7 %). However, they did not determine quantitatively the crystalline quality of their layers to correlate it to the ion bombardment conditions.

PI-MBE has also been used to grow thin films of the wide band-gap semiconductor gallium nitride GaN [64]. Similarly, when the ionized fraction of the N beam was increased, the growth temperatures were lowered and the crystalline quality improved based on the observations of higher resistivities and lower n-type concentrations in the films.

Using I^2MBE, Ota [65] investigated the epitaxial growth of arsenic doped Si using a Collutron ion source to introduce the dopant via an ion beam. The As sticking coefficient and the epitaxial temperature determined by the carrier mobilities μ_F in the film were measured as a function of ion energy. The sticking coefficient was several orders of magnitude larger than the thermal equilibrium values. It reached unity over a wide range of temperatures and decreased with increasing ion energy and substrate temperatures. The epitaxial temperature was also decreased, especially with ion energies below 400 eV. Similarly, Sugiura [67] explored ion doping technique with Sb ions in the energy range of 130 eV to 1 keV on Si (111) at 860 °C. The Sb sticking coefficient was close to unity and doping levels above the solid solubility (up to 10^{20} at/cm^3) were obtained with an unparalleled control of the doping profile and without degradation of the electrical properties of the films.

Since these two preliminary studies, Ion Beam Doping has become one of the doping methods used in Si-MBE. A good and recent review has been compiled by J.C. Bean [68].

2. CIMD-TYPE TECHNIQUES

Moriwaki et al. [69] investigated the growth of superconducting $Ba_2YCu_3O_{7-\delta}$ thin films by CIMD at low temperature (600 °C). Their system comprises three Knudsen-cells to produce molecular beam of the metals and an Electron Cyclotron Resonance (ECR) ion source to produce the oxygen ion beam with energies of 50 eV, current densities up to 0.3 mA/cm^2 and beam diameter of 10 cm. It should be noted that the beam defocusing due the space charge effects is quite significant: 10 cm away from the ion source, the beam, originally 10 cm in diameter, has a diameter of 80 cm. Y and Cu were used as metal sources while BaF_2 was chosen instead of Ba metal to enhance the stability of the evaporation rate. As-deposited films were superconducting with a critical temperature of 80-82 K and no post-growth annealing was necessary. The ion energy serves in this case to decompose the BaF_2, to oxidize the compound and to achieve epitaxial ordering at a low growth temperature (600 °C) for this type of compound when compared to other growth techniques (typically higher than 900 °C). Similar systems are now under development where the oxygen is provided by an ion beam. [70]

Two groups [71-74] have investigated CIMD of III-V compounds using a MBE growth chamber coupled with a UHV low energy, mass-analyzed ion implantation system. Shimizu et al. [71,72] studied the homoepitaxial growth of GaAs and InP using an As^+ and P^+ ion beam as the group V source, while the group III element, Ga and In, was provided by a "conventional" molecular beam. Homoepitaxial films of stoichiometric GaAs were obtained between 220 °C and 550 °C, with a V/III flux ratio of unity and As^+ energies of 100 and 200 eV. Crystallinity was assessed by RHEED and stoichiometry by Auger Electron Spectroscopy (AES). Although RHEED patterns indicated that single-crystal films were obtained at 220 °C, photoluminescence (PL) spectra at low temperature (4.2 K) showed characteristic features such as bound exciton luminescence and emission due to the recombination of donor-acceptor pairs, only above 400 °C. High quality epitaxy was demonstrated by PL for growth temperatures of 500 °C and 550 °C, to be compared to 600 - 640 °C in MBE. The growth rate was 2×10^{13} molecules/cm^2 sec or 325 Å/hr, compared to typically 1 µm/hr in MBE. The relatively low growth rate is due to the fact that, although the ion beam current was 0.25 mA, the deposition area was quite large, 10 cm in diameter, resulting in a rather small current density at the target and hence a low growth rate. The large deposition area is due to the deceleration optics consisting of 2 electrostatic lenses in front of the substrate. This optics, even when optimized, is probably not as efficient as the technique which uses the substrate as the last retarding electrode.

Similar results were obtained with InP. The substrate temperature was varied from 210 °C to 420 °C; the ion energies were 100 and 200 eV, and the deposition rate was 1.5×10^{13} molecules/cm^2/sec. The best InP films, as determined by RHEED and PL, were obtained at 390 °C with P^+ ions of 100 eV and

V/III ratio equal to unity (compared to typically 430 °C and V/III of 50 in MBE).

Maruno et al. [73,74] investigated the growth of homoepitaxial InP for a wider range of substrate temperatures (from 200 °C to 500 °C), V/III ratio (from 1.2 to 2.2), and ion energies (from 50 to 300 eV). The optimum energy was determined to be 100 eV. At low energy (50 eV), the electrical and optical properties became poor. At higher P^+ energies (200 & 300 eV), the growth rate decreased rapidly because of sputtering, and at 600 eV, no deposition occurred. Hall measurements and low temperature (4 K) PL indicated that the best electrical and optical properties were obtained with the lower V/III ratio and higher growth temperature up to 450 °C.

These examples show that CIMD (or CIMD-type techniques) can be used to grow epitaxial layers of good crystalline, electrical and optical quality in conditions and with a versatility that are not achievable when MBE or IBD are used alone.

2.3. SCOPE OF THE THESIS RESEARCH

The present doctoral research focuses on several aspects of semiconductor-based epitaxial and dielectric film growth from low energy ion beams. Its motivation is both theoretical and experimental.

On the theoretical level, the kinetics involved in epitaxial growth by IBD was investigated in order to account for previous experimental observations of epitaxial growth by IBD of Si on Si made by Herbots et al. [5-7].

Experimentally, the formation of thin oxide layers by IBO and the dependence of phase formation and film properties upon ion energy were investigated, with particular emphasis on the formation of new oxide phases based on $Si_{1-x}Ge_x$ strained layers and GaAs for potential application in MOS technologies. Computer models were then developed to explore the kinetics of IBO by correlating the theoretical calculations to the experimental results.

a. MOTIVATION FOR THE STUDY OF IBO SIGE-OXIDES

SiGe-oxides are metastable oxides which are difficult to form by conventional thermal oxidation in both wet and dry ambients. It has been previously demonstrated [54,75] that thermal oxidation of $Si_{1-x}Ge_x$ does not result in a SiGe-oxide film, but leads to the decomposition of the $Si_{1-x}Ge_x$ alloy into a SiO_2 film with a segregated Ge layer underneath, thereby destroying the $Si_{1-x}Ge_x$ film (Fig. 2.5). Recently however, it was reported [76] that steam oxidation in a narrow range of low temperature (700 °C) resulted in an oxide layer with no Ge pile-up at the interface. In the present research, the formation of SiGe-oxides at room temperature by IBO was investigated as a function of ion energy. A systematic study of IBO of pure Si and Ge was also conducted to gain insights in the kinetics of IBO of $Si_{1-x}Ge_x$ alloys.

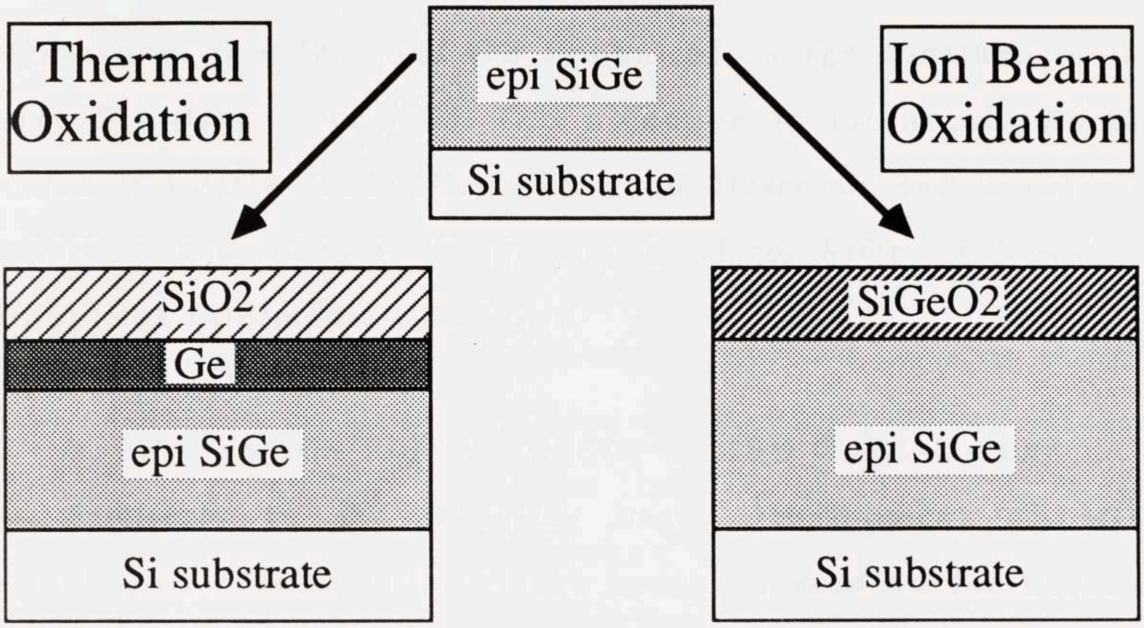

Figure 2.5. Thermal versus Ion Beam Oxidation of $Si_{1-x}Ge_x$

The motivation for our study of IBO of $Si_{1-x}Ge_x$ is the development of a CMOS technology using heteroepitaxial strained layers of $Si_{1-x}Ge_x$ as the channel materials. Indeed in Ge, the hole mobility (1900 cm^2/V sec) is only half of the electron mobility (3900 cm^2/V sec) and is much higher than the hole mobility in Si, GaAs and InP (500 cm^2/V sec). Two other properties [77] make these strained overlayers even more interesting for CMOS applications: 1) the type I band offset between unstrained Si and strained $Si_{1-x}Ge_x$ ($x < 0.85$) which renders possible modulation-doping techniques for the holes and 2) the hole mobility enhancement due to the strain . However, the crucial point is to find a high quality gate dielectric with a sharp interface and low interface state density. Presently, an intermediate Si layer is introduced between the $Si_{1-x}Ge_x$ active layer and a pure SiO_2 layer is used as the gate dielectric. A compromise needs to be made between the quality of the gate/channel interface and the amount of charge confined in the active $Si_{1-x}Ge_x$ layer [78]. Our objective is to investigate the growth of a SiGe-oxide film with good dielectric and interfacial properties to be used as the gate material for SiGe-MOS devices without the intermediate Si layer.

b. MOTIVATION FOR THE STUDY OF IBO GAAS-OXIDES

Similarly to the $Si_{1-x}Ge_x$ case, development of MOS technologies based on GaAs have been hindered so far because of the difficulty to grow or deposit on GaAs a dielectric film of sufficient quality to be used as the gate material. As potential candidates for gate material, GaAs oxides have been extensively studied for more than ten years [51,52]. As shown in the ternary phase diagram of Ga-As-O (Fig. 2.6) [79], several oxides of Ga and As exist at thermodynamic equilibrium.

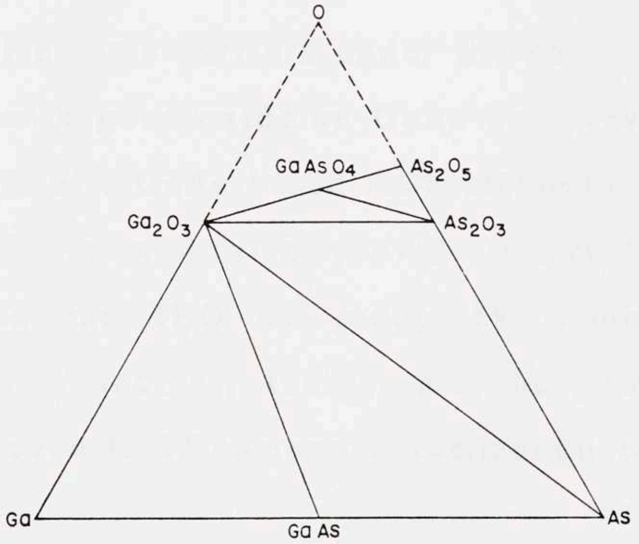

Figure 2.6. Ga-As-O ternary phase diagram below the melting point of As_2O_3 (278 °C) [79]

Ga_2O_3 and As_2O_3 are both thermodynamically stable oxides, but As_2O_3 is much more volatile than Ga_2O_3 or even As. $GaAsO_4$ and As_2O_5 are oxides richer in oxygen; they are more difficult to form because they are even more volatile than As_2O_3 and they tend to decompose into the lower oxides upon heating. As it can be seen from the phase diagram, no As oxide is thermodynamically stable in the presence of GaAs. This explains why it is difficult to form a good dielectric on GaAs. Different oxidation techniques have been studied in the past, mainly thermal oxidation, plasma oxidation and anodic oxidation. All these techniques involve a processing step at high temperature, i.e. above 300 °C, which causes the thermal decomposition of As_2O_3, according to the reaction: $2\ As_2O_3 \rightarrow 4\ As + 3\ O_2$. This results in the depletion of As in the oxide film and in the build-up of metallic As at the interface. The final oxide then shows poor insulating and structural properties at the interface and in the bulk; the Fermi level is pinned at the interface and the inversion of electronic carriers under the gate is inhibited. The inability to grow a good oxide on GaAs has prevented until now the development of a GaAs-based MOS technology.

IBO of GaAs will also provide interesting comparison points between the IBO of group IV semiconductors and compound semiconductors. Insight may be gained for IBO of other III-V or even II-VI compound semiconductors.

3. THEORETICAL AND COMPUTER MODELLING OF THE IBD AND CIMD GROWTH

In this chapter, a physical description of the phenomena involved in IBD and CIMD is first presented. The Monte-Carlo code developed to calculate the ion-solid interactions is then described in more details. A brief presentation of the specific models for IBD and IBO elaborated in this work is finally given.

3.1. PHYSICAL PHENOMENA INVOLVED IN IBD AND CIMD

To describe thin film growth by IBD, the physical phenomena occurring during ion bombardment can be categorized according to their time scale. Three separate mechanisms can be identified. Important features in the case of low energy ions will be pointed out.

a. ION-SOLID INTERACTION: COLLISION CASCADE AND SPUTTERING

The first process in IBD is the ion-solid interaction which takes place on a time scale shorter than a lattice vibration or < 10^{-13} sec. Besides the ion incorporation, it involves two main effects: athermal generation of point defects and sputtering. When the ion penetrates into the substrate, it makes several collisions with the substrate atoms before coming to rest. If the transferred energy (ΔE_n) to a target atom by collision is larger than a threshold energy or displacement energy ($\Delta E_n > E_d$, E_d = 15 eV for Si and 13 eV for Ge [80]), a vacancy-interstitial pair is created. The target atom knocked out of its lattice site becomes a recoil with an energy $E_{rec} = \Delta E_n - BE$, where BE represents the binding energy between two atoms ($BE \cong 2$ eV for semiconductors). Before coming to rest, this recoil can make collisions with target atoms and create secondary recoils which in turn create ternary recoils, and so on. These successive collisions develop in what is known as the collision cascade caused by an energetic ion. Some of the recoils created close to the surface can escape the solid if they have a kinetic energy large enough to overcome the surface potential or surface binding energy (SBE). This results in the removal of an atom from the solid or sputtering. A good approximation for SBE is to take the sublimation energy U_0 reduced by the binding energy, or $BE + SBE = U_0$ ($U_0 = 4.72$ eV for Si and 3.88 eV for Ge [80]).

Three important phenomena thus take place during the ion-solid interaction: the incorporation of the ions, the development of the collision cascade or athermal generation of point defects, and the sputtering of the substrate. As the ion energy decreases, the sputtering yield decreases. Below a threshold ion energy, it will be less than one, corresponding to actual deposition of material instead of removal. Similarly, less point defects are created by ions with lower energies, resulting in a less perturbed lattice environment in the collision cascade region. The range and range straggling of the ions decrease with energy as well, making the ion incorporation and defect generation closer to the surface at lower energies.

b. ELASTIC RECOMBINATION: REPLACEMENTS AND RELOCATIONS

The next important process is the elastic recombination of instantaneously created defects. This occurs in the time scale of a lattice vibration or 10^{-12} sec [81]. The energy transferred to a target atom in a collision must be greater than the displacement energy in order to create a stable vacancy-interstitial pair. If not, the instantaneous defect is annihilated within the next lattice vibration. This is due to elastic forces originating from the surrounding atoms, which tend to keep the struck atom in its lattice site. These forces also act on the striking species, ion or recoil from an earlier collision. If after a collision, the striking species has a kinetic energy too small to escape the collision site, i.e. $E_{out} < E_d$, it is captured by the vacant site it just created. If the striking species is an incoming ion, a *replacement* of a target atom by the ion occurs and the ion occupies a substitutional site. If the striking species is a recoil, a *relocation* of a target atom to another lattice site occurs. The replacement/relocation events are thus the results of the attractive part of the interactomic potential. The elastic forces responsible for these events come in action if the lattice environment of the defect is relatively unperturbed. This elastic recombination process is thus favored at lower ion energies because of the smaller defect density.

These two processes of replacement/relocation are schematically illustrated in Fig. 3.1 where the development of the interaction of a low energy ion with a crystal is shown.

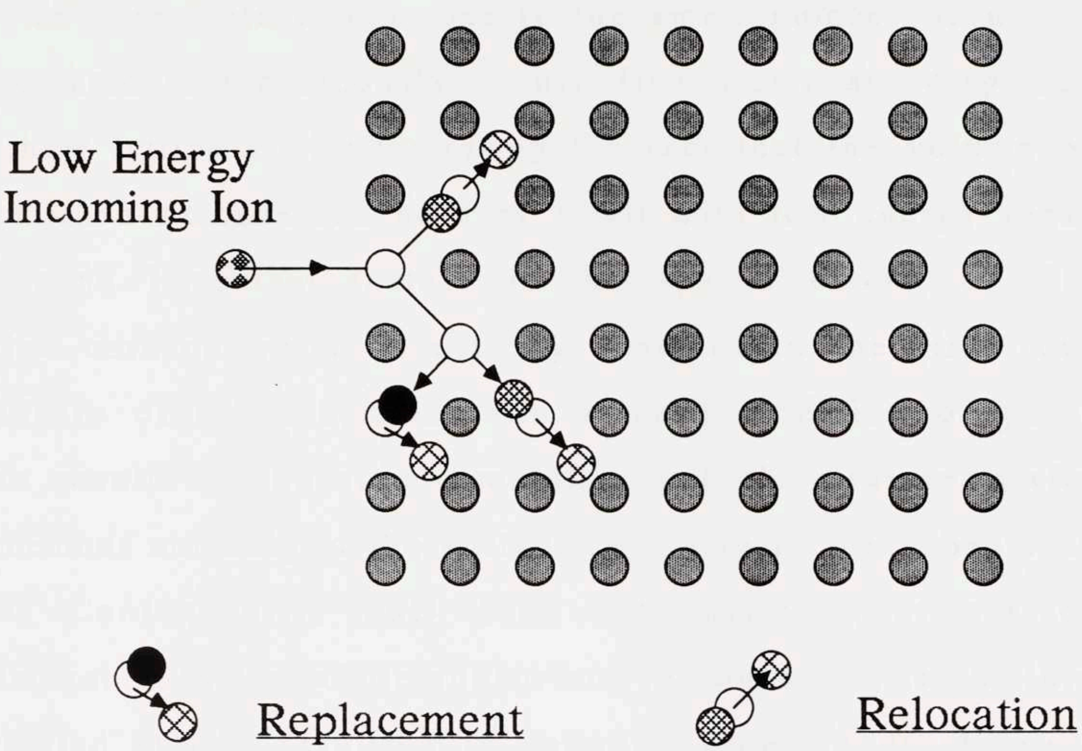

Figure 3.1. Ion-Solid interaction at low energy: collision cascade and replacement/relocation events

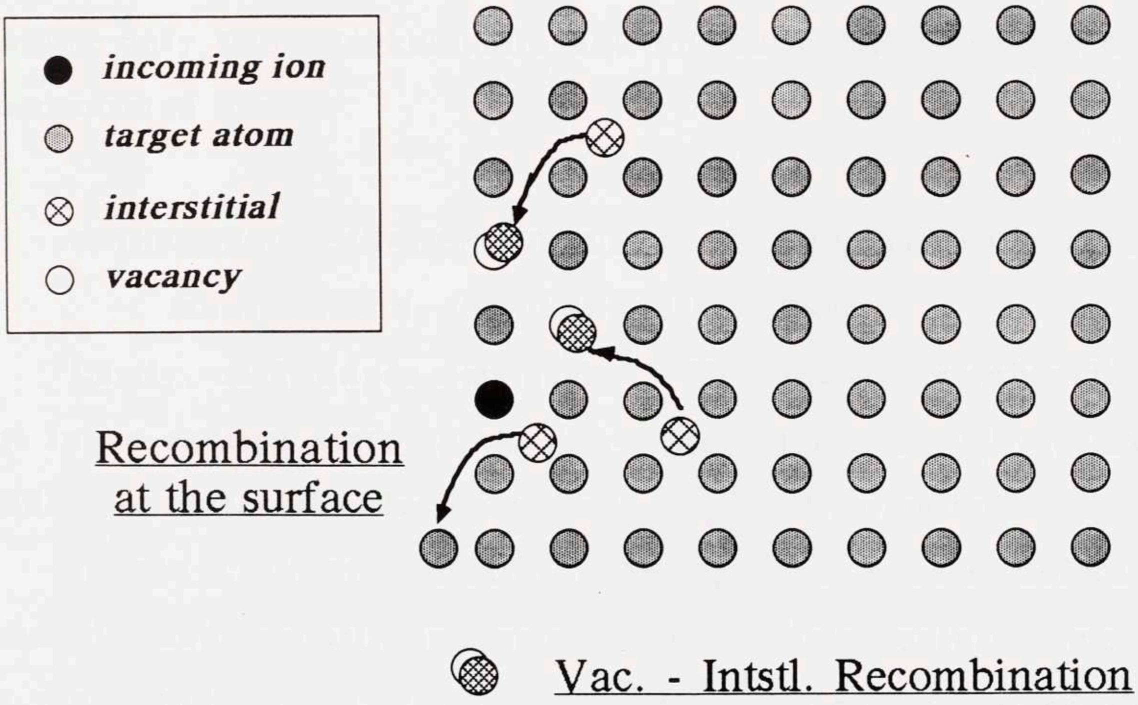

Figure 3.2. Thermal relaxation after ion-solid interaction: vacancy-interstitial annihilation and surface recombination

The first feature to notice is the small number of defect pairs created instantaneously: only five atoms are displaced from their lattice site, illustrating the fact that the volume of the collision cascade can be very small with low energy ions. The second important feature is the spatial extend of this collision cascade which is entirely confined in the first four monolayers of the substrate. The athermal creation of point defects results in the atomic mobility and chemical reactivity enhancement not only at the surface, but also in the subsurface region. Consequently, IBD does not involve just surface phenomena: it is the whole subsurface region which is put into an “excited state”, resulting in epitaxial ordering or chemical reaction at low temperature. Lastly, the already low number of generated defects is further reduced by elastic recombination, leaving only two Frenkel pairs and one interstitial for the one incorporated ion.

c. THERMAL RELAXATION: DIFFUSION, RECOMBINATION OF EXCESS POINT DEFECTS, AND CHEMICAL REACTION

Lastly, on a longer time scale (> 10^{-9} sec.), the subsurface put in an excited state by the ion-solid interaction will relax, leading to epitaxial ordering and/or compound formation.

In the case of epitaxial ordering, the excess defects, vacancies and interstitials created in the collision cascade, move by thermal diffusion. Due to the lattice distortion around the individual defects, an attractive force between vacancies and interstitials leads to their recombination. This diffusion-limited recombination restores a target atom to its lattice site. Similarly, when a defect is nearby the surface, it can diffuse and recombine at that efficient defect sink. With low energy ions, the surface recombination plays a key role since the defects are created in a shallow region and are therefore very likely to recombine with the nearby surface

These two types of thermal recombinations are illustrated in Fig. 3.2 where the two vacancies are annihilated through recombination with a diffusing interstitial, while the third interstitial readily recombines with the nearby surface. In this schematic scenario, the resulting film is left with no defect and has grown by one atom for one deposited ion.

In the case of compound formation, both the thermal diffusion and chemical reaction play an important role. The incorporated ions react with the substrate atom made available by atomic collision. Some radiation enhanced diffusion can take place as well since point defects are created.

3.2. ATOMISTIC CALCULATIONS OF ION-SOLID INTERACTIONS: TRIMCSR

To calculate the ion-solid interaction, namely ion incorporation, sputtering yield, point defect generation and replacement/relocation events, we have developed an advanced version of the Monte-Carlo code TRansport of Ion in Matter (TRIM) developed over the last decade by Biersack, Eckstein and coworkers [82-84]. Our version has the special feature to include all the ion-solid interactions mentioned above, i.e. TRansport of Ion in Matter including Collision cascade, Sputtering and Replacement/Relocation events or TRIMCSR.

a. MAIN FEATURES OF THE ORIGINAL TRIM PROGRAM

The original TRIM program calculates the ion-solid interaction in three dimensions for a multi-element, multi-layer amorphous target. The ion trajectory is calculated by TRIM using the binary collision approximation (BCA). The BCA assumes that the ion is interacting with only one atom at a time. BCA is a valid approximation, especially at high energies, but breaks down at very low energies (< 50 eV). As shown by Molecular Dynamics (MD) calculations [85-87], the detailed description of ion trajectories becomes increasingly difficult below 100 eV, as multiple collisions rather than binary collisions dominate the ion-solid interaction. Computational efforts are presently under way to address this problem [88]. However, point defect generation can still be approximated by a code such as TRIM, based on energy conservation considerations. The assumption of an amorphous target does not take into account possible channeling effects. But, in a first approximation, TRIM calculations have been extremely successful in predicting ion range and sputtering, even at low energy [89].

The trajectory of the ions is calculated using the Ziegler-Biersack-Littmark (ZBL) electronic stopping power for continuous deceleration of the ion and the Ziegler universal potential for the elastic scattering by substrate nuclei [84]. The validity of the universal potential in low energy ion-solid scattering events has been shown experimentally by the work of Tenner [89].

Lastly, the original version of TRIM is actually two programs in one, with a flag to choose between a sputtering version and a cascade version. The sputtering version provides accurate calculations of the sputtering by the ions but not of the defect generation, while the cascade version gives valid results for the point defect generation but not for the sputtering. This is due to the following computational trick: the sputtering version puts the displacement energy E_d equal to SBE. In general, SBE is significantly smaller than E_d. This results in a an overestimated number of defects created and calculations of point defect generation should be disregarded in the sputtering version. In the cascade version, on the other hand, the displacement energy has the correct value, but SBE is now set to E_d. The surface potential is overestimated in that manner and the sputtering results are not valid because they are underestimated.

b. MODIFICATIONS INTRODUCED IN TRIMCSR

We developed our own version of the TRIM program in order to be able to simulate at the same time all the ion-solid interactions. This is particularly important in the simulation of thin film growth by IBD, since all the ion-solid interactions are occurring in the shallow subsurface region: the defects are

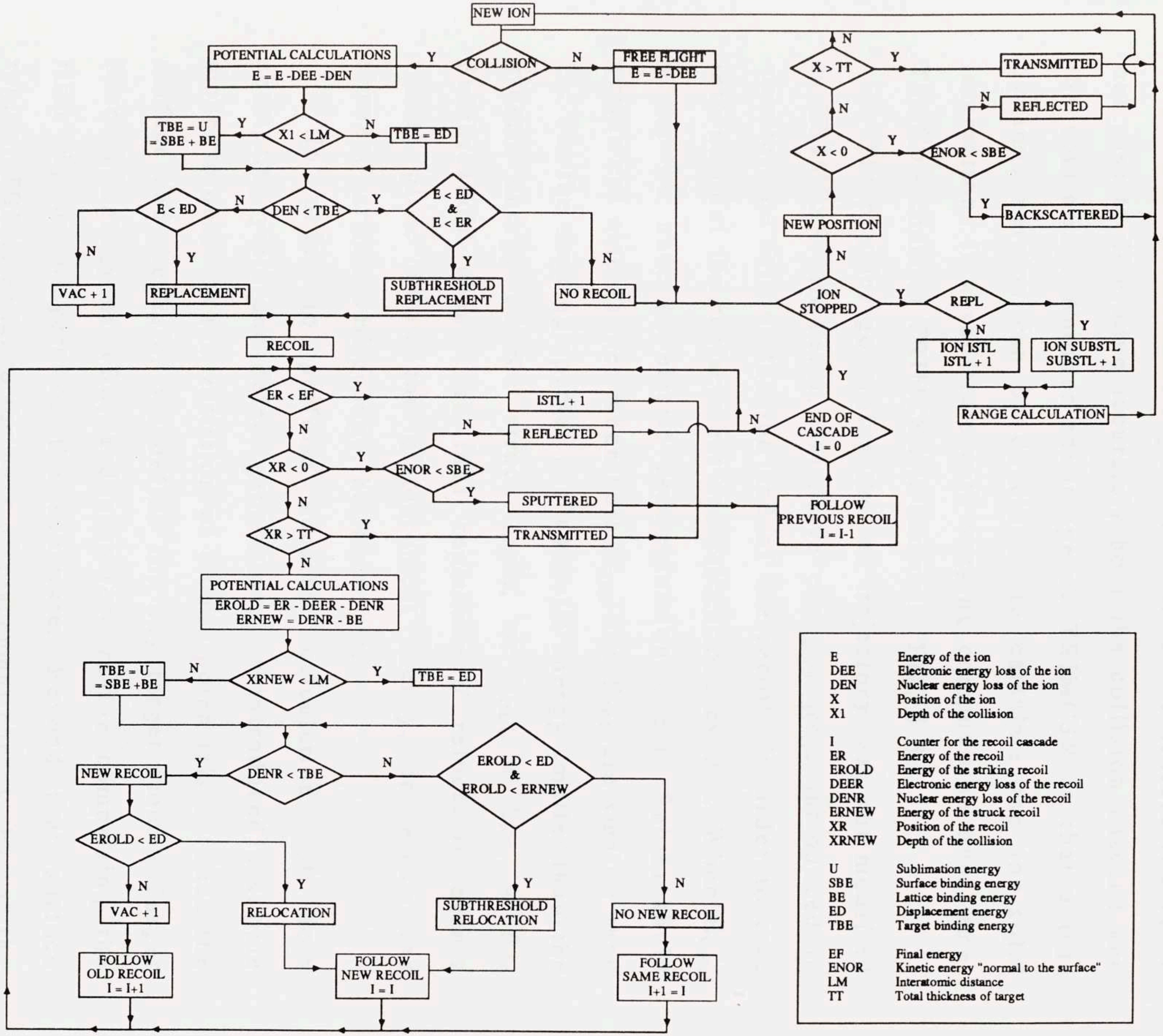

E	Energy of the ion
DEE	Electronic energy loss of the ion
DEN	Nuclear energy loss of the ion
X	Position of the ion
X1	Depth of the collision
I	Counter for the recoil cascade
ER	Energy of the recoil
EROLD	Energy of the striking recoil
DEER	Electronic energy loss of the recoil
DENR	Nuclear energy loss of the recoil
ERNEW	Energy of the struck recoil
XR	Position of the recoil
XRNEW	Depth of the collision
U	Sublimation energy
SBE	Surface binding energy
BE	Lattice binding energy
ED	Displacement energy
TBE	Target binding energy
EF	Final energy
ENOR	Kinetic energy "normal to the surface"
LM	Interatomic distance
TT	Total thickness of target

Figure 3.3. Flow chart of TRIMCSR

created in the first few monolayers while the sputtered atoms originate from the same region as well. It is therefore crucial in our case to determine accurately both the collision cascade and the sputtering. Another advantage of TRIMCSR is that a true dynamic version can be developed to calculate the ion-solid interactions in a substrate with varying composition over time. The flow chart of TRIMCSR is shown in Fig. 3.3.

The physics governing the ion trajectory was not modified in TRIMCSR. However, extensive changes were introduced to monitor the fate of the ion and of the recoils in order to take into account the replacement and relocations events. When $E_{out} < E_d$, we have an elastic recombination event. Subthreshold events can also happen when both E_{out} and E_{rec} are smaller than E_d, but the striking species has a kinetic energy smaller than the kinetic energy of the struck atom, or $E_{out} < E_{rec} < E_d$. Subthreshold events are thus replacement/ relocation events taking place below the displacement energy, in which the slowest particle will occupy the lattice site.

In order to perform accurate calculations of both sputtering yield and defect generation, we introduced a simple model to describe the variation of atomic potentials between the surface and the bulk. We define for any target atom a Target Binding Energy or TBE, and a *surface region* comprising the first N_S monolayers of the substrate. Beyond that surface region, TBE is equal to the bulk displacement energy, E_d, of the target atom. Within the surface region, TBE increases linearly from the sublimation energy, U_0 = SBE + BE, at the surface to the displacement energy in the bulk. For a collision happening in the $N_C{}^{th}$ monolayer, TBE is then given by:

$$\mathrm{TBE} = \left(1 - \frac{N_C - 1}{N_S}\right)(\mathrm{SBE} + \mathrm{BE}) + \left(\frac{N_C - 1}{N_S}\right) E_d \quad \text{for } N_C \leq N_S$$

$$\mathrm{TBE} = E_d \qquad \text{for } N_C > N_S$$

This model for the binding energy of a target atom close to the surface follows our physical understanding of atomic forces interrupted by the surface. Since these atomic forces range significantly over the second and third nearest neighbors, the surface affects or disturbs a few monolayers underneath. This is substantiated by the observation of surface reconstruction and relaxation. It is therefore physically correct to assume that the atoms in the surface region will be more and more bonded as they are deeper in the bulk, until the bulk displacement energy is reached. This simple model is targeted to represent that specific variation of bonding strength only. A similar approach was also used in another Monte-Carlo program very similar to TRIM, developed by Chou and Ghoniem, TRansport of Ion in POlyatomic Solids or TRIPOS [90].

The single parameter to fit is N_S. By performing calculation for different values of N_S ranging from 1 to 10, and comparing our results with the conventional TRIM calculations and experimental data on sputtering [91,92], we found that, for Si, defining the surface region as the first three monolayers gives us an accurate determination of both the sputtering yield and the defect production.

3.3. GENERAL PRESENTATION OF THE COMPUTER MODELS FOR IBD

The main contribution of this thesis work in the modelling of the IBD process is the detailed study of the third stage of IBD involving thermal diffusion and chemical reaction. With TRIMCSR at our disposition to calculate reliably all the ion-solid interactions, specific computer models are developed to simulate thin film growth by IBD in two cases of interest:

a. Homodeposition and epitaxial growth by IBD and CIMD with IBD of Si on Si as the model system. In this case, we will look at the role of thermal diffusion and recombination of point defects in the IBD growth kinetics. The simulation results can be compared to the experimental work of Herbots et al. [5-7]. This is the subject of chapter 4

b. Ion beam oxidation of single and multi-element semiconductor targets. In this case, we will successively examine the importance of each of the physical phenomena involved in the IBO process, namely 1) implantation/ sputtering only (model IS), 2) replacement/relocation events or ion beam mixing (model ISR) and 3) oxygen diffusion and chemical reaction (model ISRD). Our experimental study of IBO presented in chapter 5 provides the experimental base for comparison with the simulations presented in chapter 6.

4. QUANTITATIVE MODEL FOR HOMOEPITAXIAL GROWTH BY IBD AND CIMD

The purpose of the study described in this chapter is to investigate theoretically the role of atomic collisions, thermal diffusion and recombination in thin film growth by IBD in the specific case of homoepitaxy. During ion bombardment, vacancy and interstitial pairs are athermally generated through atomic collisions in the first few monolayers below the surface. In semiconductor materials, the interstitials are readily mobile even at low temperature and will diffuse in majority towards the nearby surface where they recombine, leading to net thin film growth. Vacancies can be considered immobile below 500 °C but are progressively annihilated by the interstitials diffusing to the surface.

To support quantitatively this model, a computer code was developed to simulate the thermally activated **D**iffusion and **R**ecombination of **I**nterstitials & **V**acancies during **I**BD and **C**IMD (DRIVIC). DRIVIC is based on the diffusion equations for the excess vacancies and interstitials generated by the ions and on a moving surface equation describing the IBD / CIMD growth rate. The defect generation is calculated by our advanced version TRIMCSR of the Monte-Carlo code TRIM (§ 3.2).

Using TRIMCSR and DRIVIC, IBD growth of Si on Si was calculated as a function of the ion energy. Our results demonstrate how the IBD growth is mediated by the fast diffusing interstitials. The low energy range where IBD epitaxial growth can be achieved is found to be more stringently limited by the necessity to confine the generation of defects in the subsurface region, favoring both their surface recombination and mutual annihilation, rather than by the minimization of sputtering and damage creation. Simulations and experimental results are correlated by comparing computed defect depth distributions with the microstructure of IBD grown samples. The effect of assuming different values for the point defect diffusivities upon the IBD growth mechanism is also investigated. We show that combination of IBD experiments and simulations with the present model offers the interesting possibility to determine better values of point defect diffusivities for temperatures between 300 K and 1000 K. Lastly, a relatively simple Monte-Carlo program, MCIBD, was conceived to provide a visualization of the IBD atomistics. The picture of the IBD process given by MCIBD correlates well with the DRIVIC conclusions on the energy dependence of epitaxial growth by IBD.

4.1. CONTINUUM DYNAMIC MODEL FOR THE DIFFUSION AND RECOMBINATION OF INTERSTITIALS & VACANCIES IN IBD AND CIMD: DRIVIC

The simulation code DRIVIC was developed to simulate the point defect thermal diffusion and recombination during ion bombardment. The present version can be used to calculate homodeposition by IBD. DRIVIC is based on the following continuity equations:

- Vacancy diffusion equation:

$$\frac{\partial C_V}{\partial t} = D_V \frac{\partial^2 C_V}{\partial z^2} + G_V(z-z_s)\,\phi_{ion} - k_{V\text{-}I} C_V C_I \tag{1}$$

- Interstitial diffusion equation:

$$\frac{\partial C_I}{\partial t} = D_I \frac{\partial^2 C_I}{\partial z^2} + G_I(z-z_s)\,\phi_{ion} - k_{V\text{-}I} C_V C_I \tag{2}$$

- Growth rate equation:

$$\frac{1}{\Omega}\frac{dz_s}{dt} = G_m + J_I(z_s) - J_V(z_s) \tag{3}$$

C_V, C_I are the excess concentration of vacancies and interstitials created by the ions. z (> 0) is the depth in the substrate and t, the time of IBD. The point defect generation (G_V, G_I terms), diffusion (D_V, D_I), and recombination ($k_{V\text{-}I}$) take place in the substrate (Fig. 4.1) and are described by the diffusion equations (1) and (2). The defect generation terms are obtained from TRIMCSR simulations and depend on the ion flux ϕ_{ion}. The recombination of defects is modeled as a diffusion-limited bimolecular reaction: $V + I \rightarrow 0$,with a rate constant $k_{V\text{-}I}$ given by [93]:

$$k_{V\text{-}I} = \frac{4\pi r_{V\text{-}I}}{\Omega}\left(D_V + D_I\right) \tag{4}$$

where Ω is the atomic volume and $r_{V\text{-}I}$, the capture radius (equal in first approximation to the lattice constant a_0 [94-96]).

The growth rate (eq. 3) depends on the molecular beam flux (G_m) for the more general case of CIMD and the diffusive fluxes (J_I, J_V) of point defects recombining at the growing film surface (z_s: $z_s < 0$ if the film is growing, $z_s > 0$ if the substrate

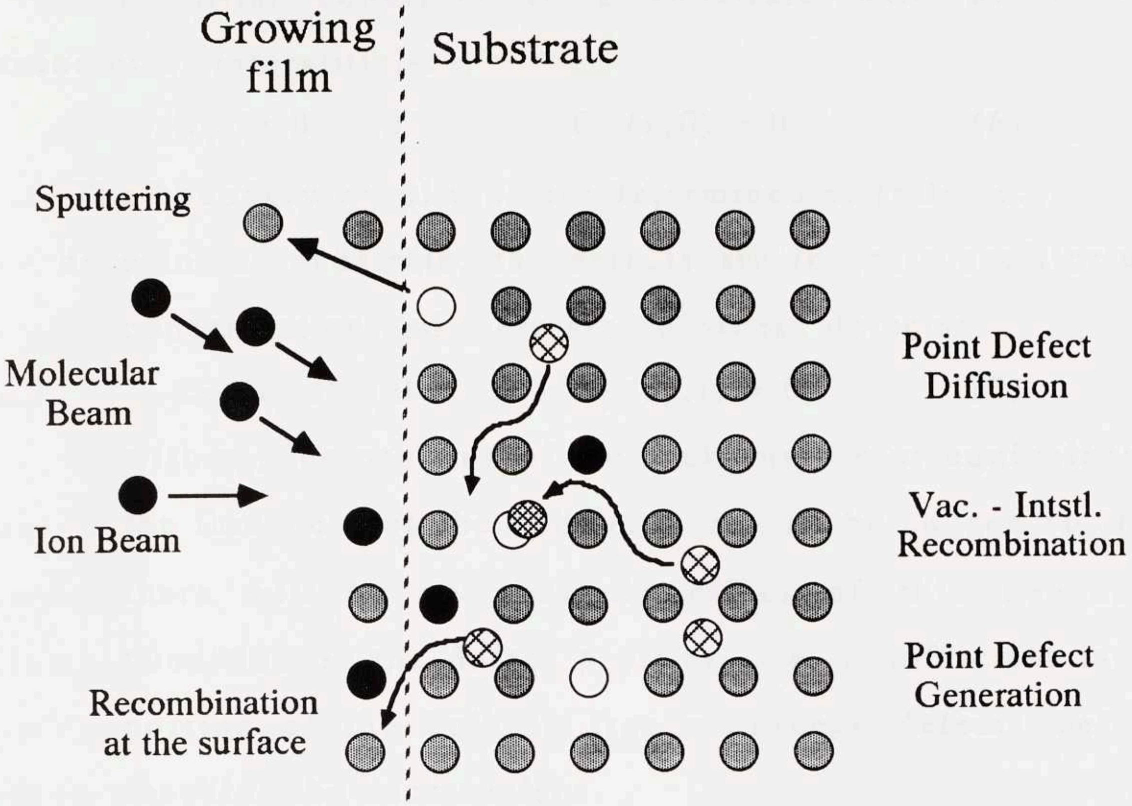

Figure 4.1. Illustration of the processes accounted for in DRIVIC

is sputtered). The sputtering rate is accounted for by the defect generation terms G_V and G_I. In the collision cascade, the same number of vacancies and interstitials are created but some of the created interstitials can escape from the solid, reducing the number of interstitials left in the substrate and corresponding to actual removal of material. The net material incorporation rate X per incoming ion in the case of homodeposition by IBD is then related to the sputtering yield, S, and to the numbers of vacancies, N_V, and interstitials, N_I, created per ion by:

$$X = 1 - S = N_I - N_V \qquad (5)$$

This net material incorporation rate can be considered as the theoretical maximum growth rate achievable in IBD.

The initial condition is a substrate with no excess vacancies or interstitials:

$$C_V\ (z,0) = 0 \qquad C_I\ (z,0) = 0 \qquad (6)$$

The boundary conditions are determined as follows:

- deep in the substrate, the defects are in their equilibrium concentration and there are no excess defects:

  $$C_V\ (z_b,t) = 0 \qquad C_I\ (z_b,t) = 0 \qquad (7)$$

  with z_b, the position of the back surface or equivalently the thickness of the substrate. z_b can be chosen so that there will be no parasitic effect of this boundary condition on the defect profiles, i.e. a sufficient large portion of the bulk is free of excess defects before reaching the back surface.
- at the growing surface, i.e. at $z = z_s$, the surface acts as a perfect sink and all the defects recombine with an infinite recombination speed; in other words, once a defect has reached the surface, it cannot be reintegrated in the substrate and is annihilated. This corresponds to the following boundary conditions:

  $$C_V\ (z_s,t) = 0 \qquad C_I\ (z_s,t) = 0 \qquad (8)$$

The continuity equations (1) and (2) and the growth rate equation (3) are non-linear and coupled to each other. We use a finite element method to solve them with an implicit self-consistent iteration scheme. Particular care was taken to minimize the numerical errors. We indeed observed that numerical imprecisions corresponded physically to an artificial generation or recombination of point defects. By keeping track of all the species, the numerical imprecisions could be evaluated. The solution scheme, the discretization grid and the time step were optimized in the simulations to keep the numerical error to a minimum, (usually less than 10 % of the residual interstitial incorporation).

Two assumptions made in this model must be pointed out: first, we neglected the formation of divacancies or other extended defects, based on the assumption that the recombination between vacancies and interstitials is the dominant phenomenon, preventing the formation of such extended defects [97]. Second, the stress fields due to the supersaturation of interstitials and vacancies at different locations are neglected but they can be introduced as an additional interaction term in the continuity equations.

In the case of heterodeposition without chemical reaction, i.e. IBD of species B on substrate A resulting in a structure $B/A_{1-x}B_x/A$, such as IBD of Ge on Si, continuity equations similar to (1) and (2) must be written for all the species involved in the growth: vacancies of A and B and interstitials of A and B, with coefficients like diffusivity ($D_{V,A}$, $D_{I,A}$, $D_{V,B}$, $D_{I,B}$) and capture radius ($r_{V,A-I,A}$, $r_{V,B-I,B}$, $r_{V,A-I,B}$ if the recombination of I_B with V_A is possible and vice-versa) dependent on their position (in A, B or $A_{1-x}B_x$). This is a rather complex but solvable problem using the above formalism.

4.2. RESULTS

DRIVIC in conjunction with TRIMCSR was used to perform calculations of IBD of Si on Si for ion energies ranging from 10 eV to 10 keV. The diffusion coefficients for vacancies and interstitials are from Gösele and Tan [98] based on high temperature experiments:

$$D_V = 0.1\, e^{-2\,\mathrm{eV}/kT} \qquad D_I = 10^{-5}\, e^{-0.4\,\mathrm{eV}/kT} \qquad \mathrm{cm}^2/\mathrm{sec}$$

These coefficients correspond to interstitials mobile even at 300 K with D_I equal to 2×10^{-12} $\mathrm{cm}^2/\mathrm{sec}$, and to vacancies totally immobile at 300 K ($D_V = 10^{-34}$ $\mathrm{cm}^2/\mathrm{sec}$) and only diffusing significantly above 800 K. These values correspond to our physical understanding of self-diffusion in silicon (slow moving vacancies and highly mobile interstitials at low temperature). However, these diffusivities are still controversial [99] and the dependence of the IBD growth process on the point defect diffusivities will be addressed in § 4.4.

a. DESCRIPTION OF IBD GROWTH

Simulation results in Fig. 4.2 illustrate the mechanism of thin film growth by IBD. The vacancies and interstitials profiles are shown after 1, 10 and 20 seconds of exposure to a 40 eV Si ion beam with a fluence of 10^{14} ion/cm^2/sec at 300 K. The IBD growth mechanism can be accounted for by the interstitial motion. Three different diffusion paths are possible:

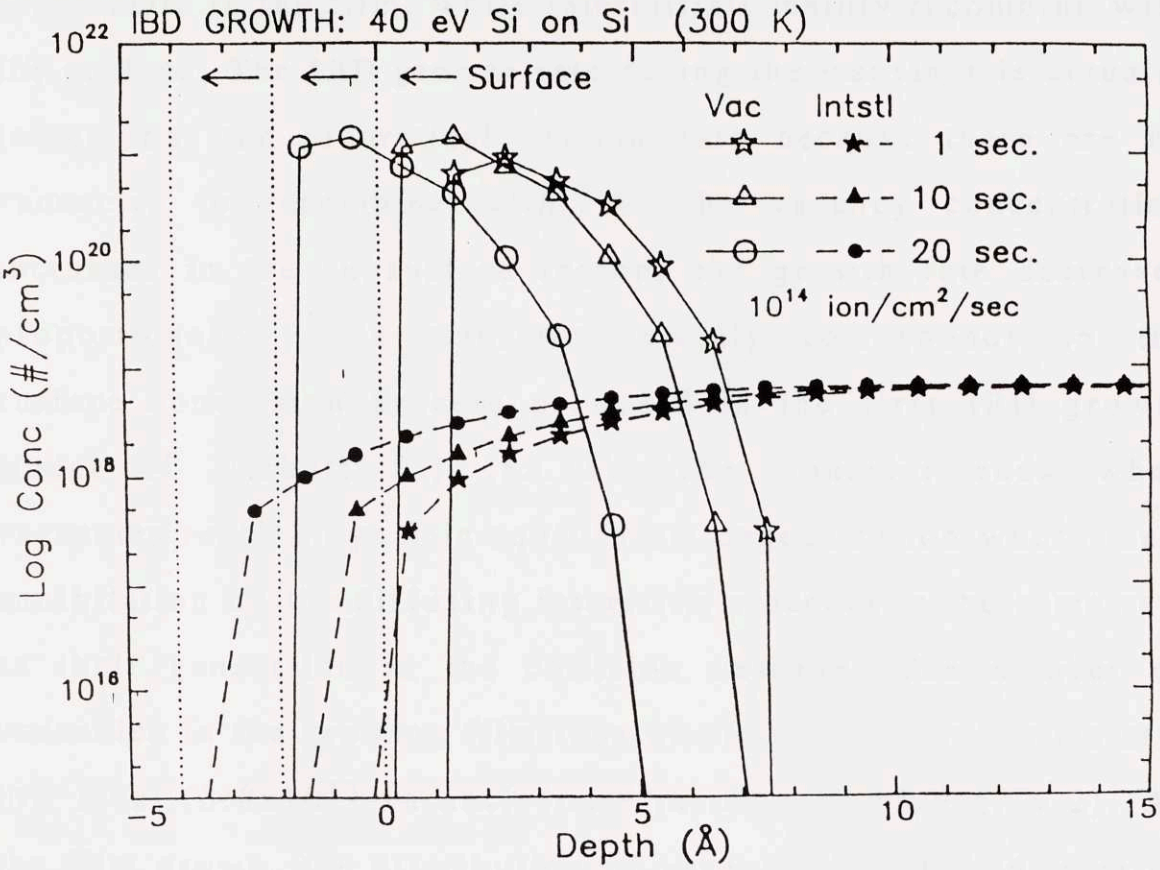

Figure 4.2. Vacancy and interstitial profiles at different times of IBD growth of Si on Si at 300 K, 40 eV, and 10^{14} ion/cm^2/sec. The dotted lines indicate the surface positions of the growing film.

1) The interstitials can first recombine with the nearby surface, leading to net growth of the IBD film. This is schematized by the dotted lines which represent the surface location at different times. In a first approximation, the IBD growth rate is equal to the theoretical growth rate given by the net material incorporation X, in this case 0.2 Å/sec.

2) While diffusing towards the surface, interstitials can also recombine with vacancies, leading to vacancy annihilation in the growing film. Before steady state, the IBD growth process goes through the following transient: vacancies first

accumulate in the film, while interstitials mainly recombine with the surface. The IBD growth rate during the transient is actually larger that the theoretical growth rate because there are no vacancies to recombine with. As the vacancy concentration increases in the subsurface region, the growth rate decreases proportionally. This transient actually corresponds to the surface conversion process proposed in the first IBD growth model of Herbots [5] (§2.1a). The transient ends when vacancies reach a dynamic equilibrium concentration where their annihilation by the diffusing interstitials occurs at the same rate as their generation in the collision cascade. The number of vacancies in the growing film then stays constant over time at a low level (3.8×10^{13} vacancies/cm^2 in the case of Fig. 4.2). As the film grows, the distribution of vacancies is shifted towards the surface with no vacancies left behind in the film, as shown in Fig. 4.2. This is due to the very low diffusivity of the vacancies and their complete annihilation by the interstitials.

3) Lastly, a small fraction of interstitials are diffusing into the substrate. This accumulation deeper in the bulk is small compared to the interstitial generation by the ion bombardment: at 40 eV, the interstitial incorporation rate is 8×10^{12} int/cm^2/sec while 1.8×10^{14} int/cm^2/sec are created by the ions. The accumulation of interstitials in the bulk correlates with the experimental observation of interstitial dislocation loops buried some 250 to 4000 Å in the substrate [6,7] (Fig. 4.3a). To explain this precipitation of interstitials at some *specific* depth, a term representing the diffusion-limited trapping [100] of

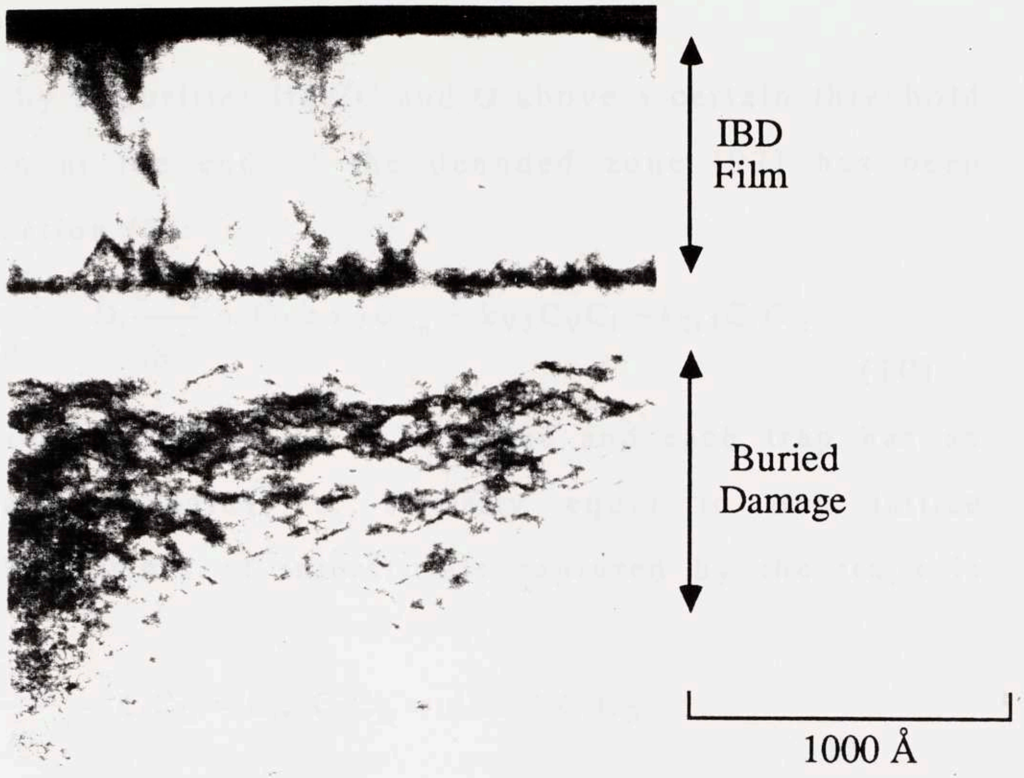

Figure 4.3. (a) TEM micrograph of Si IBD film (20 eV Si → Si, 400 °C) showing the residual damage identified as interstitial dislocation loops at a specific depth of 250 to 1250 Å below the original interface [6]

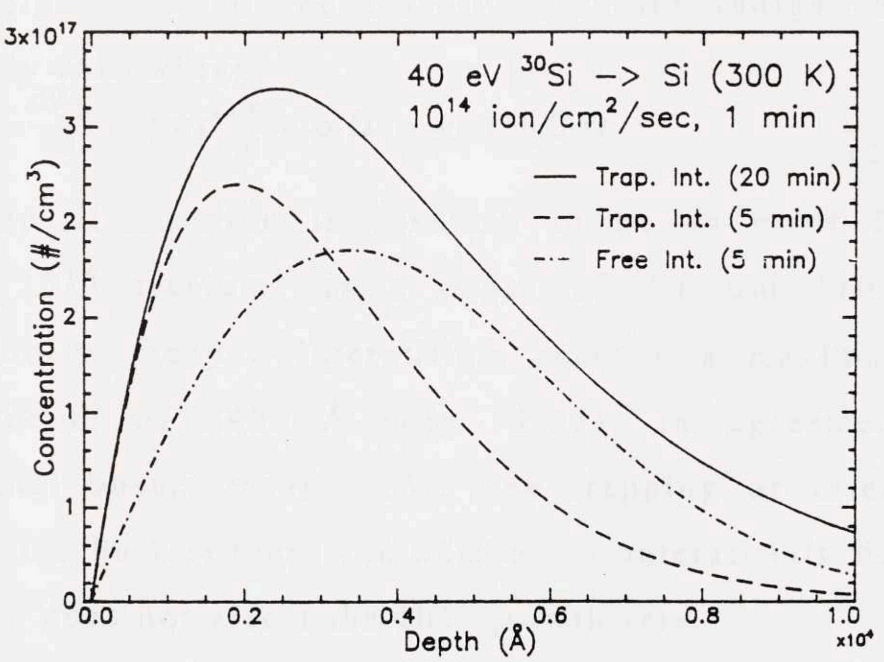

Figure 4.3. (b) Computed distribution of trapped interstitials showing the defect precipitation at a specific depth of 2400 Å when the trap distribution is an error function with 10^{16} traps/cm^3 at 10 μm [101]. IBD growth is calculated for 1 min, 40 eV Si, 10^{14} ion/cm^2/sec at 600 K. The distributions of free and trapped interstitials are shown 5 and 20 min after growth, with all the interstitials being trapped after 20 min.

interstitials by impurities like C and O above a certain threshold concentration at the end of the denuded zone [97] has been added to equation (2):

$$\frac{\partial C_I}{\partial t} = D_I \frac{\partial^2 C_I}{\partial z^2} + G_I(z-z_s)\,\phi_{ion} - k_{V\text{-}I} C_V C_I - k_{Tr\text{-}I} C_I C_{Tr} \tag{10}$$

A distribution of traps, C_{Tr}, is assumed and each trap has an effective capture radius, r, initially equal to one lattice constant. The number of interstitials captured by the traps is given by:

$$\frac{\partial C_{Itr}}{\partial t} = \phi_I C_{Tr} = k_{Tr\text{-}I} C_I C_{Tr} = 4\pi r D_I C_I C_{Tr} \tag{11}$$

ϕ_I is the interstitial flux at the surface of the traps. Each captured interstitial increases the volume of a trap by one atomic volume Ω and the effective capture radius increases accordingly following:

$$\frac{dV_{Tr}}{dt} = 4\pi r^2 \frac{dr}{dt} = \phi_I \Omega = 4\pi r D_I C_I \Omega \tag{12}$$

If the trap distribution is assumed to be an error function reaching 10^{16} trap/cm^3 at a depth of 10 μm [101], the distribution of trapped interstitials reaches a maximum at a specific depth of 2400 Å (Fig. 4.3b), in agreement with experimental observations [5,6]. The trapping of interstitials deeper in the bulk reduces the number of interstitials diffusing freely, but does not affect the IBD growth rate.

To keep track of the generated defects, the following balance relations can be written. The interstitials created per incoming ion, N_I, can either recombine with the surface, $N_{I\text{-}S}$, or annihilate vacancies, $N_{I\text{-}V}$, or accumulate in the bulk, α_I. N_I is also related to the net material incorporation rate X, the number of vacancies per ion N_V, and the sputtering rate S.

$$N_I = N_{I\text{-}S} + N_{I\text{-}V} + \alpha_I = X + N_V = 1 + N_V - S \quad (13)$$

$N_{I\text{-}V}$ is equal to the number of vacancies annihilated by the interstitials: $N_{V\text{-}I} = N_{I\text{-}V} = N_V - \alpha_V$, where α_V is the vacancy accumulation rate in the bulk. The fraction of interstitials recombining at the surface and forming the IBD film can then be expressed as:

$$N_{I\text{-}S} = 1 - S - \alpha_T, \quad (14)$$

where $\alpha_T = \alpha_I - \alpha_V$ represents a modification of the IBD growth rate due to the accumulation of point defects in the structure. During the transient, the vacancies are accumulating in the subsurface region at a rate α_V. α_T is then negative, explaining why the IBD growth rate is larger at first. At steady state, the vacancies are in dynamic equilibrium and do not accumulate: $\alpha_V = 0$ and $\alpha_I = \alpha_T$. The physical meaning of that relation is that the IBD growth rate is equal to the material incorporation rate, i.e. the ion beam flux minus the sputtering rate, reduced by the small fraction of interstitials accumulating in the bulk.

When the ion beam is turned off, vacancy and interstitial concentrations begin to decrease rapidly by recombination of the defects with each other and with the surface. The thickness of the IBD film actually continues to increase but at a rate macroscopically negligible (10^{-3} Å/sec) and decaying rapidly. The total defect incorporation in the resulting structure is a small fraction of the total dose of injected defects (1 %). This athermal annealing of defects is due to the high mobility of interstitials at low temperature and leads to the epitaxial nature of thin films grown by IBD.

b. DEPENDENCE OF IBD GROWTH ON THE ION ENERGY

Simulations results in Fig. 4.4 show the dependence of the IBD growth rate on the ion energy.

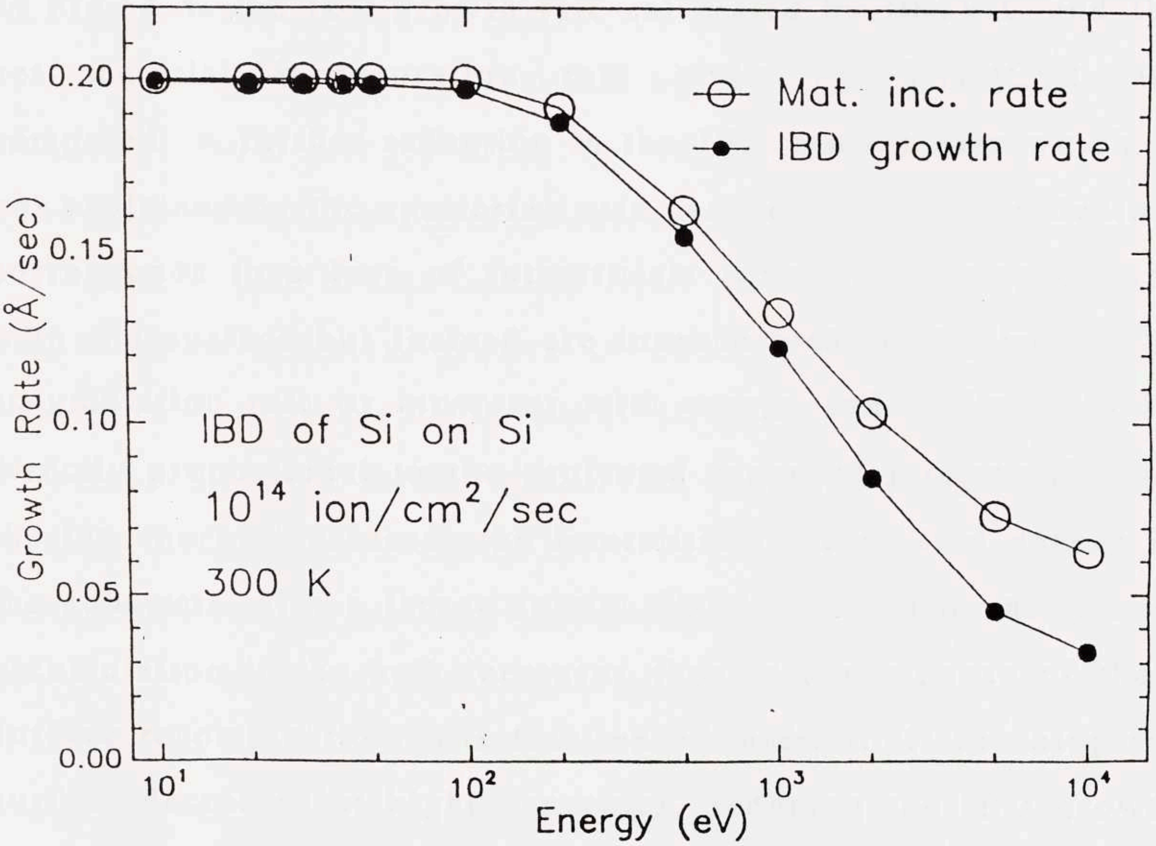

Figure 4.4. Dependence of the IBD growth rate on the ion energy (300 K, 10^{14} ion/cm^2/sec). Above 200 eV, the IBD growth rate (closed circles) deviates from the net material incorporation rate given by TRIMCSR (open circles), due to an increased incorporation of interstitials in the bulk.

Below 100 eV, the IBD growth rate is independent of the ion energy and, in a first approximation, is limited only by the ion beam fluence (in the case of Fig. 4.4: 10^{14} ion/cm^2/sec or 0.2 Å/sec). Above 100 eV, the IBD growth rate begins to decrease. The question is whether this decrease can be solely attributed to the increasing sputtering yield.

As explained earlier, the IBD growth rate would be equal to the net material incorporation rate, $X = 1 - S$, if no excess interstitials were lost due to extra recombination with accumulated vacancies or to accumulation in the bulk ($\alpha_T = 0$). In Fig. 4.4, the IBD growth rate calculated by DRIVIC and the net material incorporation rate given by TRIMCSR are compared. A further reduction in the IBD growth rate which is not explained by the sputtering rate can be seen. This reduction corresponds to a loss of interstitials which do not recombine with the surface but instead are incorporated in the bulk. The accumulation rate α_I *increases* with energy and is found to be directly proportional to the projected range of interstitials. As the ion energy increases, the interstitials are created deeper in the substrate with a larger spatial distribution. The interstitial accumulation in the bulk increases then at the expense of their surface recombination. The fraction of interstitials reaching the surface decreases at higher energies, reducing the IBD growth rate. This effect becomes significant already at 200 eV and reduces the IBD growth rate at high energy by as much as 50 %.

Moreover, as the ion energy increases, the dynamic equilibrium concentrations of vacancies increase to higher levels. Above a threshold energy, the vacancy concentrations reach the amorphization level of 0.02 to 0.04 displacements per atoms (d.p.a.) or 1 to 2x10^{22} vac/cm^3 in the case of Si. At 300 K and with the point defect diffusivities assumed above, the threshold energy for amorphization is found to be 500 eV. Below 500 eV, epitaxial growth is possible, while at 500 eV and above, the film has to be amorphous. The dependence of the vacancy concentrations on the ion energy can be explained as follows. The vacancy annihilation is limited by the interstitial diffusion. At lower energies, the spatial separation between interstitials and vacancies created by the ions is smaller than at higher energies. The pair recombination is therefore more efficient at low energy, since the interstitials need to diffuse over smaller distances to annihilate a vacancy.

This result brings a new light on the energy threshold below which epitaxial growth is possible by IBD. The main limitation on the deposition energy is that the defect generation has to be confined in the subsurface region in order to favor surface recombination which leads to net growth, and vacancy annihilation which prevents amorphization. In other words, net growth can occur at relatively high energy with Si, but good epitaxy can only happen below 200 eV, in agreement with experimental work of different groups on IBD of Si [3-9]

4.3. CORRELATIONS WITH EXPERIMENTAL RESULTS

As mentioned above, several experimental observations can be correlated with the simulation results. In addition, good agreement was found between the growth rate predicted by DRIVIC and experimental values obtained by Herbots et al. [5-7]. In that case, the growth rate was 0.1 Å/sec for an ion beam fluence of approximatively $5x10^{13}$ ion/cm^2/sec. This epitaxial growth rate was also limited by the ion beam fluence and was temperature independent between 350 °C and 600 °C.

Cross-section Transmission Electron Microscopy (TEM) observations and Rutherford Backscattering Spectrometry (RBS) measurements combined with ion channeling showed that the deposited films were epitaxial, while buried defects were observed deeper in the substrate (Fig. 4.3a). At 400 °C and below, the channeling minimum yield in the Si <110> direction was fairly constant throughout the film but never dropped below 4 %. This means that at least 1 % of the atoms in the film were displaced from the lattice sites. For films grown at 600 °C and higher, the minimum yield increased between the surface and the interface but the subsurface region reached the virgin crystal value of 3 %, while the yield at the deeper side of the film reached higher values. These differences in defect distributions were confirmed by cross-section TEM observations and show that at low temperature, interstitials are more uniformly trapped throughout the film, while at higher temperatures, they migrate and coalesce into larger clusters. It was also found by X-ray diffraction that the films were uniaxially strained, due to the large remaining concentration of interstitials in the films. These experimental observations of residual defects present in the film and the substrate, correlate with the simulated interstitial profiles remaining in the structure after growth (Fig. 4.3b). Although the spatial location of the buried defects could be accounted for by our model of diffusion-limited trapping of the interstitials, the temperature dependence of the buried defect distribution could not be reproduced, suggesting that other processes such as thermally activated nucleation and precipitation of the interstitial dislocation loops may be taken place.

4.4. DISCUSSION

The diffusivities of point defects in silicon are still a controversial issue. Therefore, the effect of choosing different values for D_I and D_V on the previous results was investigated, with special emphasis on the dependence of the IBD growth process on the ion energy.

a. EFFECT OF INTERSTITIAL DIFFUSIVITIES ON THE IBD GROWTH PROCESS

When the interstitial diffusivity is decreased from a high value 10^{-10} to an intermediate low value 10^{-16} cm^2/sec, while keeping the vacancies immobile ($D_V = 10^{-34}$ cm^2/sec), the IBD growth rate is found to be highly dependent on the interstitial diffusivity as shown in Fig. 4.5. With lower interstitial diffusivities, the IBD growth rate is a strong function of the ion energy, decreasing rapidly as the ion energy increases. The vacancy concentrations increase to very high levels since their annihilation is limited by the slower diffusion of interstitials. The threshold energy for amorphization decreases then with

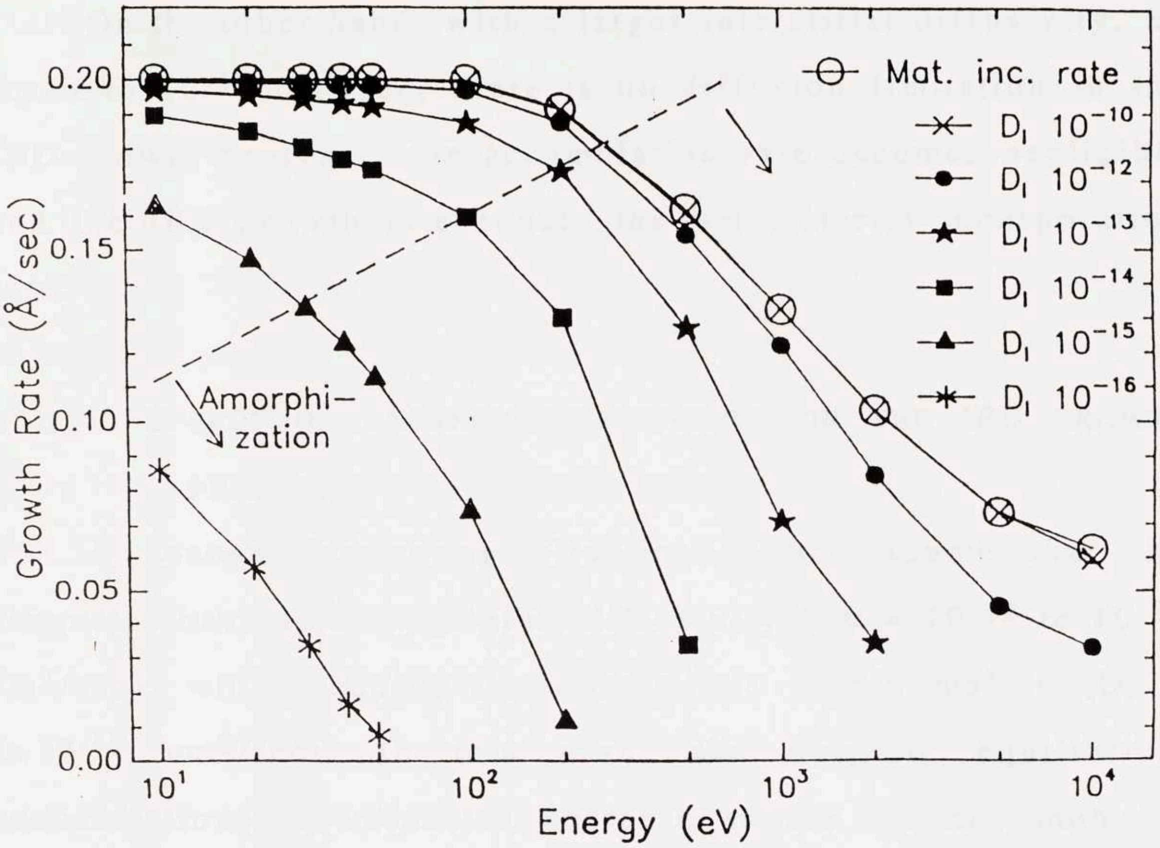

Figure 4.5. Dependence of the IBD growth rate on the ion energy for different interstitial diffusivities (D_I). In the region under the dotted line marked "amorphization", the vacancy concentrations reach the amorphization level of 0.04 d.p.a., leading to the collapse of the Si lattice.

decreasing D_I, as illustrated in Fig. 4.5 by the delimitation of the region where amorphization occurs. Similarly, the interstitial accumulation rate in the bulk, α_I, increases with decreasing D_I. After exposure to the ion beam, these accumulated interstitials diffuse and can reach the surface, contributing significantly to the growth. The resulting thickness is therefore larger than the film thickness just after the IBD is interrupted. This is to be considered when experimental growth rate are compared to calculated growth rate.

On the other hand, with a larger interstitial diffusivity, D_I equal to 10^{-10} cm^2/sec, there is no diffusion limitation in the IBD growth process: the accumulation rate becomes negligible and the IBD growth rate equals the net material incorporation rate.

b. EFFECT OF VACANCY DIFFUSIVITIES ON THE IBD GROWTH PROCESS

A second interesting situation is to assume that the vacancies have a non negligible diffusivity (D_V = 10^{-12} to 10^{-18} cm^2/sec), while keeping the interstitials highly mobile (D_I = $2x10^{-12}$ cm^2/sec). In this case, the dynamic equilibrium concentrations of vacancies decrease as the vacancy mobility increases, since they can recombine with the nearby surface. The threshold energy for amorphization accordingly increases with increasing D_V and would be larger than 10 keV for D_V larger than 10^{-14} cm^2/sec.

At energies lower than 200 eV, the IBD growth rate is not affected by a larger vacancy diffusivity. However, at higher energies, it is lower due to the increasing number of vacancies created close to the surface, while interstitials are generated deeper in the bulk. Since vacancies can recombine with the surface, more interstitials correspondingly accumulate in the bulk. When the ion beam is turned off, a fairly large number of interstitials diffuse to the surface, leading to a significant growth of the film. The resulting film has about the same final thickness and the same amount of accumulated interstitials in the bulk.

The above considerations combined with experimental results of IBD can provide an interesting mean to determine better values for point defect diffusivities in silicon at temperatures between 300 K and 1000 K. On the other hand, the good correlation between experimental observations and the simulation results obtained with the diffusivities of Gösele and Tan indicates that these values are reasonably close to reality, at least to account for IBD experiments.

One might wonder, however, if it is not just a coincidence that the diffusivities of Gösele and Tan seem to be appropriate, and if actually, the point defect diffusivities do not result from other processes, such as thermal spike effects for example. Thermal spikes [102,103] consist of briefly lived excursions to high temperatures in the ion-solid interaction volume. The temperature rise ΔT is given by the energy deposited per ion in the cascade volume [103]:

$$\Delta T \approx E_{ion} / 3k_B \, \Omega \, \Delta x \, \Delta y^2$$

where $3k_B$ is the atomic heat capacity, Ω the atomic density, and Δx and Δy the longitudinal and lateral straggling of the damage profile, respectively. The temporal and spatial evolution of the temperature spike can then be determined by solving the classical equation of heat conductivity [103]:

$$\frac{\partial T}{\partial t} = \frac{\partial}{\partial x}\left(\kappa \frac{\partial T}{\partial x} \right)$$

where κ is the thermal diffusivity. In the case of IBD, namely for 40 eV Si ions into Si, the temperature spike is calculated to be $\Delta T \approx 3000$ K and is dissipated in less than 10^{-10} sec. This extremely short heat pulse cannot explain the IBD processes of thin film growth and buried damage incorporation, which both require diffusion on a much longer time scale and over distances significantly larger than the ion-solid interaction volume (see also § 4.5). We thus do not believe that an approach based on thermal spikes can provide an appropriate physical model to describe thin film growth by IBD. We may not rule out though, that modification of the vibrational energy due to the ion-solid interaction and/or electronic recombination processes which are important for diffusion in semiconductors can affect the point defect diffusivities during IBD growth.

Nevertheless, the important point shown by our simulations with DRIVIC and the correlation with experimental observations is that epitaxial growth by IBD can be understood as resulting from a high diffusivity of the interstitials and a low diffusivity of the vacancies at the IBD growth temperatures. These point defect diffusivities happen to be well described by the values proposed by Tan and Gösele.

4.5. A GLIMPSE INTO THE IBD ATOMISTICS BY MONTE-CARLO SIMULATIONS: MCIBD

a. DESCRIPTION OF THE MCIBD MODEL

The advantage of DRIVIC is its ability to simulate a growth of long duration and to investigate the effect of the different parameters, such as ion energy and point defect diffusivities, on the IBD growth kinetics. Unfortunately, little information can be obtained on the microstructure of the film. In order to obtain such information, atomistic computation of the IBD process must be performed. Two different computational methods can be used: Molecular Dynamics (MD) or Monte-Carlo (MC) simulations.

In Molecular Dynamics simulations, the evolution with time of an ensemble of atoms is calculated according to the mechanical laws which govern their movement. MD calculations have been performed on the interaction between ion and solid at the low energy range (< 50 eV) or up to 100 eV under special conditions (grazing incidence angle of the ion) [85]. At higher energy, several problems arise.

1) The use of two- and three-body potentials is not valid anymore because of the increasing importance of collective effects.
2) The rapid transfer of kinetic energy of the ion to potential energy in the system must be accurately described: with the available potentials, the energy dissipation in a very short time scale makes the simulation box literally explode upon penetration of the ion.

3) Both the repulsive and attractive parts of the interatomic potential must be accurately accounted for.

These problems are interrelated and indicate that the atomic potentials presently available to calculate the forces between atoms, such as the Stillinger-Weber potential, are not valid to describe the interaction of an energetic particle with a solid.

The other approach to atomistic calculations is based on Monte-Carlo techniques (MC). MC techniques are not deterministic but statistical in nature. Random processes are simulated and their average over time and number of simulations provides a valid description of the physical phenomena involved. MC calculations are between rigorous MD calculations and our previous continuum model. They are able to some extent to simulate long growth time but can provide an atomistic description of thin film growth using low energy ion beams. We chose this approach and will present very simplistic calculations of IBD of Si on Si making drastic, although appropriate, assumptions governed by the experimental results and the simulation results of the continuum model.

Our Monte-Carlo program to describe IBD growth, called MCIBD (see simplified flow chart in Fig. 4.6), simulates the point defect generation in the collision cascade using the TRIMCSR results, and the diffusion and recombination of these defects. The simulation is made for a two-dimensional (2D) (100) face of a FCC lattice representing the Si substrate

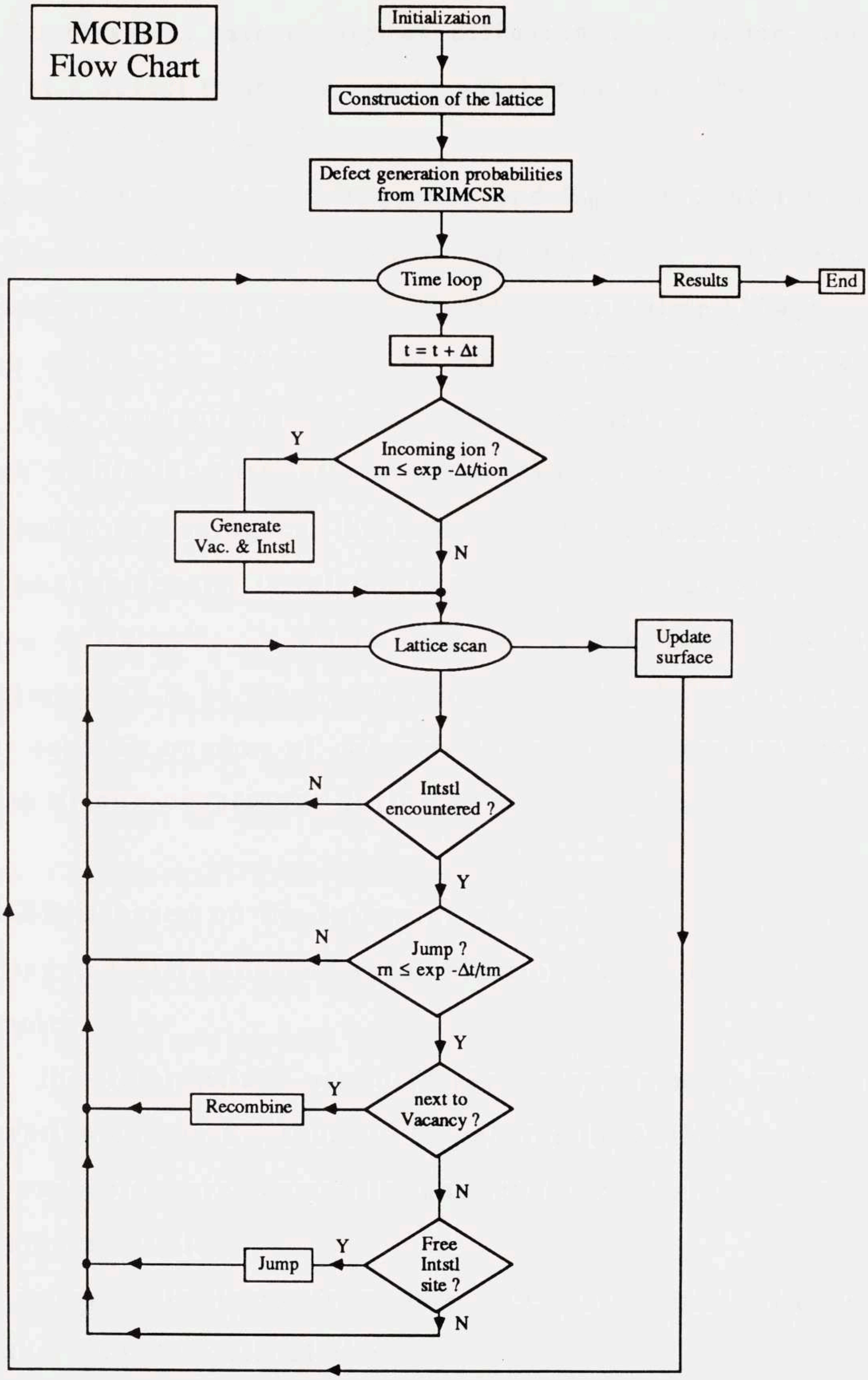

Figure 4.6. Flow chart of MCIBD

In the classical rate theory of diffusion in a lattice, the jump rate of a defect from one site to another is given by

$$\omega_m = \omega_0 \exp\left(-E_m / kT\right)$$

where ω_0 is the attempt frequency and E_m is the migration energy. The jump of the defect is described as a Poisson process with a constant number of events per unit time [104]:

$\omega_m = 1/\tau_m$, where τ_m is the average time interval between two consecutive jumps. The probability of non-occurrence within the time interval Δt is equal to: $\exp(-\Delta t/\tau_m)$.

A similar reasoning can be made for the incorporation of an ion. The time density is related to the ion beam flux by:

$\tau_{ion} = 1/\phi_{ion}/n_s$, where ϕ_{ion} is the ion beam flux in monolayer/sec and n_s is the monolayer atomic density (or in our particular case the number of columns in the 2D lattice) and the probability of non-occurrence during Δt is $\exp(-\Delta t/\tau_{ion})$.

MCIBD is based on the following assumptions:

a) regarding the diffusion and recombination of the interstitials and vacancies:

- only the interstitials are diffusing significantly with a migration energy E_m equal to 0.4 eV (as in DRIVIC)
- the vacancies are immobile and their diffusion is not considered at all
- the interstitials jump from one FCC interstitial site to another FCC interstitial site

- the recombination of an interstitial with an adjacent vacancy is more probable than a jump to a vacant interstitial site and will preferentially occur
- only nearest neighbor interactions are considered: the interstitial can recombine with a vacancy or jump to a free interstitial site within one nearest neighbor distance, but no influence of the second site is taken into account. Physically, this is equivalent to choose a capture radius of $a_0/2$ instead of a_0, where a_0 is the interatomic distance.

b) regarding the surface:

- no diffusion of the adatoms on the surface is considered. This is valid in a first approximation for the low growth temperatures possible in IBD.
- a free surface site is treated as a vacancy, with preferential recombination of the interstitial compared to jump to another interstitial site. There are no interstitial sites on the surface.
- an interstitial which has recombined with a surface vacancy is annihilated and cannot be reintegrated as an interstitial in the substrate
- no dimerization or other surface reconstruction is taken into account

c) regarding the diffusion to the bulk:

- an interstitial diffusing in the bulk cannot be reintegrated in the subsurface region and is considered as accumulating deeper in the substrate

Periodic boundary conditions are assumed on the left and right sides of the FCC face. An interstitials disappearing on the right reappears on the left.

All these assumptions make the present MC calculations relatively simplistic, but can be eliminated in more elaborate versions. In particular, a relatively important improvement of the program is to make a three-dimensional (3D) version taking into account the diamond structure of the Si lattice. Different configurations [105] and diffusion paths [106,107] can be considered for the interstitials, while the vacancy diffusion can be introduced. The surface dimerization and reconstruction [108,109] as well as diffusion of the adatoms [110] can be added with appropriate activation energy and attempt frequency determined from MD calculations [111].

Moreover, this Monte-Carlo approach is compatible with minimum energy calculations of the intermediate atomic configuration and thermal relaxation towards equilibrium. It also allows one to investigate the relative importance of the different processes leading to epitaxy by studying the effect of parameters such as point defect diffusivities, adatom diffusivity, dimerization energies, and so on.

b. MCIBD SIMULATIONS OF IBD OF SI ON SI

Using MCIBD, the IBD growth of Si on Si was calculated as a function of ion energy, for 10 sec of ion bombardment at 300 K with a flux of 1 monolayer/sec on a 40x40 2D lattice. The evolution of the 2D lattice is shown in Fig. 4.7 where x represent atoms on their lattice site, and * represent interstitials.

At 40 eV (Fig. 4.7a), the lattice is preserved as the IBD film grows. The interstitials migrate preferentially to the surface where they are annihilated, leading to net thin film growth. The vacancies are also progressively annihilated in the growing film, resulting in a fairly unperturbed lattice. At 200 eV (Fig. 4.7b), more vacancies are left behind in the growing film, and the integrity of the lattice is greatly reduced. At 1 keV (Fig. 4.7c), after some time of IBD growth, the lattice arrangement appears completely lost, with an overwhelming concentrations of vacancies which are not annihilated by the interstitials. There is no doubt that there would be in such conditions collapse of the lattice with subsequent amorphization.

This evolution of the lattice configuration with ion energy correlates qualitatively with our previous conclusions derived with DRIVIC on the threshold energy for amorphization. It can also be attributed to the increase at higher ion energies of the range and range straggling, both longitudinal and lateral, of the respective vacancy and interstitial creation profiles.

No further quantitative interpretation of the MCIBD results will be attempted at this point. These simulations fulfilled however their purpose in helping us understand and visualize the atomistic processes involved in IBD growth.

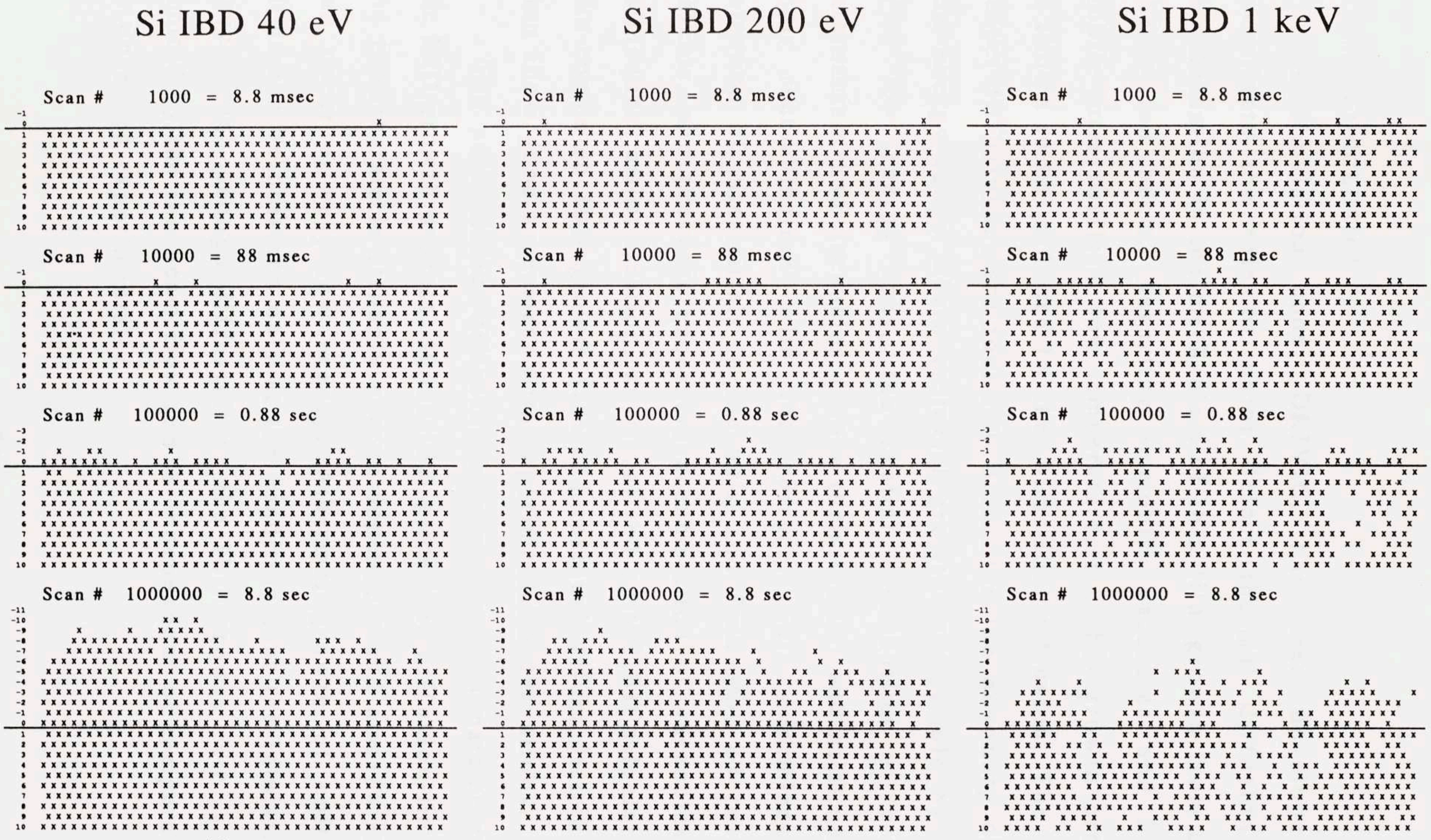

(a) (b) (c)

Figure 4.7. MCIBD simulations of IBD growth of Si on Si (100) for different ion energies. Total simulation time: 10 sec; Ion beam flux: 1 ML/sec; Time step Δt: 8.8 μsec/scan The straight line represents the location of the original surface.

4.6. CONCLUSION

A simulation code, DRIVIC, has been developed to investigate the role of point defect thermal diffusion and recombination in the mechanism of thin film growth from a low energy ion beam. Assuming immobile vacancies and highly mobile interstitials at low temperature, the IBD growth process is shown to be mediated by the interstitial diffusion. The point defect diffusivities are found to determine the boundary of the low energy range where epitaxial growth is possible by IBD. With low energy ions, the spatial distribution of created interstitials and vacancies favors their mutual annihilation and their recombination with the surface. This minimizes the injection of interstitials in the bulk and formation of residual defects, and prevents excessive accumulation of vacancies and subsequent amorphization, as visualized by MCIBD calculations. The computed IBD growth rate and residual defect distribution also show good agreement with experimental observations.

The point defect diffusivities are important parameters in the IBD growth process. If the IBD growth is diffusion-limited, the growth rate is strongly energy dependent and amorphization can occur at very low energy. Athermal growth of epitaxial films can be obtained only at the condition that the interstitials have a high enough diffusivity: the IBD growth rate is then limited by the ion beam flux and is independent of temperature, as observed experimentally.

The high diffusivity of the interstitials playing a major role in ion beam epitaxy has very recently been confirmed by MD calculations [112]. The interstitials were shown to diffuse preferentially toward the surface and to annihilate the vacancies created by the ions. The activation energy for interstitial diffusion was lower than 1.4 eV and decreased in the subsurface region. The good agreement between relatively complex and time consuming MD calculations and our conceptually simple continuum (DRIVIC) and Monte-Carlo (MCIBD) simulation programs shows that our computer models can be used to gain insight into the epitaxial growth mechanism by IBD.

5. EXPERIMENTAL STUDY OF IBO OF SEMICONDUCTORS

In the present work, the growth of thin oxide films of group IV semiconductors, Si, Ge and their alloy $Si_{1-x}Ge_x$, and of the III-V semiconductor GaAs was investigated by IBO at room temperature. Special emphasis was placed on the determination of the dependence of phase formation and film properties upon ion energy. The experimental procedures and results are first presented for the group IV semiconductors then for GaAs.

5.1. ION BEAM OXIDATION OF SI, GE, $SI_{1-X}GE_X$

All the experiments were performed in the CIMD laboratory which comprises a multi-chamber UHV system and a wet chemical cleaning hood, both installed in a clean room environment in order to minimize contamination by particulates. The UHV system (Fig. 5.1) consists primarily of a MBE system dedicated to group IV semiconductors and designed for 3" wafers and an analytical chamber with XPS, connected by a UHV transfer tube.

Before presenting the IBO experiments, it is useful to describe the $Si_{1-x}Ge_x$ sample preparation by chemical cleaning and MBE growth, as well as some modifications implemented in the XPS chamber in order to perform the IBO experiments with in situ monitoring by XPS.

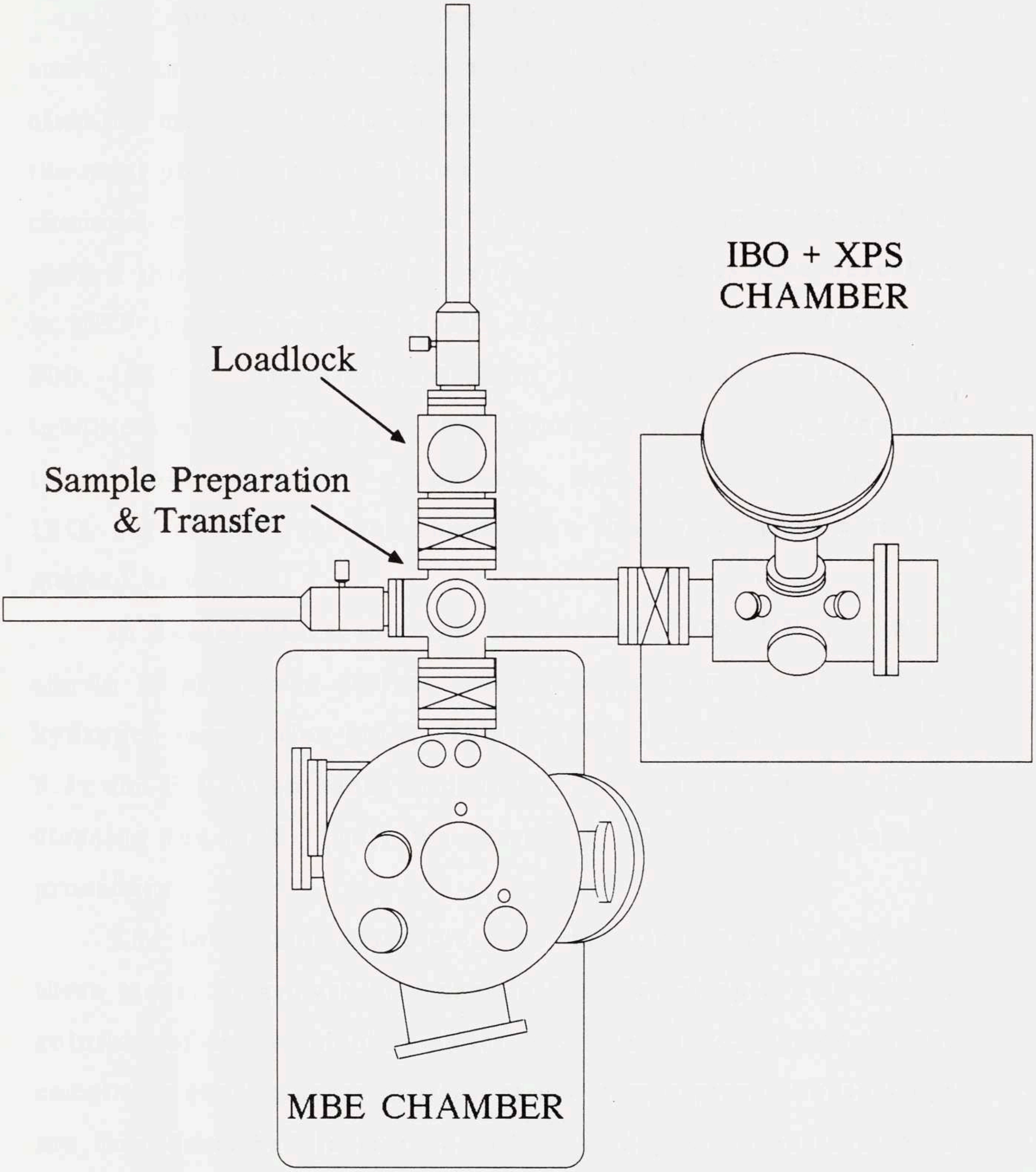

Figure 5.1. Layout of the CIMD system

a. SAMPLE CLEANING

The purpose of cleaning the samples is to produce a surface that will allow epitaxial growth by MBE. Several cleaning methods have been proposed in the past [113]. One of the most popular is the "Shiraki clean" [114]. It first involves a chemical clean to remove the carboneous contaminants and to grow a thin (10 Å) chemical oxide. This oxide is then desorbed in UHV just before MBE growth by heating the Si wafer up to 800 - 850 °C. The disadvantage of this cleaning method is to involve a high temperature step. Since we are investigating low temperature processing techniques, such as IBD, CIMD and IBO, our cleaning method should be a low temperature cleaning method as well.

In recent years, etching Si surfaces with HF has been shown to produce a surface free of oxygen and passivated by hydrogen termination [115]. This property has been exploited by P.J. and F.J. Grunthaner to devise a low temperature Si surface cleaning for MBE [116]. We therefore opted for this cleaning procedure.

The low temperature clean of the Grunthaner's involves three steps: 1) growth of a chemical oxide, 2) spin etch with a solution of HF in alcohol under N_2, and 3) desorption of the remaining contaminants in UHV at low temperature. These steps are now described in more details, as they were performed in our experiments. Fig. 5.2 and 5.3 illustrate the different stages of the Si surface preparation, observed by XPS and RHEED, respectively.

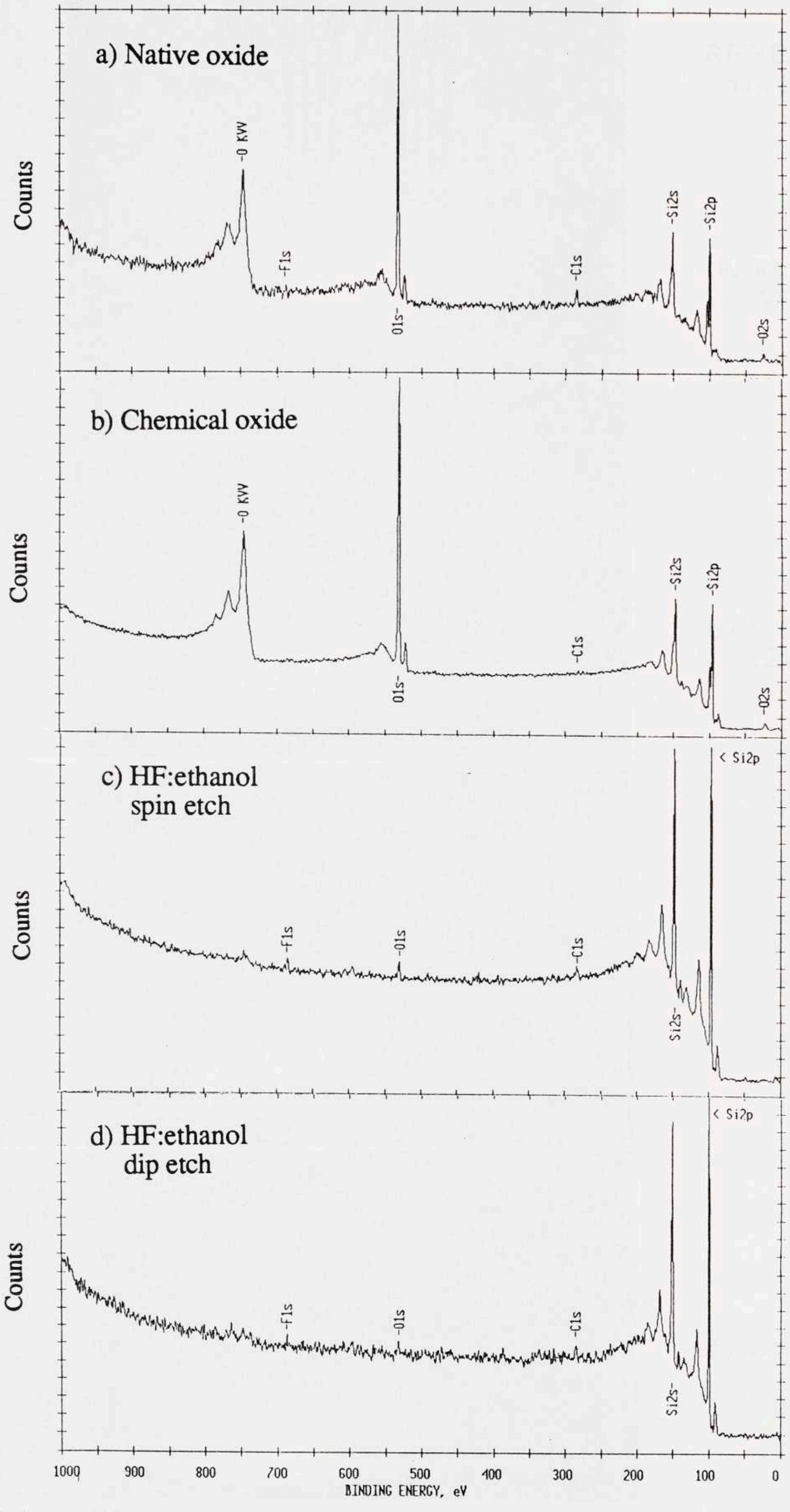

Figures 5.2. XPS survey spectra of the Si surface at different stages of the cleaning procedure

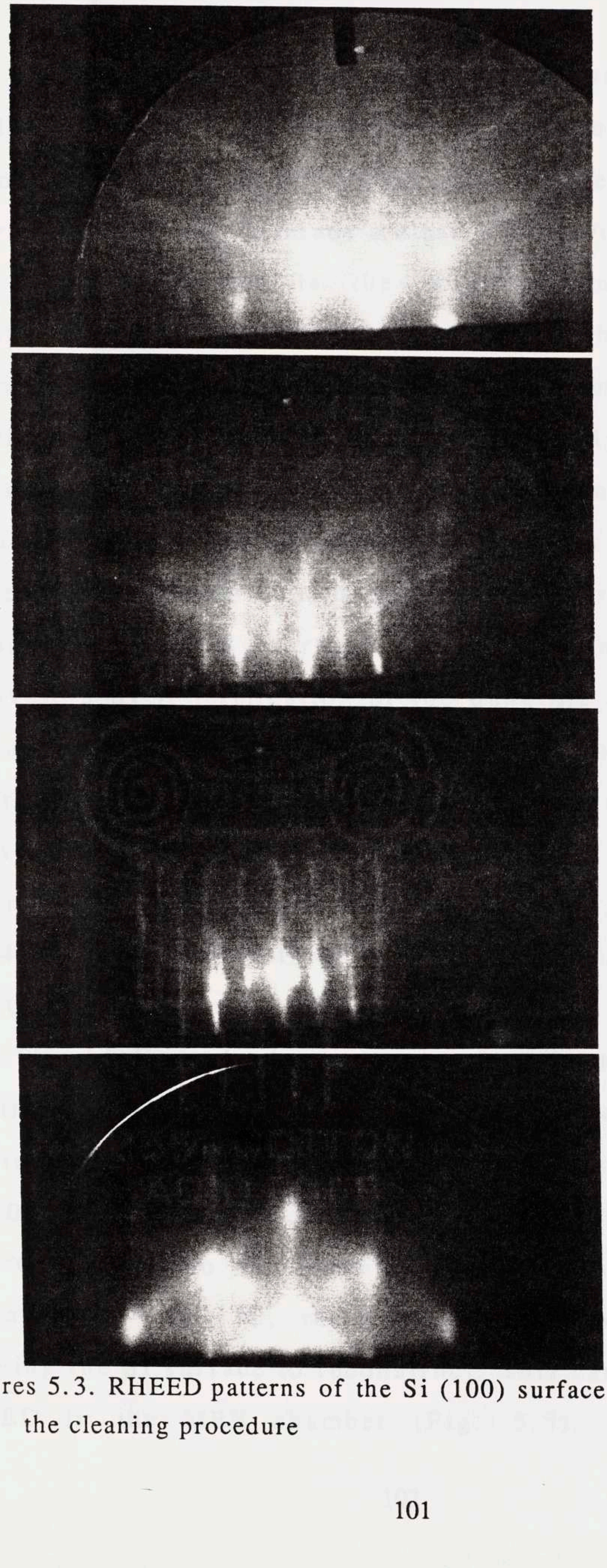
RHEED patterns of
Si (100) surface

a) as loaded
(1x1)

b) at 550 ℃
(2x1)

c) at 500 ℃
after MBE growth
(2x1)

d) Contaminated surface
at 600 ℃
(spotty 1x1 (SiC))

Figures 5.3. RHEED patterns of the Si (100) surface at different stages of the cleaning procedure

The first step is used to produce a carbon-free chemical Si dioxide, similarly to the first part of the Shiraki clean. It can be accomplished by several recipes, generally equivalent to each other as long as they produce a clean SiO_2 layer (Fig. 5.2b).

The second step is the original contribution of the Grunthaner's. The Si wafer capped with the clean chemical oxide is placed on a spinner in a glove box maintained under a positive pressure of N_2 (typically 50 mm H_2O). The SiO_2 is then etched by dropping droplets of a solution of HF in ethanol on the spinning wafer. The use of a solution of HF in ethanol (rather than in water) and the positive pressure of N_2 avoid the reoxidation of the Si surface and provide an almost complete passivation by H termination of the dangling bonds. The wafer is then mounted on the MBE holder and transferred to UHV under N_2 at all time. The level of contaminants (O, C, F) after the spin etch is only a small fraction of a monolayer as determined by XPS (in the case of Fig. 5.2c, 0.031 ML of O, 0.054 ML of C, 0.014 ML of F, where a monolayer (ML) on the Si (100) surface is 6.8×10^{14} atoms/cm^2)

The third step is the desorption in UHV at low temperature of the remaining contaminants. These contaminants are physisorbed and will desorb by maintaining the wafer at 175 °C for 30 min typically. The temperature can then be raised slowly (15 °C/min) up to the growth temperature (500 - 600 °C). Around 400 - 450 °C, the passivating H begins to desorb, allowing the Si surface to reconstruct. This can be monitored by RHEED in the MBE chamber (Fig. 5.3). The 1x1 pattern observed after loading of the wafer (Fig. 5.3a) gradually changes into a 2x1 reconstructed pattern around 430 - 450 °C (Fig. 5.3b), indicating that the surface is clean and ready for epitaxy. When the temperature is increased up to 600 °C, the reconstructed RHEED pattern sharpens further, showing that the surface gets smoother. After MBE growth, very sharp and clear 2x1 patterns indicate the good epitaxial quality of the Si and $Si_{1-x}Ge_x$ films (Fig. 5.3c). If the surface is not clean, the 2x1 reconstruction is not observed upon heating, but a 1x1 spotty pattern characteristic of SiC particulates appears instead (Fig. 5.3d). The Grunthaner's characterized further by Secondary Ion Mass Spectrometry (SIMS) and Scanning Tunneling Microscopy (STM) the cleanliness of the Si surface prepared by the spin etch method [115]. Using depth profiling by SIMS, the level of remaining contaminants at the original surface obtained by the spin etch clean is comparable to other cleaning procedures involving a high temperature step. Moreover, STM observation reveals that the smoothness of the cleaned Si surface is improved quite significantly by using the low temperature spin etch clean instead of a technique with a high temperature anneal.

In this spin etch cleaning method, the low temperature desorption step and subsequent slow heating of the wafer up to the growth temperature are particularly important. Indeed, if these steps are eliminated and the wafer is heated up too quickly, the remaining physisorbed contaminants will not be allowed to desorb, but will become chemisorbed, requiring a high temperature anneal (to 850 °C, if not higher) to remove them.

For the IBO experiments, we devised another low temperature cleaning procedure for the surface preparation, which was much shorter than the spin etch technique but almost as efficient. For IBO, a low temperature surface cleaning technique is as important as for MBE, since a thin layer is formed on the surface and excessive contaminant levels can alter the growth and/or the properties of the thin films. However, the permissible level of contamination is higher than in MBE, since the oxides are amorphous films. In addition, the IBO process provides a self-cleaning of the substrate by sputtering of the loosely bonded contaminants on the surface (as we observed by in situ XPS during IBO).

This shorter cleaning procedure consists of a 2 min methanol rinse, a 15 sec dip etch in HF:ethanol (HF:H_2O: anhydrous alcohol, 1:1:10), followed by a 1 min methanol rinse, dried with N_2 and loaded as quickly as possible in UHV (usually less than 5 min). The surface cleanliness obtained by this dip etch clean is only slightly reduced compared to the results of the spin etch method, and was found to be satisfactory for the IBO experiments (Fig. 5.2d). The low level of contaminants can be attributed to the following properties. The first methanol rinse removes most of the carboneous contaminant on the native oxide of the as-received wafer. The HF:ethanol dip avoids the reoxidation of Si by the water contained in an HF:H_2O solution, conventionally used. It also provides H passivation of the Si surface. In conventional HF:H_2O etch and deionized water rinse, a Langmuir-Blodgett

(LB) film of contaminants is deposited on the clean Si surface when the wafer is retrieved from the baths, because H_2O does not wet bare Si. In the dip etch clean developed here, however, the alcohols, ethanol in the etch solution and methanol in the post-dip rinse, wet the clean Si surface, avoiding a LB film to be formed on the Si surface. When dried with N_2, the high grade methanol leaves a minimal amount of residue on the surface. The H passivation then protects the Si surface against reoxidation until it is loaded in UHV.

Moreover, the contaminants left by the dip etch clean are physisorbed and present in amounts small enough to be desorbed during the low temperature anneal (175 °C, 30 min). The Si surface is then clean and exhibits the characteristic 2x1 pattern at 450 °C (in all respect similar to that of Fig. 5.3b).

The key point for a successful and reproducible low temperature cleaning procedure for Si epitaxy is thus to provide an H-passivated Si surface with a minimum amount of physisorbed contaminants. Our short dip etch clean performed with high grade alcohols and minimal exposure to oxidants (in air and cleaning solutions) fulfills that requirement and was successfully used to prepare the Si surface for MBE growth in this work. The epitaxial quality of the MBE layers was assessed by cross-sectional TEM. The original surface appears in the TEM pictures as a straight line with few or no features (Fig. 5.17), indicating that no significant amount of contaminants was left by the short clean. Occasionally, defects nucleate at the original surface. A Si buffer was always grown before the Si_{1-}

$_x$Ge$_x$ layers in order to provide a smooth and clean template for MBE growth of the strained layers and to avoid nucleation of defects at the starting surface.

The short dip etch clean was also used for the Ge samples with a 30 sec dip etch. Although most of the native oxide and the carbon contamination was removed, the oxygen coverage was significantly higher than in the case of Si, around 0.2 to 0.3 monolayer coverage. This can be explained by an H-passivation less efficient and/or less stable and a more rapid reoxidation of the Ge surface when exposed to atmosphere. The Si$_{1-x}$Ge$_x$ layers were grown by MBE and then directly transferred to the IBO/XPS chamber without breaking vacuum. The pressure was at all time below 10^{-9} Torr, avoiding (excessive) contamination or reoxidation of the surface.

b. PRELIMINARY PREPARATION FOR THE IBO EXPERIMENTS

The IBO experiments were performed in the XPS chamber so that the change in composition and chemical state could be monitored by XPS analysis. The ion source was a hot filament, electron impact ion gun (PE 04-300), which is normally used for depth profiling by sputtering. The gun is designed to produce ions with energies between 1 and 4 keV, and its performances, i.e. current density and beam definition, deteriorate rapidly below 1 keV. In order to produce the ions with energies in the range of interest for IBO (< 1 keV) and with significant beam current density, the XPS sample stage was modified and special sample holders with a floating ground were designed to work in an acceleration-deceleration mode. The ions were extracted with a higher energy and decelerated to the desired low energy by biasing the sample at 1 kV, which was the practical limit of the electrical feedthrough. The beam shape and current density could thereby be kept to reasonable characteristics (see appendix A.1). The sample holders with a floating ground were also designed to allow successive MBE and IBO without removing the sample from vacuum. Small cleaved pieces, 10x10 mm^2 and 20x20 mm^2, or plain 2" wafers could be used with the appropriate holder. Due to the design of the respective holders, MBE growth could be monitored by RHEED only with the 2" wafers but not with the cleaved pieces.

The XPS was also reconfigured by switching the position of the ion gun and of the X-ray source, so that the ion beam could have a normal incidence. Normal incidence of the ion beam is important in IBD to favor maximum incorporation of the ions and to minimize sputtering. This changes somewhat the parameters used in the quantification by XPS, but within the experimental errors (< 5 %) [117].

c. IBO EXPERIMENTAL AND CHARACTERIZATION PROCEDURES

For the study of Si IBO, 3" wafers of p-type Si (100) 10-20 Ω cm were cleaved into 20x20 mm^2 samples. The pieces were then cleaned using the HF in ethanol dip etch technique.

For IBO of elemental Ge, thick Ge films (≈ 1000 Å) were deposited on a Si (100) 3" wafer by MBE at 500 °C. These films were epitaxially ordered as assessed by RHEED and TEM, although they contained large stacking faults due to the lattice mismatch with the Si substrate. Samples were then cleaved and cleaned for separate IBO experiments.

Both cleaved pieces and 2" wafers were used for IBO of $Si_{1-x}Ge_x$. On the 2" wafers, a Si buffer was first grown at 600 °C, then the $Si_{1-x}Ge_x$ was deposited at 500 °C with a constant preset composition of 20 % Ge. The epitaxial quality of the films was also monitored in situ by RHEED. The temperatures were slightly higher with the cleaved pieces (650 °C for Si buffer, 550 °C for $Si_{1-x}Ge_x$ layers) and no RHEED monitoring was possible. The actual thickness and composition of the films were determined by cross-section TEM and RBS. After MBE growth, the samples were transferred to the IBO/XPS chamber without breaking vacuum in a base pressure $< 10^{-9}$ Torr at all times, avoiding any contamination of the $Si_{1-x}Ge_x$ surface.

IBO was performed at room temperature in a base pressure $<10^{-9}$ Torr. The deposition pressure was typically 5×10^{-8} - 10^{-7} Torr and never exceeded 2×10^{-7} Torr. $^{18}O_2^+$ instead of $^{16}O_2^+$ was used to be able to investigate the reactivity of the IBO films by measuring by RBS the possible incorporation of ^{16}O after exposure to atmosphere and to improve the detection of incorporated oxygen during depth profiling by SIMS. The $^{18}O_2^+$ ions were produced with the electron impact ion gun using the acceleration-decelaration scheme described above. The ion current density ranged from 0.5 to 2 $\mu A/cm^2$ depending on the ion energy. The beam had a normal incidence and was rastered over an area of about 2 cm^2. The ion energy was varied from

100 eV to 1 keV in order to study the dependence of phase formation and film properties upon ion energy. At regular time intervals, the IBO was interrupted and the sample grounded in order to characterize the growing film by *in situ* XPS. The samples were exposed to the ion beam until the O 1s signal reached a saturation level which occurred for doses between 1.5×10^{16} to 3×10^{16} O/cm^2 depending on the ion energy and the substrate. The ion doses were estimated by combining the Faraday cup characterization of the ion beam (see appendix A.1) and the measurements of the ion current during IBO and of the IBO spot area. Still a significant error with regard to the ion doses can be expected.

After IBO, the samples were characterized *in situ* by angular resolved XPS to profile the oxide composition in depth. The XPS apparatus was a Perkin-Elmer ESCA 5400, with a spherical capacitor analyzer 10-360, equipped with a small area Omni Focus lens and a single channel detector. The analyzer was operated in small area and Fixed Analyzer Transmission (FAT) modes, resulting in an energy resolution given by $\Delta E = 0.015$ PE, where PE is the pass energy for the acquisition. Typically, the pass energy was 89.45 eV for survey acquisition (full scans of binding energy (BE) from 1400 to 0 eV), 35.75 eV for multiplex acquisition of different peaks (Si 2p, Ge 3d, etc), and 71.55 eV for profile acquisition during IBO monitoring. The available X-ray radiations were Al Kα (hν: 1486.6 eV, FWHM: 0.85 eV) and Mg Kα (hν: 1253.6 eV, FWHM: 0.65 eV). The XPS was calibrated using Au 4f$_{7/2}$ (84.0

eV), Ag $3d_{5/2}$ (368.3 eV) and Cu $2p_{3/2}$ (932.7 eV) photoelectron peaks emitted from pieces of the corresponding metals mounted on the Faraday cup (FC) assembly. Calibration of the XPS, triple alignment of the X-ray beam, small analysis area and ion beam, and characterization of the ion beam could thus be performed efficiently and accurately by using the FC assembly.

Ex situ characterization included the following complementary techniques:

- SEM observation to assess the presence of an insulating film and the dimensions and shape of the reacted area. These were performed in a CAMSCAN Series 2 SEM operated in secondary electron imaging mode, with a 20 keV electron beam.

- ellipsometry to measure the film thickness. The ellispometer was a Gaertner L117 operated at an angle of 70 ° and with a He-Ne laser light (6328 Å).

- cross-section TEM to determine the film thickness and uniformity, the interface width, the microstructure and the presence of defects in the underlying substrate. The sample were prepared by successive mechanical thinning and polishing, dimpling, and lastly ion beam milling by Ar at 1 keV [1]. A TEM JEOL 200-CX operated at 200 keV, giving a spatial resolution of 4 Å was used to observe the samples.

- Rutherford Backscattering (RBS) combined with ion channeling techniques was used to quantify the ^{18}O incorporation and the number of displaced Si atoms and to detect the possible presence of ^{16}O and damage in the substrate. The RBS analysis was done with 2 MeV $^4He^+$ produced by a tandem accelerator. The FWHM was around 25 keV, corresponding to a depth resolution not better than 300 Å. The experimental setup illustrated in Fig. 5.4 is characterized by a fixed angle (10 °) between the incident He beam and the detector.

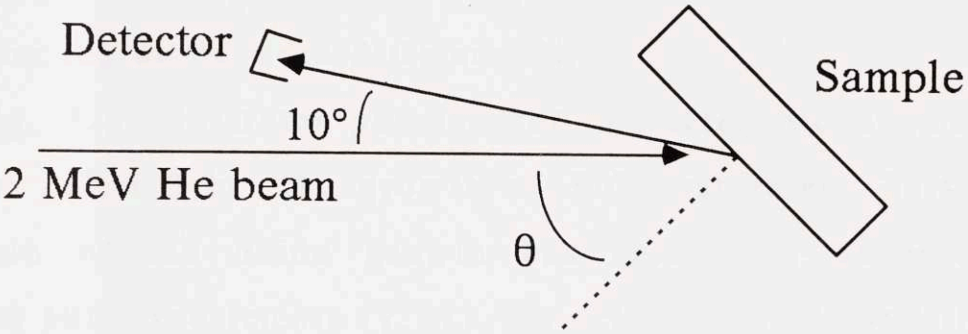

Figure 5.4. Geometry of the RBS system

The electrical characterization is the object of chapter 8.

d. RESULTS OF IBO OF SI, GE AND $SI_{1-X}GE_X$

1. IBO OF ELEMENTAL SI

In Fig. 5.5, time-resolved XPS spectra show the progressive oxidation of Si under $^{18}O_2^+$ bombardment at 100 eV as a function of time. As the exposure to the ion beam increases, the Si 2p signal of unreacted Si (Si^0, 99.6 eV) originating from the substrate decreases in intensity while a signal at higher binding energy (103.6 eV) appears and increases due to the formation of stoichiometric SiO_2 (Si^{4+}). In the initial stage of IBO, Si suboxides are formed as can be seen in the XPS spectrum. However, as the oxygen dose increases, these transitory suboxides disappear completely and only stoichiometric SiO_2 grows on top of the Si substrate. An estimation of the contribution of the suboxides in the IBO oxide can be made by curve fitting of the Si 2p signal, based on the data from Himpsel et al. [118] This is shown in Fig. 5.6 and Table 5.1 which lists the characteristics of each contributing peak. The contribution of the suboxides amounts to less than 7% of the total intensity of the Si 2p peaks and is indicative of the transition region between SiO_2 and Si.

Fig. 5.5 illustrates yet another characteristic of the IBO process: after 3 hr, the growth of SiO_2 saturates. This self-limitation of the oxide growth has also been observed in previous IBO experiments [7,27]. Its origin will be investigated in the theoretical modelling of IBO presented in chapter 6.

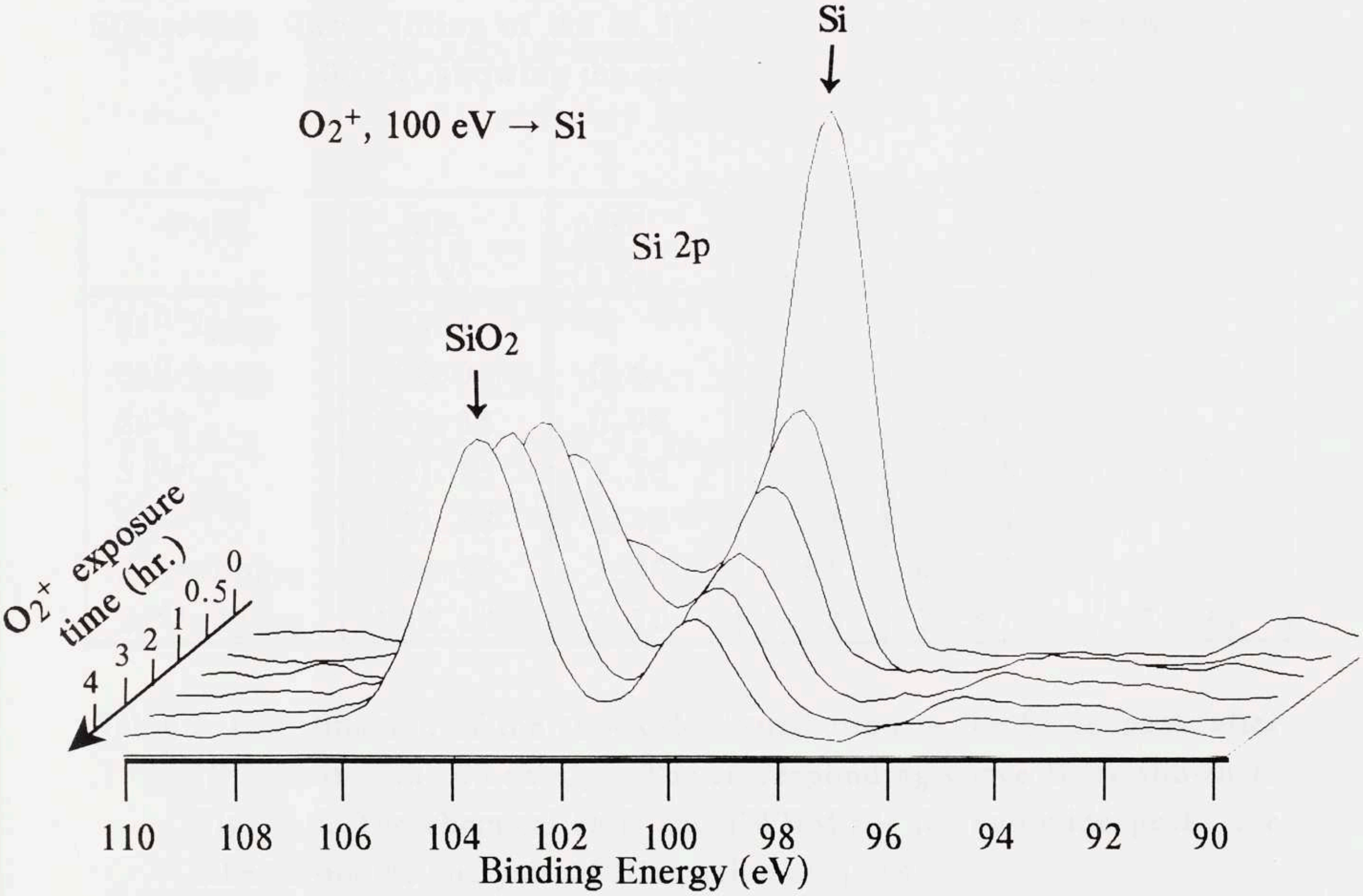

Figure 5.5. Time-resolved XPS spectra of the Ion Beam Oxidation of Si with 100 eV $^{18}O_2^+$ as a function of exposure time to the beam

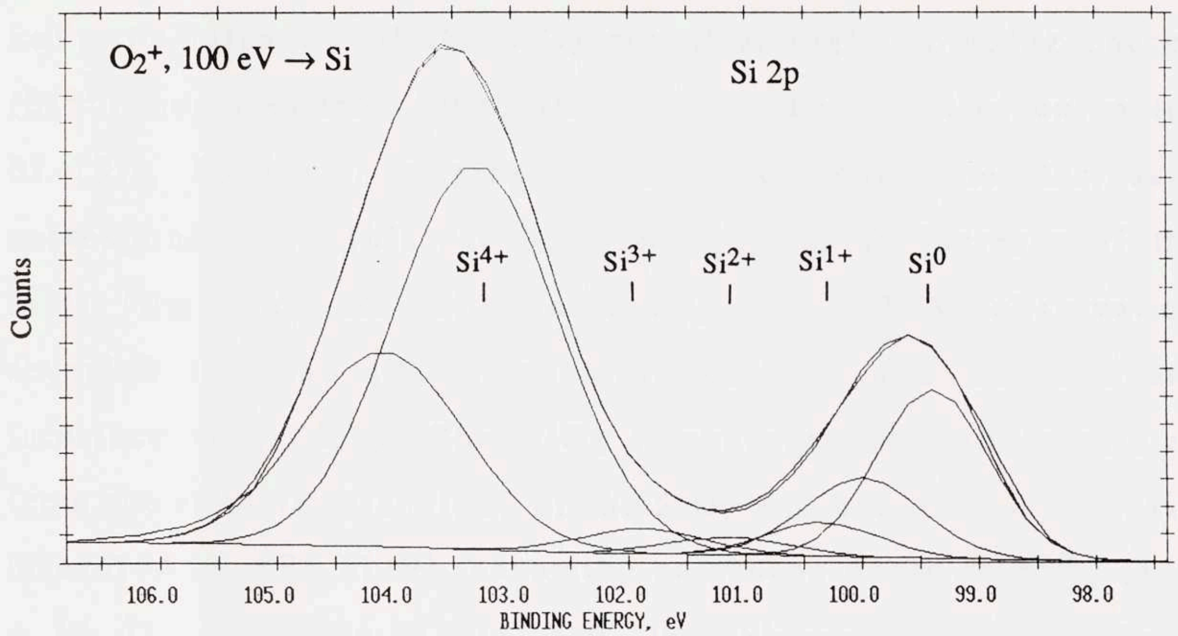

Figure 5.6. Curve fitting of the Si 2p peak from the oxide film formed by IBO at 100 eV, showing the contribution of the suboxides

Peak	BE (eV)	ΔBE (eV)	FWHM (eV)	Area %	
Si^0 $2p_{3/2}$	99.4		1.11	14.20	
Si^0 $2p_{1/2}$	100.0	0.6	1.19	7.10	21.30
Si^{1+}	100.35	0.95	1.13	2.86	
Si^{2+}	101.15	1.75	1.22	1.56	6.76
Si^{3+}	101.88	2.48	1.24	2.34	
Si^{4+} $2p_{3/2}$	103.30	3.90	1.65	47.97	
Si^{4+} $2p_{1/2}$	104.10	4.70	1.62	23.97	71.94

Table 5.1. Estimation of the suboxide contribution in the Si 2p peak after IBO of Si with 100 eV O_2^+. The corresponding curve fit is shown in Fig. 5.6. The chemical shift and FWHM for the suboxide peaks are taken from the analysis of Himpsel et al. [118]

Fig. 5.7 shows the Si 2p signal at saturation as a function of ion energy (E_{ion}). With E_{ion} increasing from 100 eV to 1 keV, the intensity of the SiO_2 signal at higher binding energy (Si^{4+}) increases from 70 to 90 %, while the signal of unreacted Si (Si^0, 99.6 eV) originating from the substrate decreases correspondingly. This can be interpreted as an increase of the SiO_2 film thickness with increasing E_{ion}. TEM observation revealed that the IBO films were uniform and had a sharp interface (Fig. 5.8). The SiO_2 thicknesses can be calculated from the relative intensities of the SiO_2 and unoxidized Si peaks measured by XPS [119], assuming an escape depth in SiO_2 (λ_{ox} = 30 Å). As shown in Fig. 5.9, the thicknesses derived from XPS are in excellent agreement with those measured by cross-section TEM and ellipsometry assuming an index of refraction of 1.46.

As it can also be seen in Fig. 5.7, the SiO_2 peak shifts slightly to a lower binding energy as the thickness decreases (Table 5.2): from 104.2 eV for the 70 Å film to 103.6 eV for the 39 Å oxide. This shift is characteristic of thin oxide films and has been observed by other workers. According to the thorough analysis of the Grunthaner's [120] on thin thermal oxides, this is due to a change of the atomic density and bridging bond angle distribution in the SiO_2/Si interfacial region, resulting in a change in the valence charge distribution in the Si-O bond and the observed chemical shift difference. From this observation, the SiO_2 interfaces formed by IBO are similar to those formed by thermal oxidation. This has already

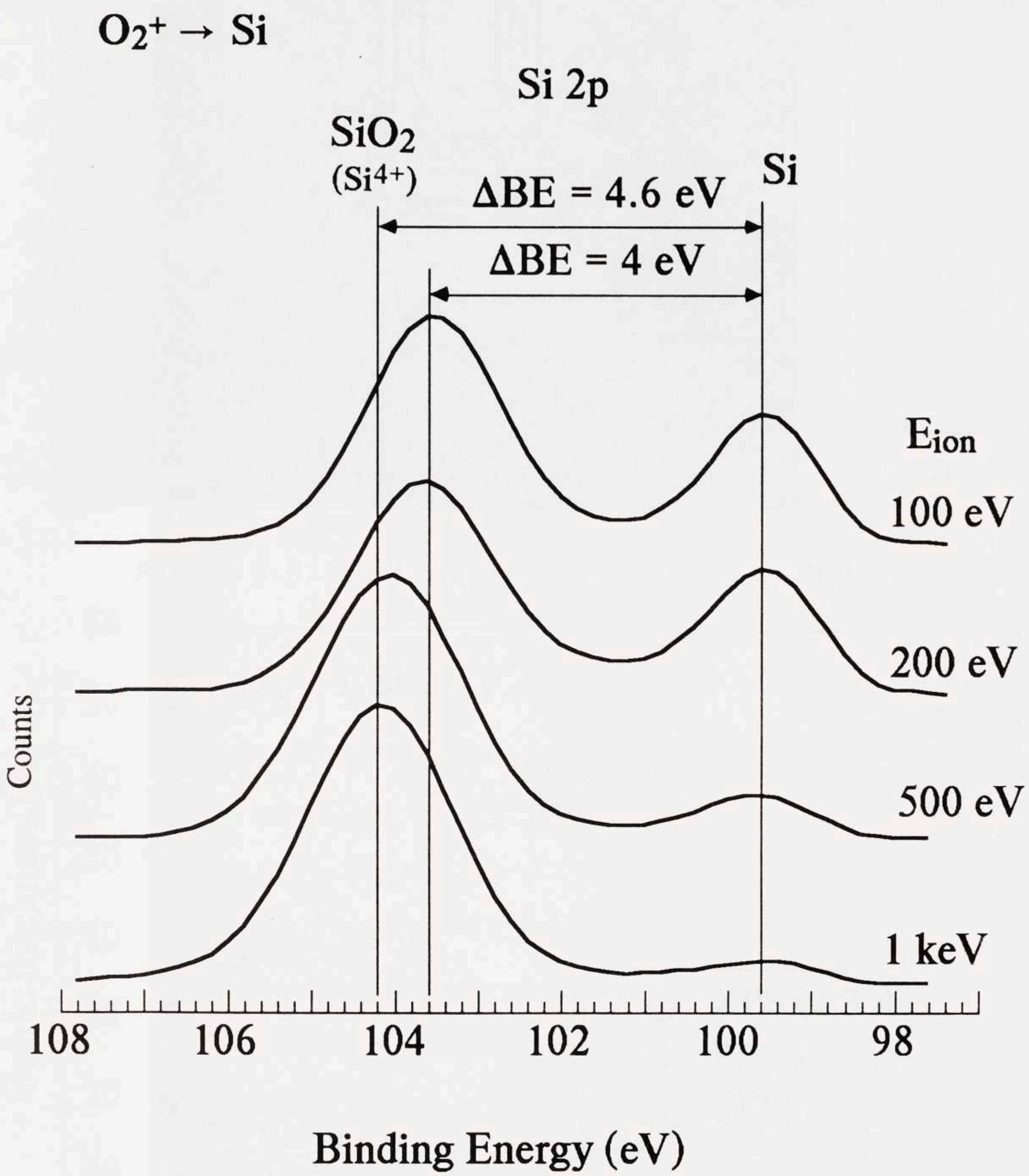

Figure 5.7. XPS spectra of the Si 2p signal as a function of ion energy in IBO of elemental Si

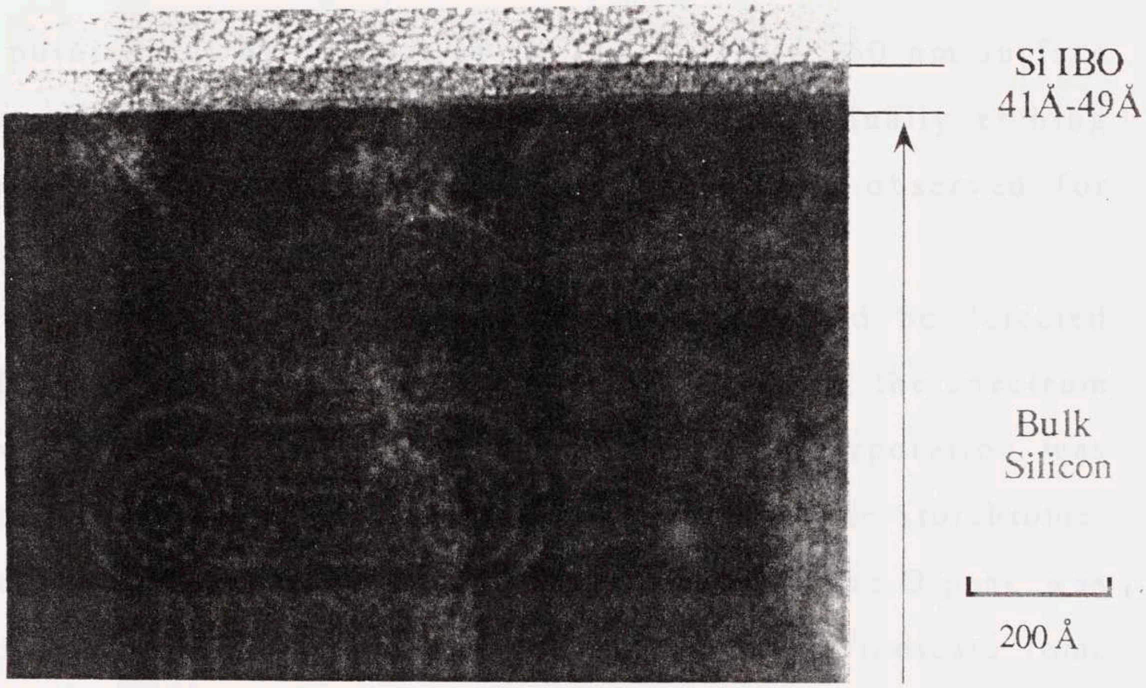

Figure 5.8. TEM picture of IBO SiO_2 at 200 eV

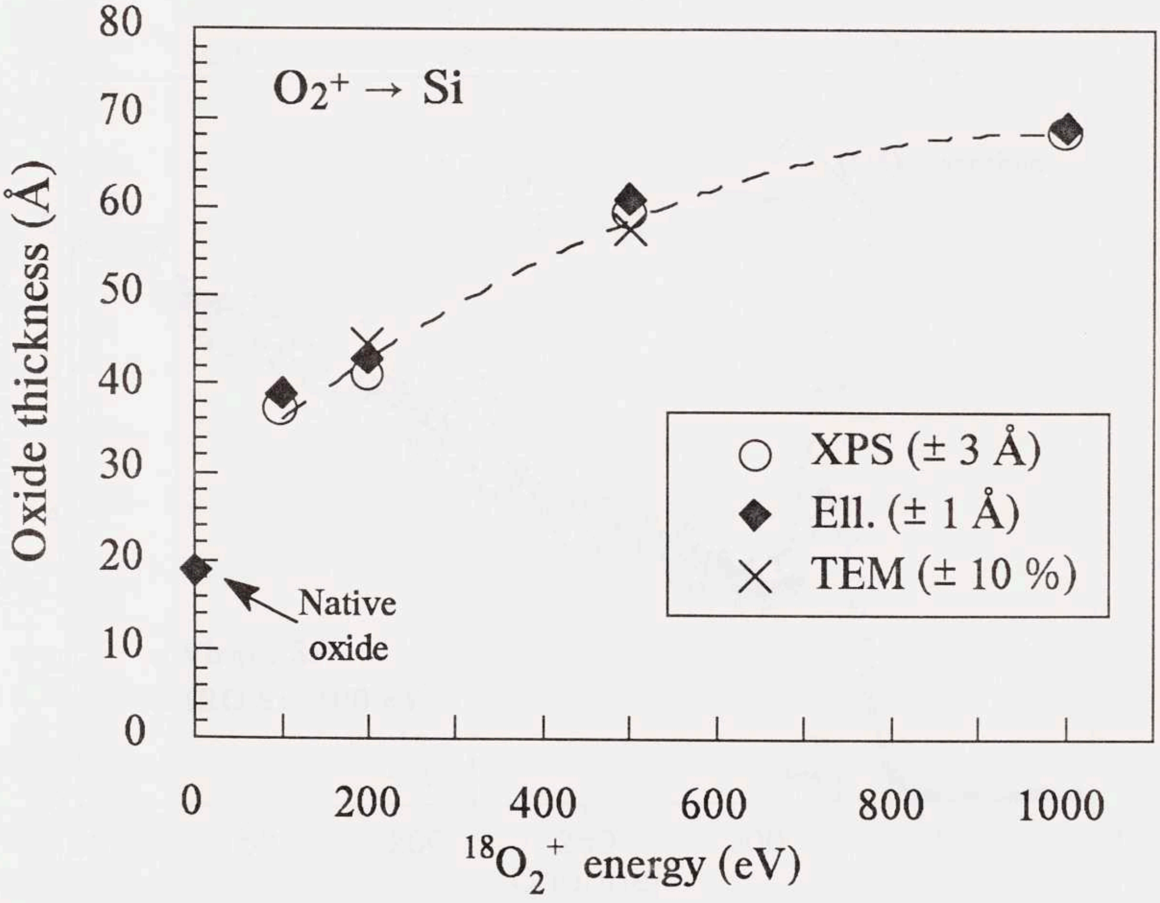

Figure 5.9. Thickness of the IBO SiO_2 films as a function of ion energy, as measured by XPS, ellipsometry and TEM

been pointed out by Schulze et al. [121] with a 160 nm surface oxide grown using $^{16}O^+$ ions at 30 keV. By gradually etching the oxide, a decrease in the chemical shift was observed for oxide thicknesses below 40 Å.

No damage in the underlying substrate could be detected by TEM and RBS (Fig. 5.8 & 5.10). By acquiring the spectrum in the <110> channeling direction, the ^{18}O incorporation was measured with a minimum of background noise. The stoichiometry determined from the RBS Si surface peak and the O peak was found to be below the ideal ratio of 2. This might indicate some displaced Si under the SiO_2 films, although such a region could

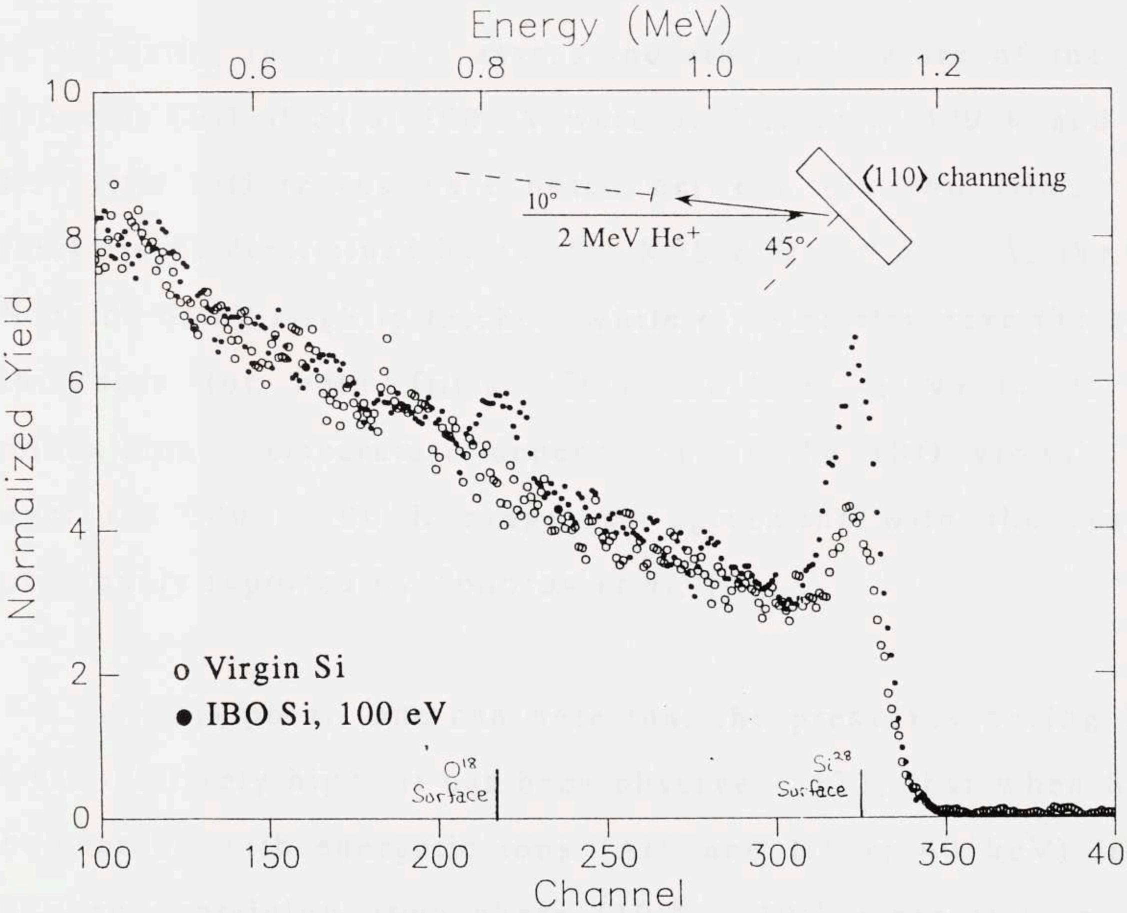

Figure 5.10. RBS spectra in the <110> channeling direction of virgin Si and Si with 100 eV IBO SiO_2

not be identified in the TEM micrographs. ^{16}O was not consistently detected. We do not have a definitive interpretation for its incorporation in some samples and its absence in others. Two possible explanations are the following. (1) Some Si may be left unreacted at the surface of the IBO SiO_2 films and oxidizes upon exposure to atmosphere. (2) During the RBS analysis, some ^{16}O from the background gas in the vacuum chamber (10^{-6} - 10^{-7} Torr) is incorporated in the IBO films by Ion Beam Induced Oxidation [122] and replaces the ^{18}O. Depth profiling by SIMS analysis performed in UHV ($< 10^{-9}$ Torr) should allow us to determine the ^{16}O origin.

Lastly, in order to assess the athermal nature of the IBO process, IBO of Si at 200 eV were performed at 300 K and 700 K. Little differences were noted between the two films. The thicknesses determined by in situ XPS differed by 2 Å, the 700 K oxide being slightly thicker, while ellipsometry gave the same thickness for both films. This indicates a weak, if not nonexistent, temperature dependence of the IBO growth rate over the 300 - 700 K range, in agreement with the results previously reported by Todorov et al. [24]

At this point, one can note that the pressures during IBO were relatively high. It has been observed [122] that when Si is bombarded with energetic ions (Ar^+ and N^+ at 40 keV) in an oxygen containing atmosphere (10^{-8} - 10^{-5} mbar O_2), a thin SiO_2 film can be formed by Ion Beam Induced Oxidation (IBIO).

The SiO_2 film thickness formed by IBIO saturates after a rapid growth. The saturation thickness strongly depends on O_2 partial pressure (0 Å at 10^{-8} mbar, 10 Å at 10^{-7}, 40 Å at 10^{-6} and 100 Å at 10^{-5}) but not so much on the ion beam current density, species or energy (in the medium keV range). With our working pressures (typically 9×10^{-8} Torr = 6.75×10^{-8} mbar), there might be a slight contribution from the background oxygen to the oxide film formation, but IBIO is probably not the predominant phenomenon observed in our experiments. The following remarks can be stated to support further this conclusion. The IBO study was performed with much lower energies than in ref. [122]. These low energies can be expected to favor direct oxidation by incorporation of oxygen ions versus recoil implantation of the background oxygens. The evolution with time of the oxide formation at different energies, i.e. slower initial oxidation rate at higher energies, is indicative of a subsurface process (IBO) rather than a surface-driven process (IBIO). The strong dependence of the film thickness observed upon ion energy while the O_2 partial pressures were similar, also demonstrates that Si oxidation as investigated here is governed by direct Ion Beam Oxidation. Lastly, the results of the present experiments, namely the SiO_2 film thicknesses, can be compared to those of other IBO experiments done in true UHV conditions (< 10^{-9} Torr), either at the same low energy (200 eV O^+) [7] or at slightly higher energy (4 keV O_2^+) [123].

2. IBO OF ELEMENTAL GE

Fig. 5.11 illustrates the gradual oxidation of Ge (29.7 eV) into GeO_2 (33 eV) under $^{18}O_2^+$ bombardment at 200 eV. Features are similar to those observed in Si IBO. IBO of Ge first goes through a short initial stage where Ge suboxides are formed, then the formation of stoichiometric GeO_2 increases and finally saturates.

In the case of elemental Ge oxidized by IBO (Fig. 5.12), a dramatic dependence of phase formation on the ion energy is observed. Below 200 eV, GeO_2 is clearly formed, while at 500 eV and above, the chemical shift of the oxidized peak does not

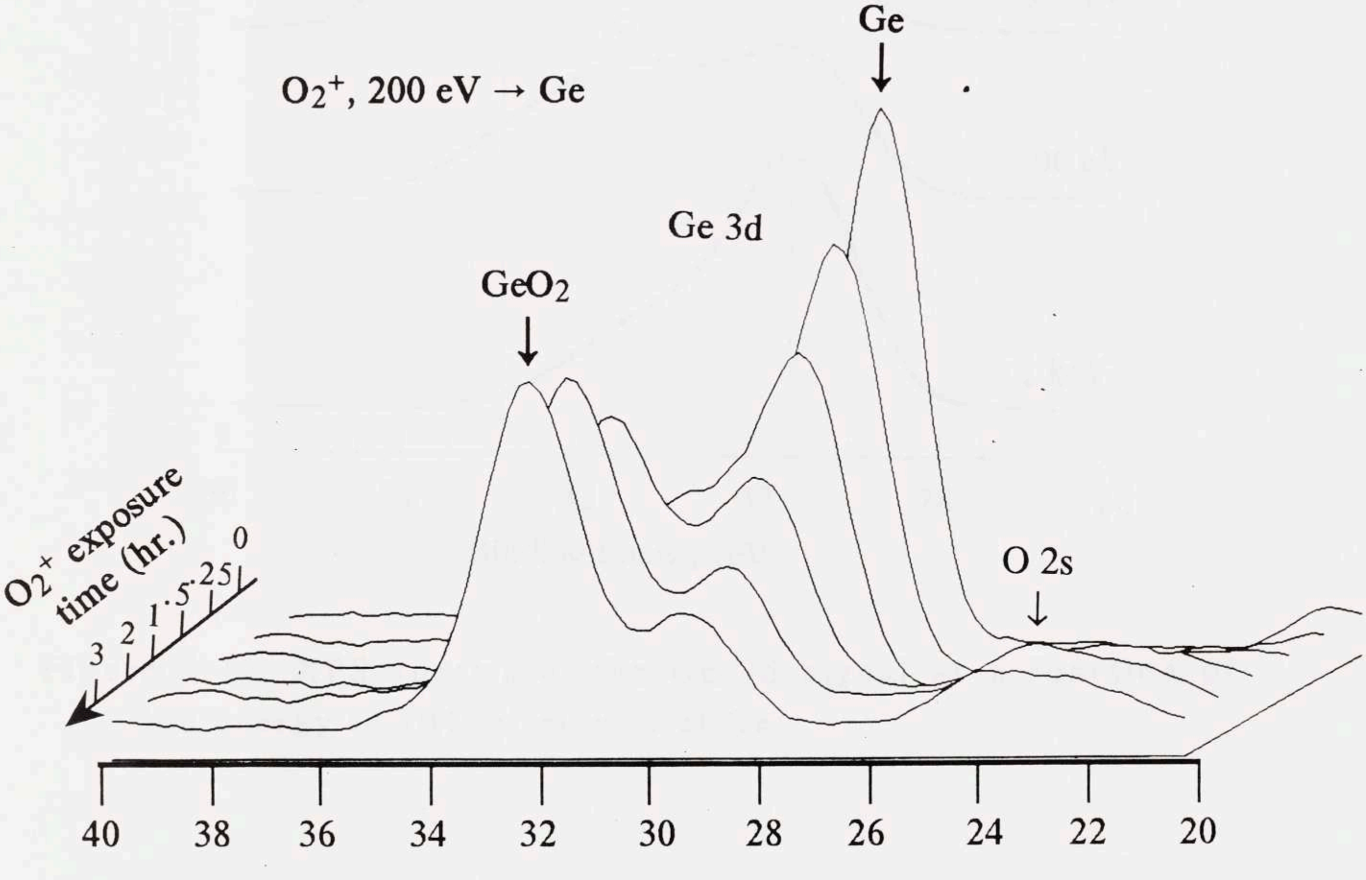

Figure 5.11. Time-resolved XPS spectra of the Ion Beam Oxidation of Ge with 200 eV $^{18}O_2^+$ as a function of exposure time to the beam

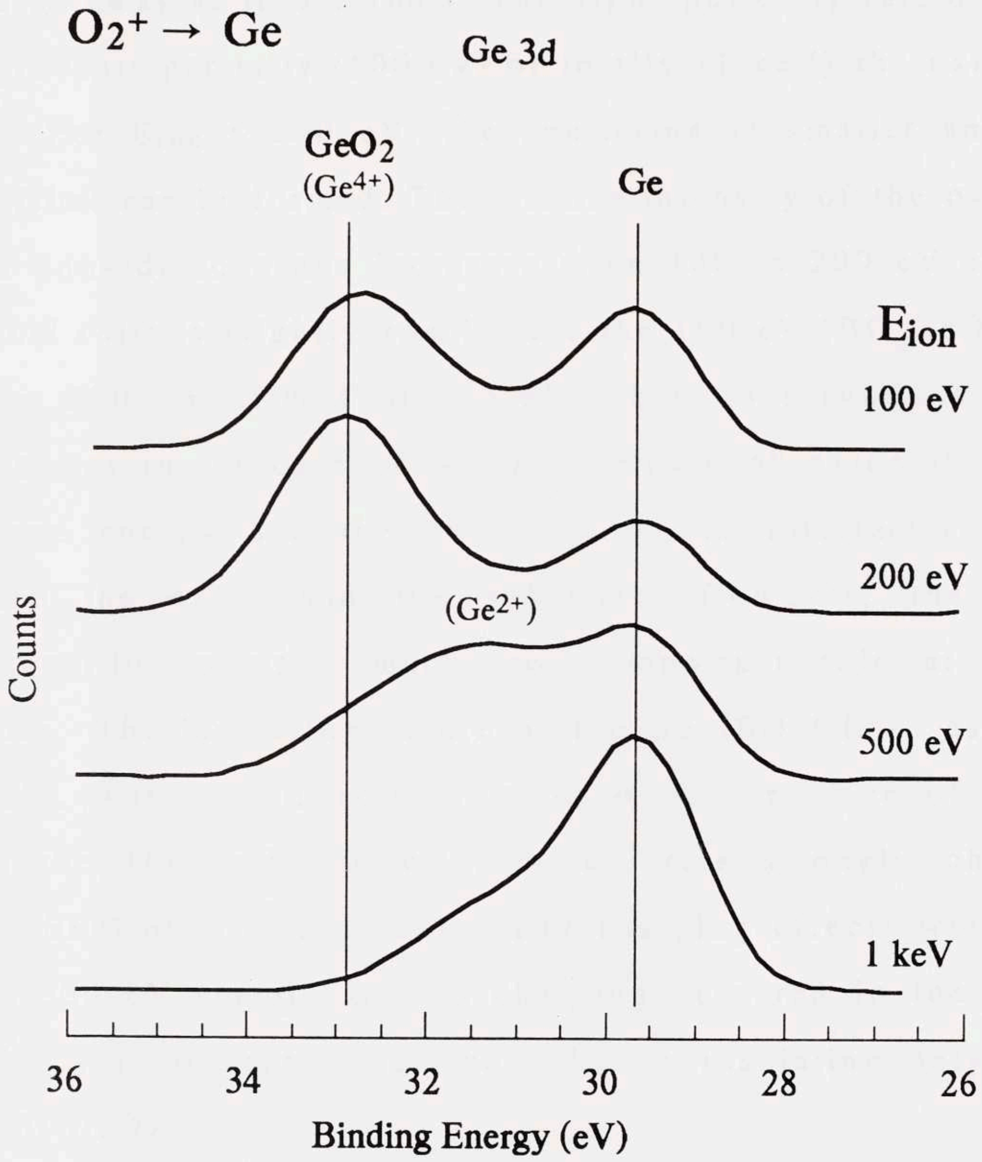

Figure 5.12. XPS spectra of the Ge 3d signal as a function of ion energy in IBO of elemental Ge

correspond to GeO_2 (Ge^{4+}), but to the lower oxide GeO (Ge^{2+}). GeO_2 is a volatile oxide and at higher ion energies, is probably sputtered away as it is formed. The high sputtering rate of GeO_2 thus prevents partially (500 eV) or totally (1 keV) the oxidation of Ge. For $E_{ion} \leq 200$ eV, the sputtering is smaller and thin GeO_2 films can be formed. The relative intensity of the oxidized to the unoxidized peaks increases from 100 to 200 eV and the chemical shift is slightly smaller for the 100 eV IBO GeO_2 than for the 200 eV film (Table 5.2). These observations might indicate, as in the case of Si, an increase of oxide thickness with ion energy and the existence of an interfacial region between the oxide and the substrate. However, the phase decomposition plays a much more important role at higher energies. The insulating nature of the Ge IBO films, assessed by SEM, was also directly related to the presence of GeO_2. While the 100 and 200 eV samples were strongly charging during SEM observation, only faint charging effects were seen in the 500 eV sample and no charging occurred in the 1 keV sample. This indicates that the oxide is insulating only when made of GeO_2.

TEM observations indicated that the epitaxial quality of the Ge films was relatively good, although some large stacking faults were present (Fig. 5.13). The surface, however, was very rough and made difficult the detection of an amorphous layer on top of the Ge films. It should be noted that the TEM sample preparation might have affected the film microstructure. Amorphous GeO_2 is indeed highly soluble in water which is used in the dimpling of the samples. Strong ion beam milling effects can also be detected and seems to indicate that Ge films are quite sensitive to the TEM sample preparation method.

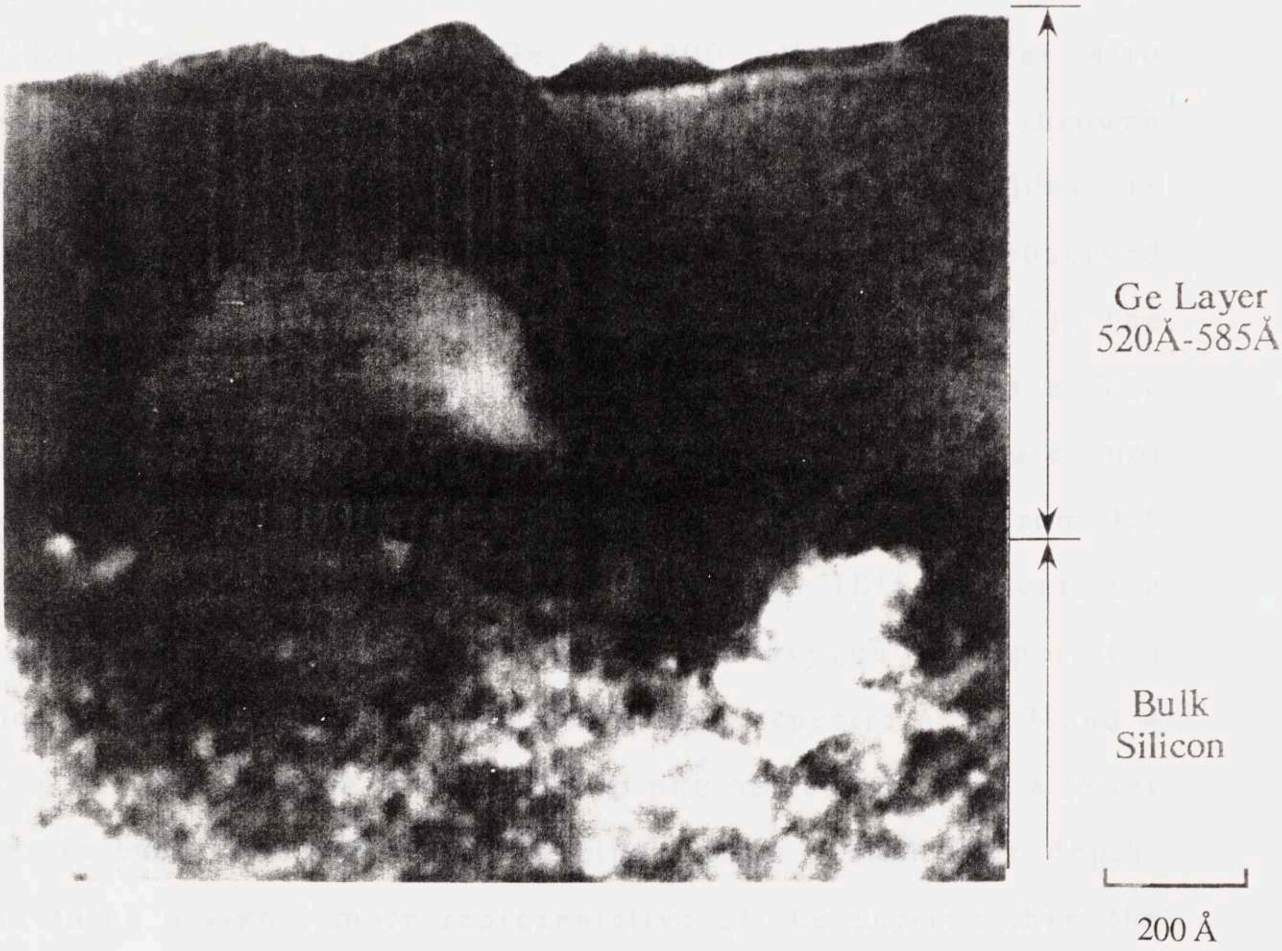

Figure 5.13. TEM picture of IBO Ge at 200 eV

3. IBO OF $SI_{1-X}GE_X$

During IBO of $Si_{1-x}Ge_x$ layers under $^{18}O_2^+$ bombardment, both the Si and the Ge of the alloy are transformed simultaneously into a fully oxidized state similar to that of stoichiometric SiO_2 and GeO_2, respectively. This is in contrast with observations for high energy Ion Beam Synthesis of $Si_{0.5}Ge_{0.5}$ oxides where the Ge oxidizes only after the Si is completely oxidized [124]. Fig. 5.14 illustrates the gradual oxidation by IBO of $Si_{1-x}Ge_x$ at 200 eV. As it was also observed in IBO of elemental Si and Ge, the IBO goes through three stages: in an initial stage, substoichiometric oxides are formed significantly as evidenced by the chemical shift observed in the XPS spectra (at 0.5 hr of O_2 exposure in Fig. 5.14). The second stage consists of rapid growth of the dioxide phase. The transitory suboxides disappear progressively and are not contributing significantly (< 5 %) to the XPS spectra (from 0.5 to 2 hr of oxygen exposure in Fig. 5.14). The IBO then enters a third stage of saturation where the net oxygen incorporation does not increase anymore over time (XPS spectra at 2, 3 and 4 hr in Fig 5.14). Note that the Ge 2p photoelectrons have a lower kinetic energy and therefore originate from a shallower depth, providing a signal more representative of the surface than the Ge 3d photoelectrons. This explains why in the Ge 2p signal, the peak due to unoxidized Ge disappears almost entirely.

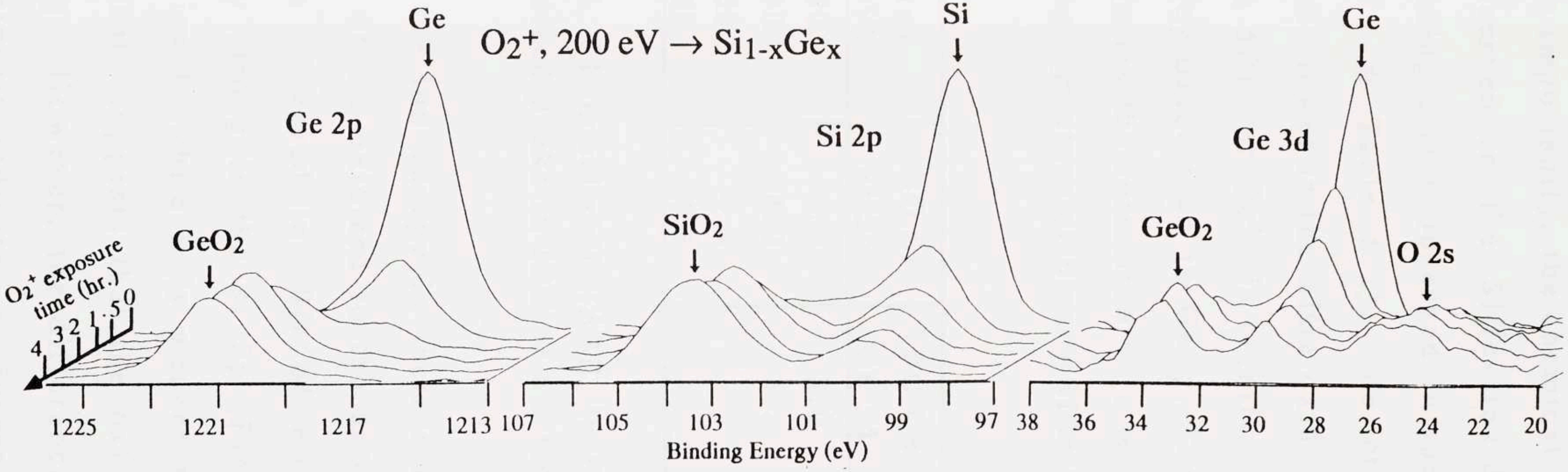

Figure 5.14. Time-resolved XPS spectra of the Ion Beam Oxidation of $Si_{1-x}Ge_x$ with 200 eV $^{18}O_2^+$ as a function of exposure time to the beam

More importantly, the chemical shift for the Si^{4+} and Ge^{4+} states observed in the SiGe-dioxide are different from the corresponding states observed in the elemental SiO_2 and GeO_2 (Fig. 5.15 & Table 5.2). The chemical shift for Si^{4+} is consistently lower in the SiGe-oxide than in SiO_2 by 0.1 to 0.4 eV, while ΔBE for Ge^{4+} is significantly larger by 0.8 - 1.0 eV in the alloy oxide than in GeO_2. These differences in chemical shift indicates the formation of a ternary phase of SiGe-dioxide rather than a mixture of binary SiO_2 and GeO_2 phases.

E_{ion}	IBO Si	IBO Ge	IBO $Si_{1-x}Ge_x$	
(eV)	Si 2p	Ge 3d	Si 2p	Ge 3d
100	4.0	3.0	3.8	4.0
200	4.0	3.2	3.9	4.0
500	4.4	-	4.0	4.2
1000	4.6	-	4.2	4.6

Table 5.2. Chemical shift (ΔBE, in eV) observed by XPS for the oxidized peaks in IBO of Si, Ge, and $Si_{1-x}Ge_x$.

As the ion energy is increased (Fig. 5.15), the relative intensity of the oxidized to the unoxidized peaks increases, as has been observed in IBO of elemental Si. This effect is relatively strong in the Si 2p (Fig. 5.15b) and Ge 2p (Fig. 5.15a) signals while it is weaker for the Ge 3d signal (Fig. 5.15c). This suggests that the oxide thickness increases with ion energy. However, the difference in intensity of the Ge 2p and 3d signals indicates an increasing non-uniformity of the

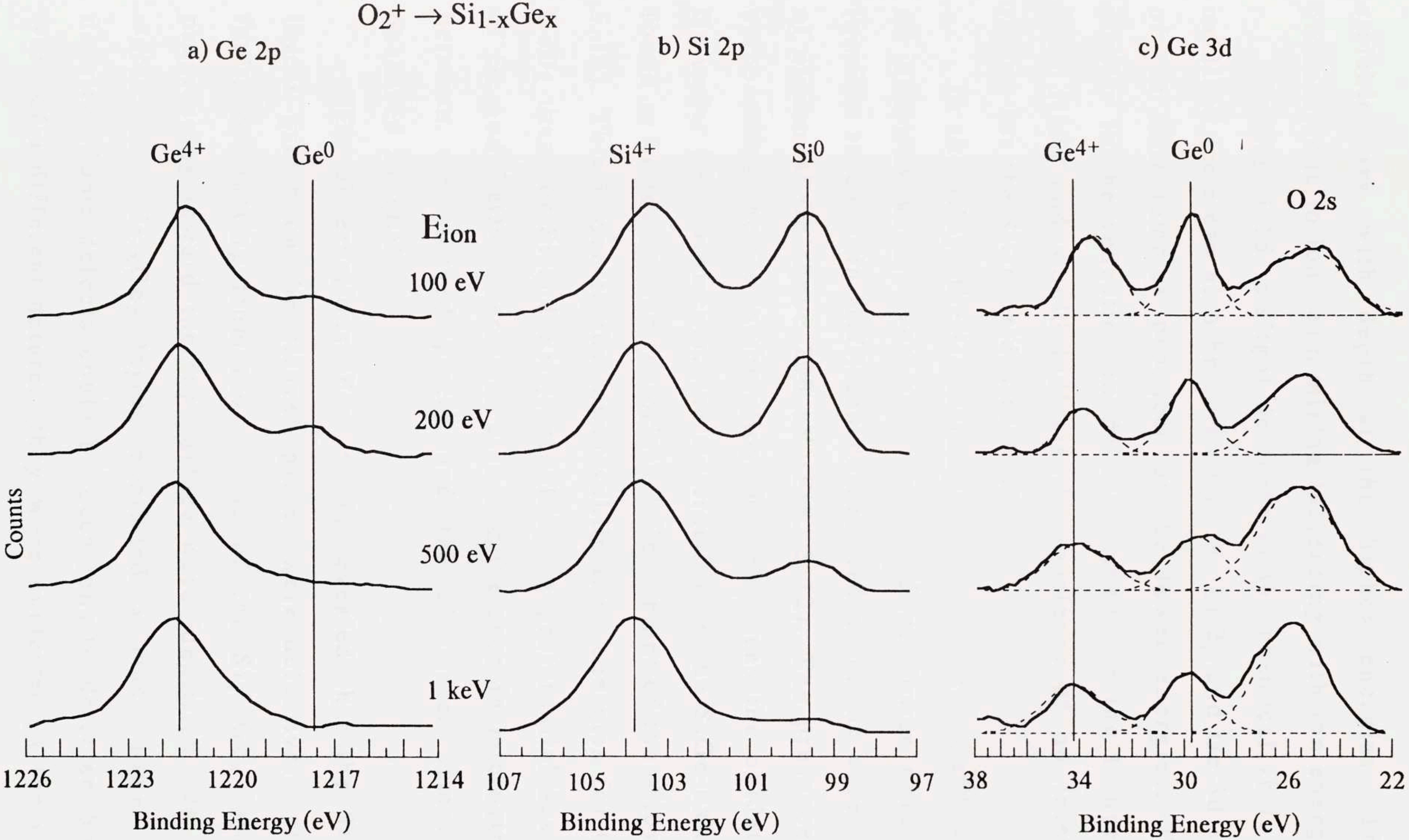

Figure 5.15. XPS spectra of a) Ge 2p, b) Si 2p, and c) Ge 3d signals as a function of ion energy in IBO of $Si_{1-x}Ge_x$. In (c), the gaussian fits (dotted lines) to the Ge^{4+}, Ge^0 and O2s peaks have been included to resolve the individual contribution of each signal.

stoichiometry with depth at the higher energies. This is probably due to ion beam mixing increasing with ion energy.

In Fig. 5.15, a slight decrease in the chemical shift of the oxidized state can also be noticed in the Si 2p and Ge 3d signals of the IBO samples produced at the lower energies. This is similar to the reduction in ΔBE observed for the thinner IBO SiO_2 films and would indicate the existence of an interfacial region for the SiGe-oxides as well.

In the alloy, the Ge is fully oxidized in the Ge^{4+} state at all energies used, even at 1 keV, and no lower oxide state (similar to Ge^{2+} in GeO) can be detected as in the case of IBO of elemental Ge above 200 eV (Fig. 5.12). The presence of Si surrounding the Ge in the alloy thus enhances the oxidation of Ge under IBO. However, the Ge fraction in the SiGe-oxide was found to be lower than the original Ge content of the alloy (Fig. 5.16). This is due to the lower sublimation energies for Ge and GeO_2 than for Si and SiO_2, resulting in preferential sputtering of Ge and GeO_2. There was also a difference in microstructure between the cleaved pieces and the 2” wafer samples, as observed by TEM.

TEM observations (Fig. 5.17) revealed that the $Si_{1-x}Ge_x$ layers grown on the cleaved pieces were defective: stacking faults originating from the middle of the $Si_{1-x}Ge_x$ layer and progressing toward the top surface were identified. On the 2” wafer, the $Si_{1-x}Ge_x$ layers exhibited a much lower defect density. Some defects could be occasionally detected but they were of a different nature: they were nucleated at the original

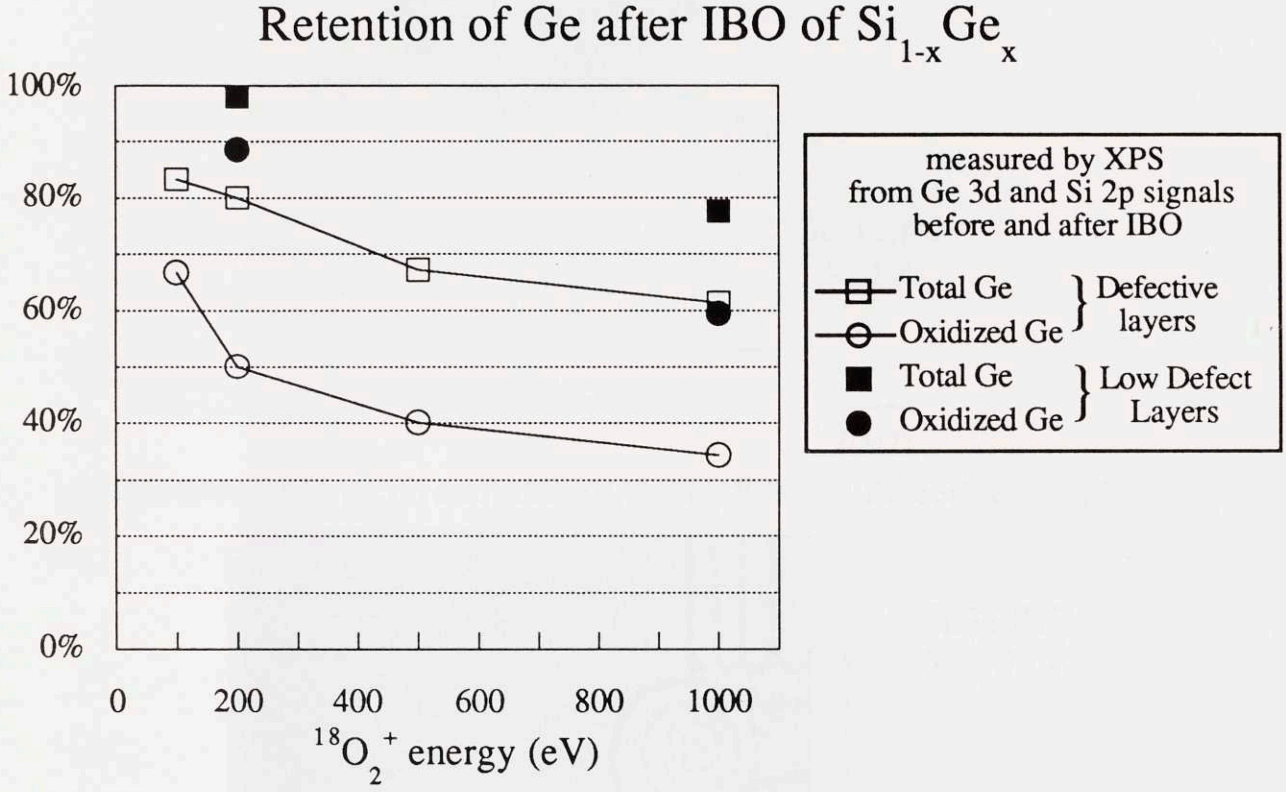

Figure 5.16. Retention of Ge after IBO as a function of ion energy. The Ge/Si ratio is calculated from the Ge 3d and Si 2p photoelectron peaks measured by XPS before IBO in the SiGe layer and after IBO in the SiGe-dioxide using the oxidized peak intensities of Si and Ge (annotated "oxidized Ge") and in the structure using the total intensity for both elements (annotated "total Ge"). The Ge retention is much higher in the films with a low defect density than in the defective $Si_{1-x}Ge_x$ layers

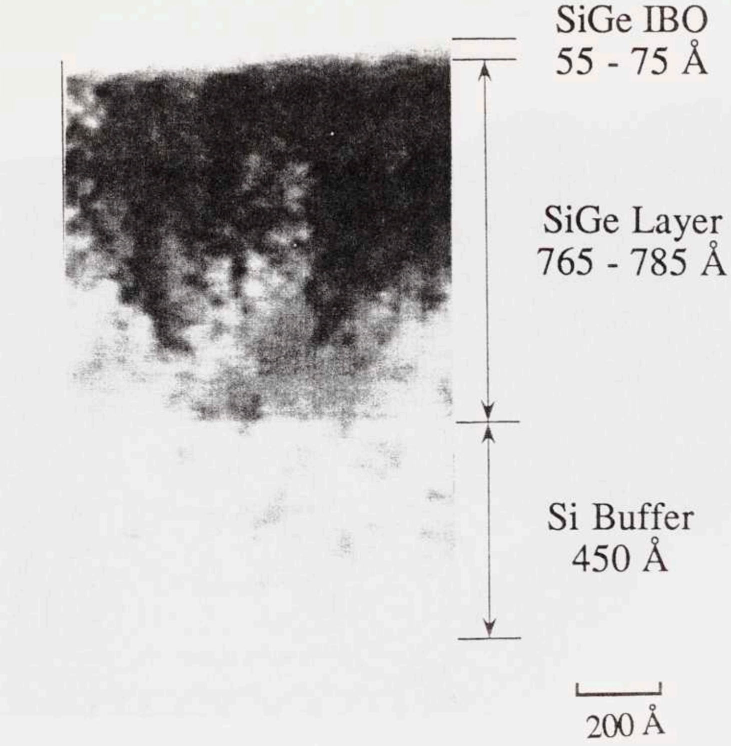

a) Off-axis TEM picture of 200 eV SiGe-IBO of a defective $Si_{1-x}Ge_x$ layer

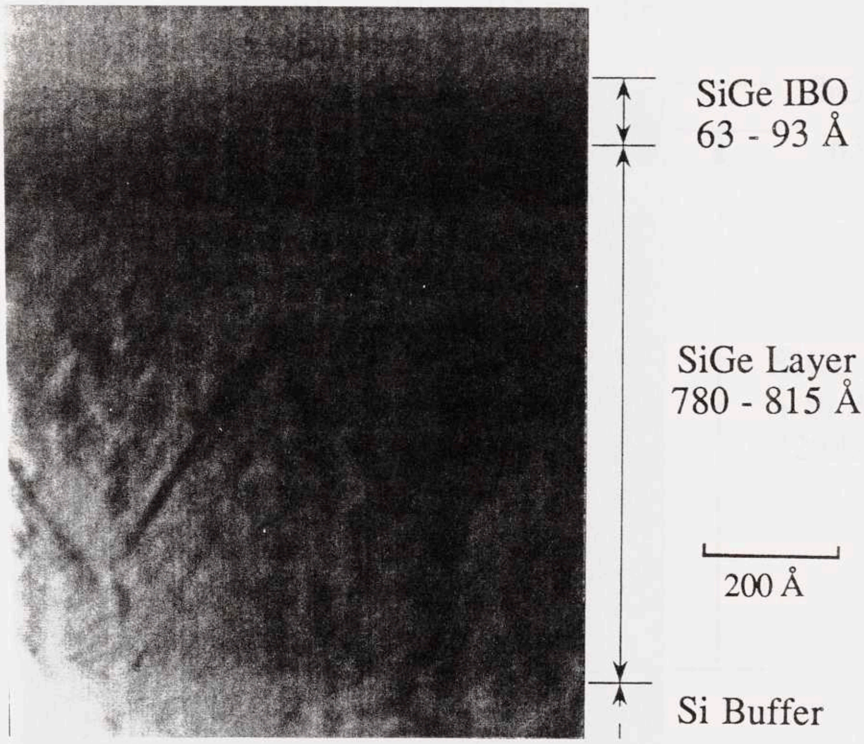

b) Off-axis TEM picture of 1 keV SiGe-IBO of a defective $Si_{1-x}Ge_x$ layer

Figures 5.17. Cross-section TEM micrographs of the IBO SiGe-dioxide/$Si_{1-x}Ge_x$ layer structures.

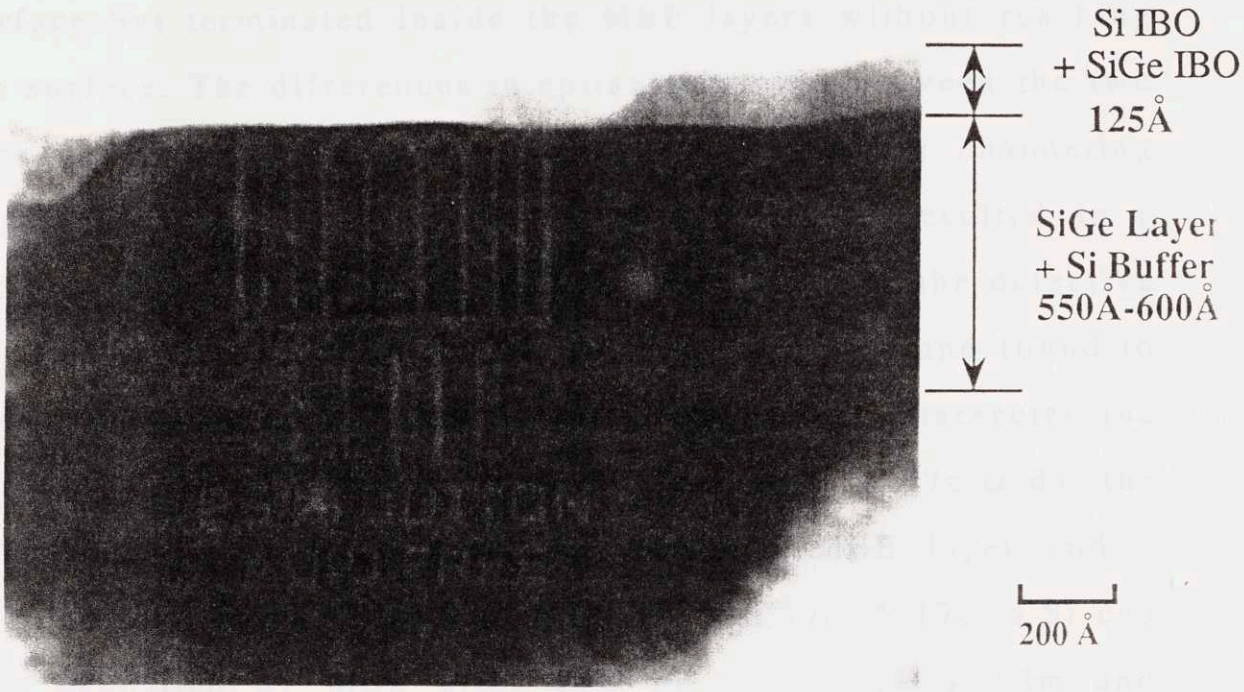

c) Off-axis TEM picture of 200 eV SiGe-IBO of a low defect density $Si_{1-x}Ge_x$ layer, capped with an IBO SiO_2 at 1 keV

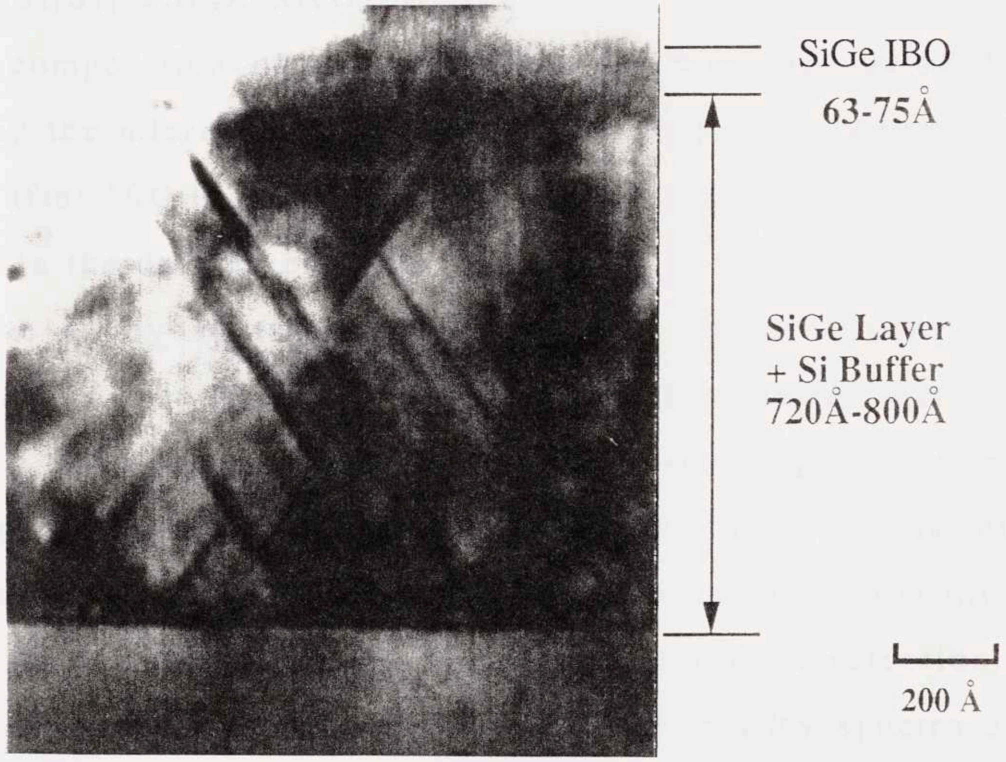

d) Off-axis TEM picture of 1 keV SiGe-IBO of a low defect density $Si_{1-x}Ge_x$ layer

Figures 5.17. (cont.)

surface but terminated inside the MBE layers without reaching the surface. The differences in epitaxial quality between the two types of samples were confirmed by RBS and ion channeling angular scans. The difference in microstructure resulted in a different morphology of the SiGe-dioxide films. In the defective films (Fig. 5.17a & b), the IBO oxides were rough and found to grow non-uniformly into the layer where a defect intersected the surface. On the low defect density layers (Fig. 5.17c & d), the IBO films had a sharp interface with the MBE layer and a uniform thickness. (Note that in the case of Fig. 5.17c, a Si cap was deposited by MBE after IBO of the $Si_{1-x}Ge_x$ film and reoxidized by IBO at 1 keV, to provide a heterodielectric structure ($Si/Si_{1-x}Ge_x/SiGeO_2/SiO_2$))

The composition of the alloy dioxide was also strongly affected by the microstructure (Fig. 5.16). The Ge retention in the oxide after IBO is much higher in the low defect density $Si_{1-x}Ge_x$ than in the defective layers. A possible explanation is that Ge is more easily sputtered away where a defect is present. Nevertheless, in both cases (defective and low defect density films), as the ion energy is decreased, the importance of sputtering decreases and the Ge/Si ratio after oxidation approaches the original Ge/Si ratio. Lower energies in IBO thus appear to favor both compositional uniformity and Ge retention.

Fig. 5.18 and 5.19 are typical 2 MeV $^4He^+$ RBS spectra of $Si_{1-x}Ge_x$ oxidized by IBO. The RBS spectra taken in the <110> channeling direction (Fig. 5.18) reveals the incorporation of ^{18}O and occasionally of some ^{16}O. The substrate channeling

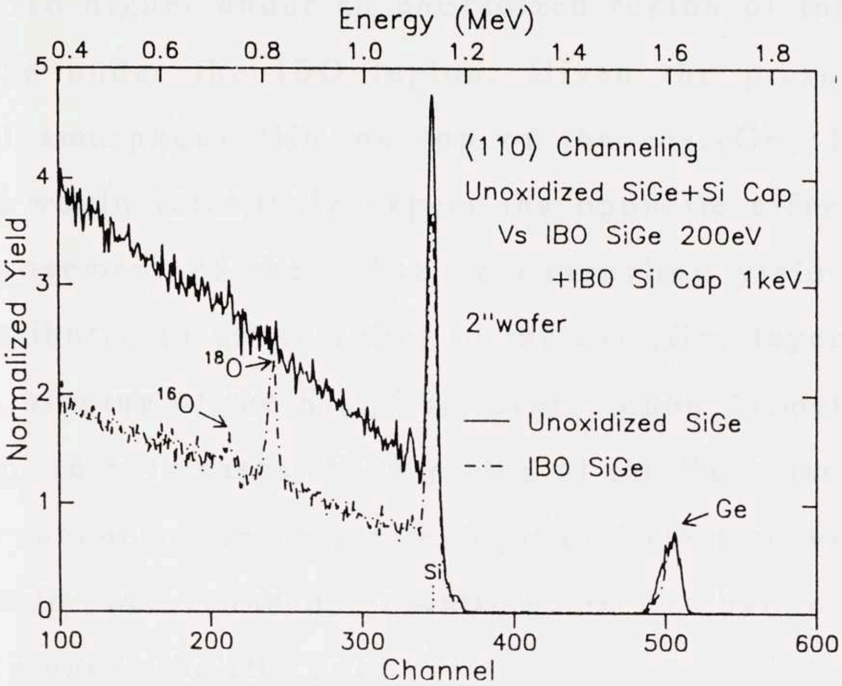

Figure 5.18. 2 MeV ^{4}He$^+$ RBS spectra in the <110> channelling direction for unoxidized $Si_{1-x}Ge_x$/Si (100) capped with an amorphous Si layer (50 Å) and oxidized $Si_{1-x}Ge_x$/Si (100) at 200 eV capped with oxidized Si at 1 keV on a 2" wafer (same sample as in Fig. 5.17c). Incorporation of ^{18}O and of some ^{16}O can be detected.

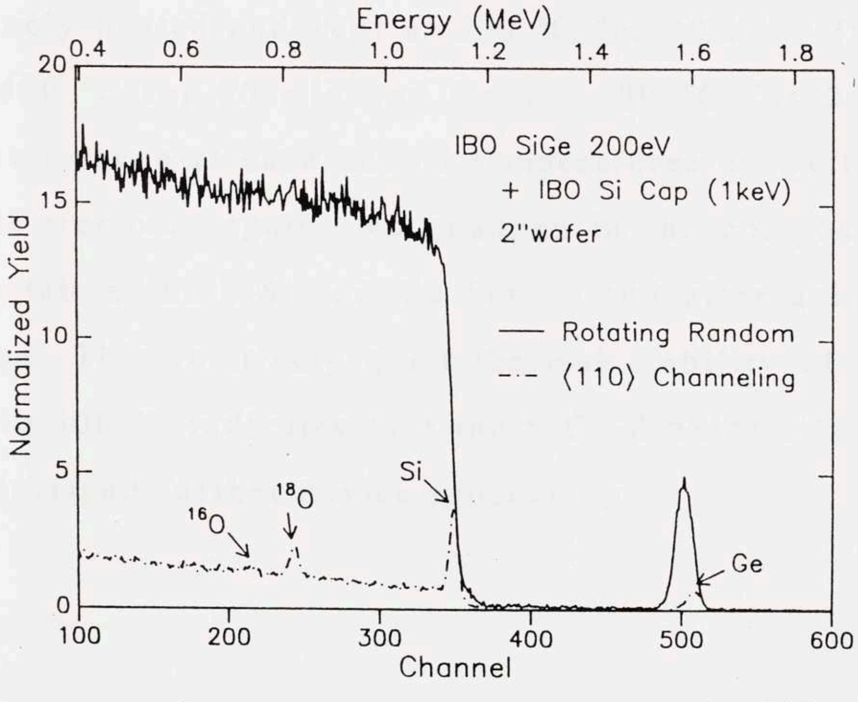

Figure 5.19. 2 MeV ^{4}He$^+$ RBS spectra in random and <110> channeling directions for the oxidized region of the sample of Fig. 5.17c

yield is also higher under an unoxidized region of the $Si_{1-x}Ge_x$ layers than under the IBO region. Given the presence of an additional amorphous film on top of the $Si_{1-x}Ge_x$ layer after IBO, one would intuitively expect the opposite effect at first. This improvement of the substrate channeling yield after IBO can be attributed to strain relief in the $Si_{1-x}Ge_x$ layers or to an effective thinning of the $Si_{1-x}Ge_x$ layers, upon formation of the oxide film. In both cases, the steering of the He beam out of the substrate channels due to the tetragonal distortion in the alloy layer would be reduced, resulting in a better substrate channeling under the IBO spot.

Lastly, the thermal stability of these new $Si_{1-x}Ge_x$ dielectrics was assessed by submitting a 200 eV SiGe-oxide to an in situ anneal monitored by XPS. The sample was progressively heated and kept at 200 °C for 30 min, 300 °C for 30 min, 400 °C for 30 min and finally 500 °C for 2 hr. XPS spectra were taken at each anneal temperatures as well as when the sample was cold again. No changes in the composition and chemical state of both Si and Ge before and after anneal could be detected. This relatively good thermal stability of the alloy oxide up to 500 °C indicates that the SiGe-dioxide films may be able to withstand further device processing.

5.2. ION BEAM OXIDATION OF GAAS

Ion Beam Oxidation of GaAs at room temperature was studied as a function of O_2^+ ion energy between 100 eV and 8 keV, in three sets of experiments.

Below 1 keV and at normal incidence, a thin oxide film is formed: it is composed of Ga_2O_3 and As_2O_3, and exhibits insulating properties. As the ion energy increases, preferential sputtering of As and decomposition of As_2O_3 increase and prevent formation of an insulating film. No damage in the substrate was detected by RBS combined with ion channeling for IBO performed below 1 keV.

a. GAAS IBO EXPERIMENTAL PROCEDURE

For all the IBO experiments, the same Czhokralski-grown, low resistivity GaAs (100) 3” substrate was used by cleaving small pieces.

In the first experiment, IBO of GaAs was explored for ion energies ranging from 1 keV to 8 keV using a VG duoplasmatron ion source (VG DP 2001/C) with in situ SIMS analysis. In this case however, the ion beam did not have a normal incidence but impinged at 30° off the normal. The O_2^+ ions were extracted at 10 keV and slowed down by biasing the target from 9 to 2 kV.

For the second experiment at 500 eV, an electron impact sputtering ion gun (Perkin-Elmer 04-303) was used to produce the IBO film with in situ Scanning Auger Microscopy (SAM). The O_2^+ ions were produced at 1 keV and decelerated to 500 eV at the target. In this case, special care was taken to have normal incidence.

For the experiments described above, the samples were sputter-cleaned in situ prior to IBO: the sputter-cleaning was done with 4 keV ions, Cs^+ in the SIMS, and O_2^+ in the SAM, for short duration (12 sec. to 1 min.) with a beam incidence of 30° to favor sputtering versus incorporation. This duration was optimized by experimentation prior to IBO, in order to remove most of the surface contamination of carbon and oxygen, while keeping the GaAs surface as stoichiometric as possible.

These first two IBO experiments were also conducted in a UHV environment ($5x10^{-9}$ Torr during IBO). With the ion sources used above, the oxygen ions were predominantly O_2^+, and not O^+. The ion current density ranged between 10 and 20 $\mu A/cm^2$. In each experiment, the time of exposure to the oxygen ion beam was determined to have the same total dose of O_2^+, namely 10^{17} ions/cm^2. The samples were characterized by ex situ XPS, SEM, and RBS with ion channeling technique.

The third set of experiments was conducted in the CIMD system in the same conditions as the IBO of group IV semiconductors. The GaAs samples were cleaned using the dip etch clean with a 30 sec dip in the HF:ethanol solution. This removed most of the carbon contamination and of the native oxide as determined by XPS. The remaining oxygen contamination was however still quite high (0.25 - 0.3 ML) and most of it was bonded to As in As_2O_3. As in the case of Ge, this is probably due to a less efficient and less stable passivation of the surface by H termination. The dip etch clean was however sufficient for the IBO experiments and provided a stoichiometric GaAs surface. In situ XPS was used to monitor the phase formation as a function of exposure to the ion beam. IBO was interrupted when the saturation level was reached. Oxygen ion energies were varied between 100 eV and 1 keV to study more precisely the role of ion energy on GaAs-oxide formation by IBO.

b. RESULTS OF IBO OF GAAS

The XPS analysis of the GaAs IBO layers is in general quite complex compared to that of group IV semiconductors. More photoelectron emmisions as well as Auger electron signals contribute to the XPS spectrum and more oxide phases can be formed and need to be identified. Table 5.3 summarizes the peak position and chemical shift in the oxide phases for the 3d photoelectron and $L_3M_{45}M_{45}$ Auger electron signals of both Ga and As [125]. The chemical shift in the Ga 3d signal between GaAs and Ga_2O_3 is quite small ($\Delta BE = 1.0$ eV). In addition, for very thin oxides, this chemical shift has been found to be incomplete, in a similar manner to the shifts found for thin SiO_2 films [126]. This makes the respective contribution of oxidized and unoxidized Ga to the Ga 3d signal difficult to separate accurately. Fortunately, the shift in the Ga LMM Auger peak is quite significant ($\Delta BE = 4.9$ eV) and easily observable. This helps identifying more accurately the degree of oxidation of Ga into Ga_2O_3. There is no such difficulty for As and its oxides since the chemical shifts in the 3d peak are large enough to resolve easily the different contributions.

	Ga 3d (eV)	As 3d (eV)	Ga LMM (eV)	As LMM (eV)
GaAs	19	41	hν - 1062	hν - 1225.6
Ga_2O_3	+ 1		+ 4.9	
As_2O_3		+3.5		+5.8
$GaAsO_4$	+1.9	+4.7		
As_2O_5		+4.7		

Table 5.3. Binding energies of the 3d photoelectrons and $L_3M_{45}M_{45}$ Auger electrons for Ga and As in GaAs and corresponding chemical shifts in the oxide phases [125]

The results of the first two sets of GaAs IBO are summarized in Fig. 5.20. The first spectrum in Fig. 5.20 is a reference spectrum taken on virgin GaAs, i.e. uncleaned and not exposed to any ion beam, and thus having retained a native oxide intact on the surface. The three other spectra (Fig. 5.20b, c & d) correspond to oxidized GaAs with three different ion energies, 500 eV, normal incidence (from SAM), and 1 and 3 keV, 30 ° incidence (from SIMS), respectively. By comparing the binding energy positions observed in Fig. 5.20 to the values in Table 5.3, it can be established that the oxidized states of Ga and As are Ga_2O_3 and As_2O_3, respectively, with no detectable presence of $GaAsO_4$ or As_2O_5.

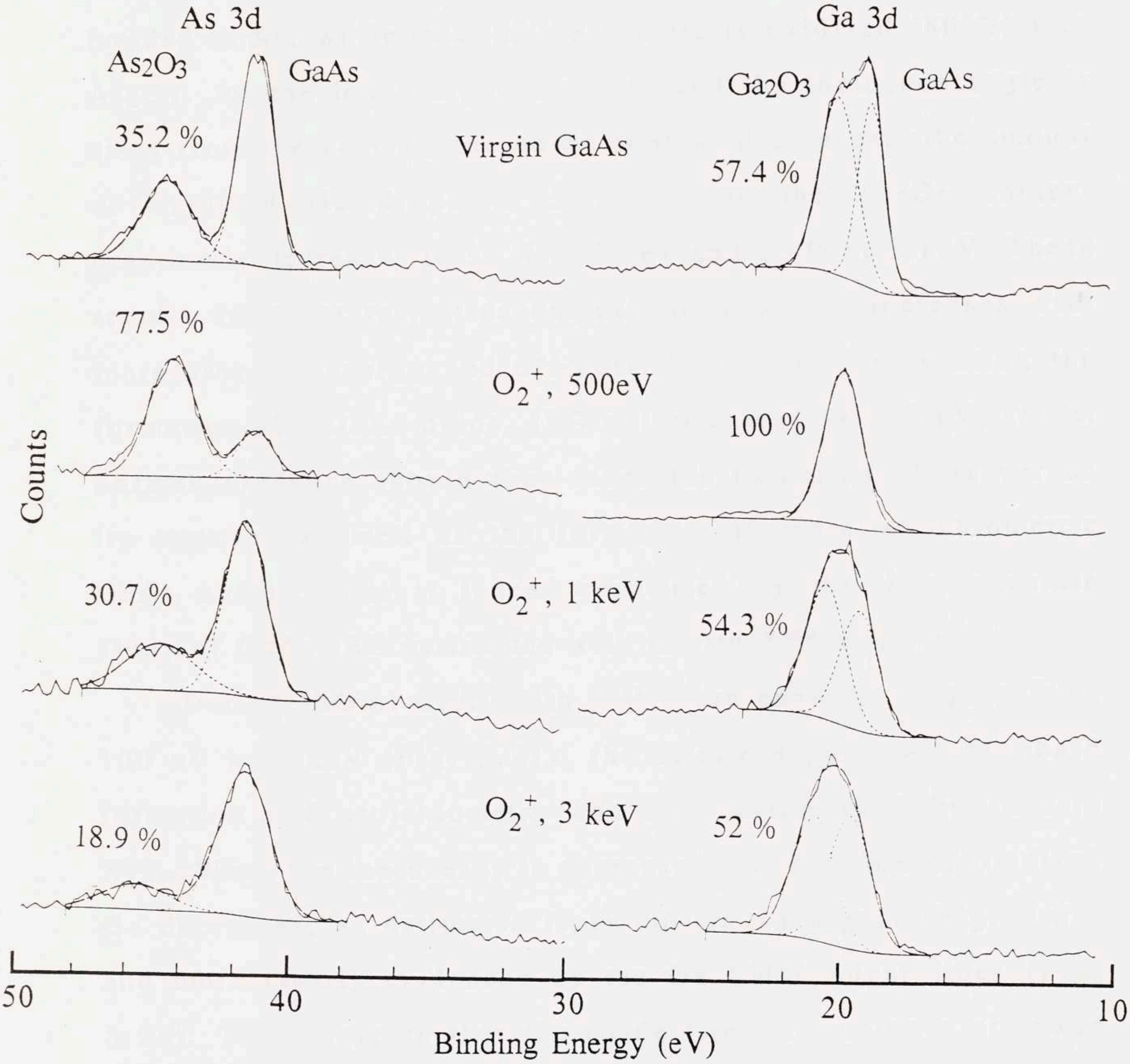

Figure 5.20. XPS spectra of (a) virgin GaAs, and IBO GaAs at (b) 500 eV, (c) 1 keV, and (d) 3 keV

At 500 eV, a dramatic difference is observed in the composition between the native oxide and the IBO film. The gallium seems completely oxidized into Ga_2O_3, with no Ga bonded to As, while most of the arsenic is oxidized (80 %) into As_2O_3. As the ion energy increases and the incidence angle is away from the normal, the oxide content decreases: the amount of oxidized Ga drops to 50 % while the As_2O_3 content drastically decreases to 30 % at 1 keV and 20 % at 3 keV. These results demonstrate that decomposition of As_2O_3 increases with increasing ion energy and off-normal incidence, preventing the formation of a GaAs-oxide. IBO at low energy (< 500 eV) and at normal incidence should thus favor the oxidation of As versus its removal as well as the formation of more stoichiometric GaAs oxides. This is indeed confirmed by the more accurate study of GaAs IBO performed with in situ XPS analysis.

During IBO of GaAs with ${}^{18}O_2^+$ ion energies ranging from 100 eV to 1 keV (Fig. 5.21), the strong dependence of phase formation and stoichiometry could be established by in situ XPS. When the ion energy is decreased, the fraction of oxidized Ga decreases, as estimated from the Ga 3d signal (Fig. 5.22) and more clearly evidenced by the Ga LMM Auger lines (Fig. 5.23). This suggests that the oxide films are thinner at lower energies, as was the case in IBO of group IV semiconductors. On the other hand, the fraction of oxidized As decreases significantly with increasing ion energy (Fig. 5.22). Similarly, the Ga:As ratio (Fig. 5.24), ideally equal to 1 in GaAs, increases dramatically during IBO at higher energies. This

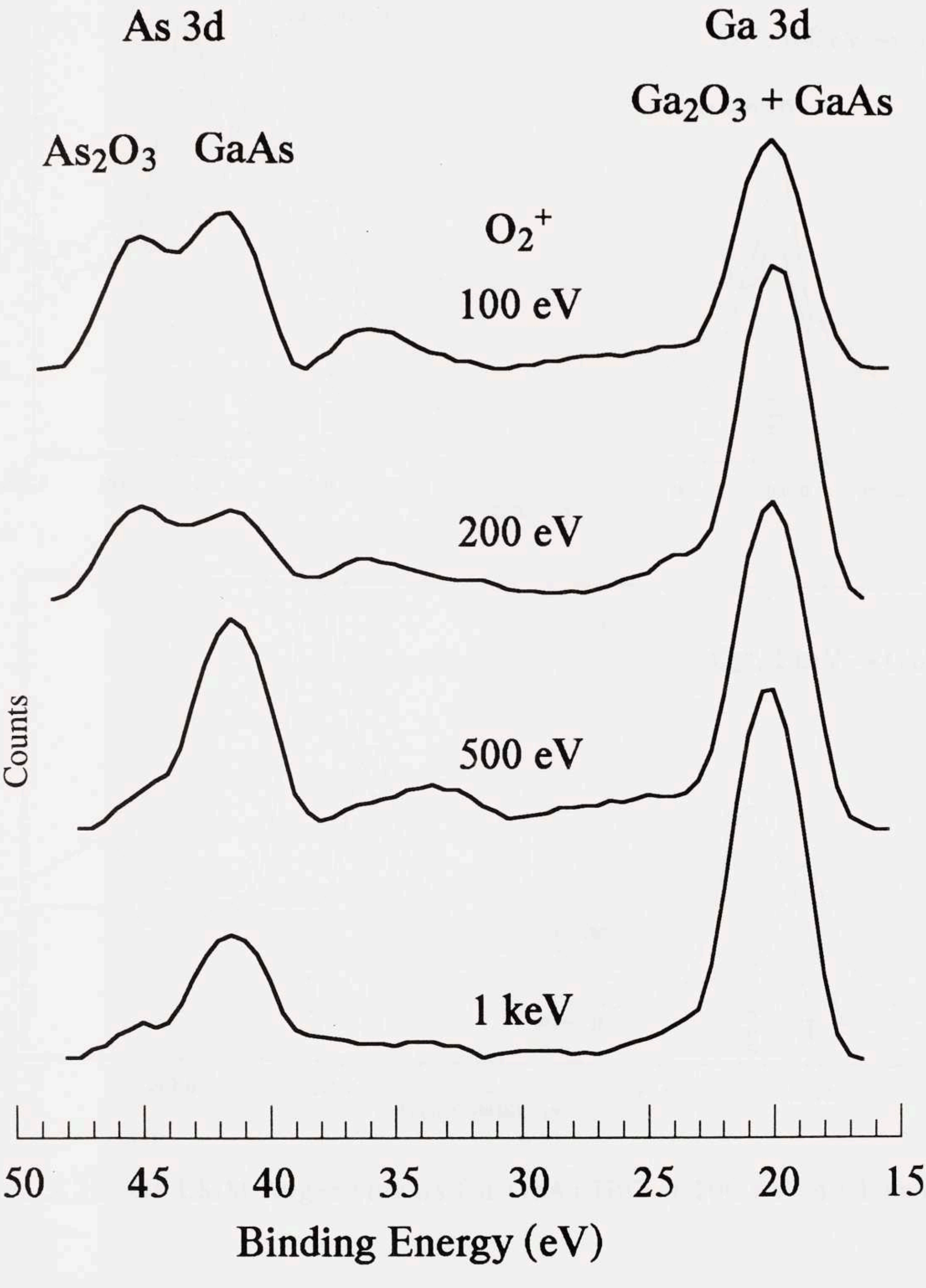

Figure 5.21. XPS spectra of Ga 3d and As 3d signals for GaAs IBO as a function of ion energy (100 eV - 1 keV)

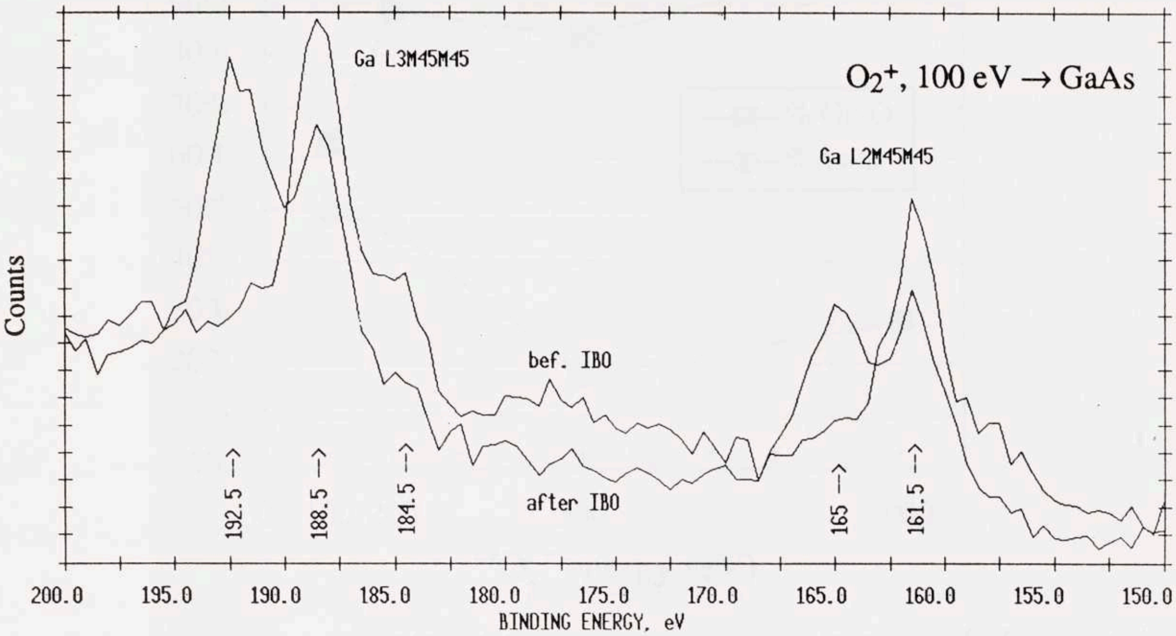

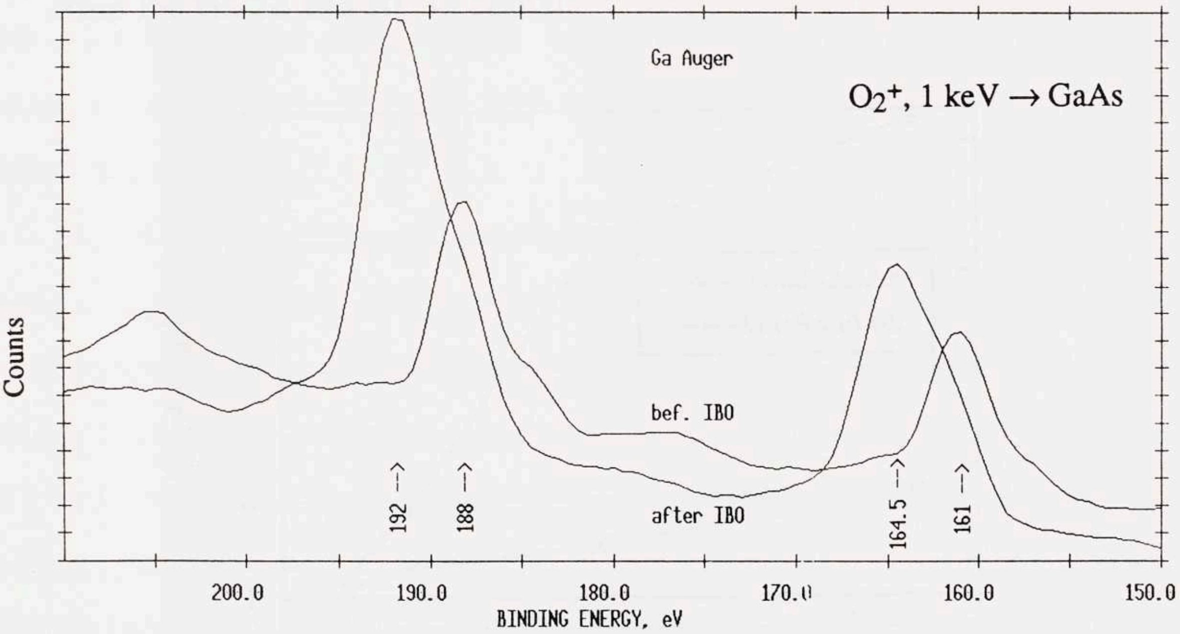

Figures 5.22. Ga LMM Auger signals for GaAs IBO at 100 eV and 1 keV

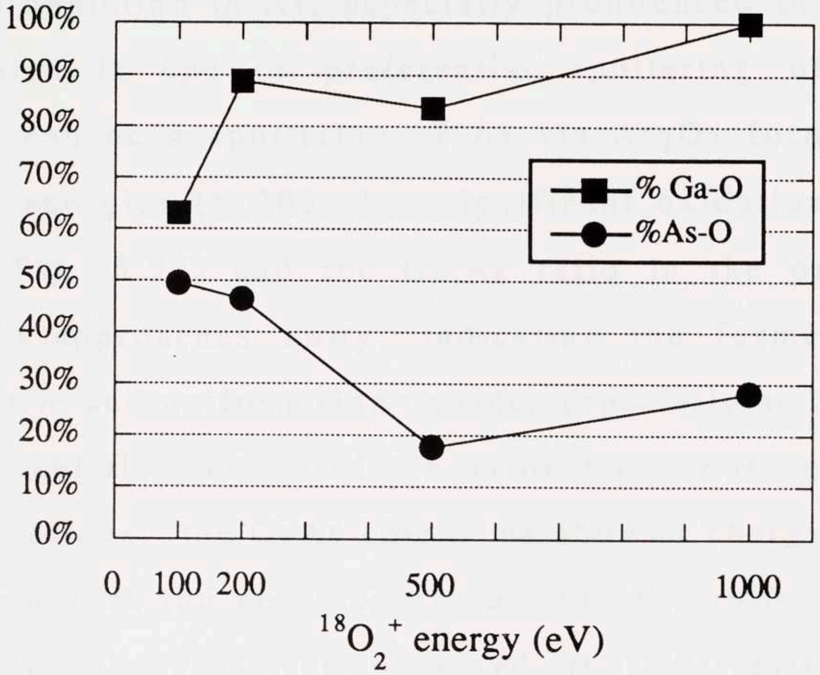

Figure 5.23. Fraction of oxidized Ga and As as a function of IBO energy from the Ga 3d and As 3d signals

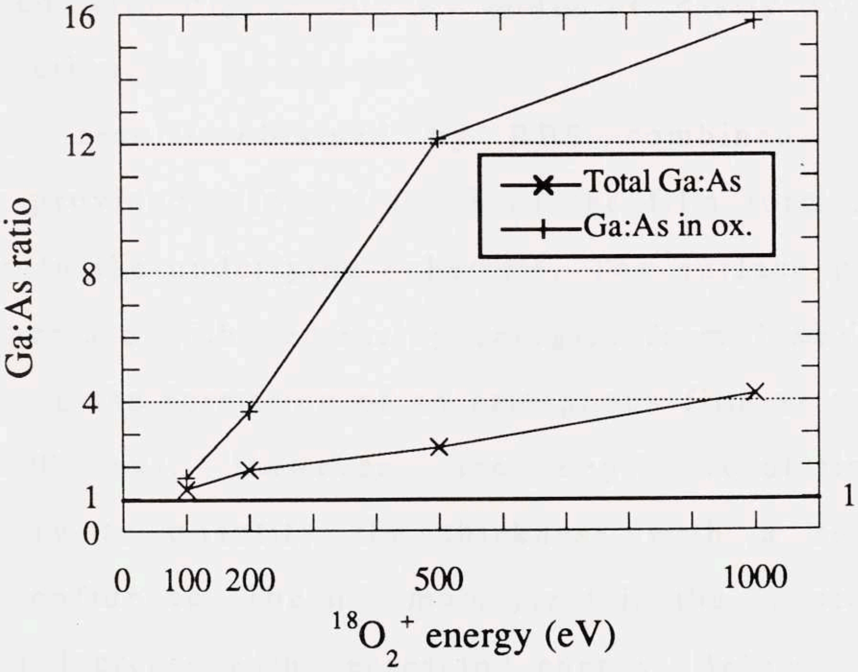

Figure 5.24. Ga:As ratio after IBO as a function of ion energy as determined by XPS from the Ga 3d and As 3d signals with the total intensity of both signals ("Ga:As total") and with the respective intensity of their respective oxidized fraction ("Ga:As in ox.")

indicates a depletion in As, especially pronounced in the oxide phase, which is due to preferential sputtering of As and chemically enhanced sputtering of As via As_2O_3 formation. At lower IBO energies (≤ 200 eV), significant oxidation of As is observed (Fig. 5.21) and the Ga:As ratio in the oxide layer (Fig. 5.24) approaches unity, indicating the formation of a stoichiometric and uniform GaAs oxide, especially at 100 eV.

The insulating nature of the oxide films was assessed by SEM observations: the GaAs IBO films showed charging effects when formed with ion energies up to 500 eV, while above 500 eV, charging was weak or not observed. It is interesting to note that visual inspection gave the complementary information: the IBO spots formed below 500 eV were not visible, while the spots formed with E_{ion} > 500 eV could be easily located by visual inspection.

Lastly, results obtained by RBS combined with ion channeling provided information about the film formation and the damage in the underlying substrate. The surface peak was found to increase with decreasing energies from 3 keV to 500 eV, indicating the formation of an amorphous film at the lower energy (500 eV). However, the depth resolution was unsatisfactory to quantify the thickness with a reasonable degree of confidence. The minimum yield in the substrate was observed to decrease with decreasing energy. Below 1 keV, it was found to be equal to the value for virgin GaAs (100) or 4 %. This establishes that the low energy used in IBO not only minimizes sputtering and oxide decomposition, but also prevents a massive incorporation of defects in the underlying substrate.

5.3 SUMMARY OF THE RESULTS

Low energy Ion Beam Oxidation of Si (100), Ge on Si(100) and MBE-grown $Si_{1-x}Ge_x$ on Si (100) as well as IBO of GaAs (100) was investigated at room temperature using $^{18}O_2^+$ with ion energies ranging from 100 eV to 1 keV. The dependence of phase formation and film properties upon ion energy was established. In the case of Si, thin films of stoichiometric SiO_2 are formed at each energy and their thickness increases from 39 Å to 70 Å with increasing ion energies. Insulating GeO_2 can only be formed for $E_{ion} \leq 200$ eV. Under IBO, both Si and Ge in the $Si_{1-x}Ge_x$ alloy are fully oxidized. At each energy investigated, thin SiGe-dioxide films are formed and found to be insulating by SEM. This contrasts with IBO of elemental Ge and shows that the presence of Si surrounding the Ge in the $Si_{1-x}Ge_x$ alloy enhances the oxidation of Ge by IBO. Due to preferential sputtering of Ge and beam induced decomposition of GeO_2, the Ge fraction in the SiGe-oxide is lower than the original Ge content of the alloy, especially at high energy. IBO performed at low energy ($\leq$ 200 eV) favors the retention of Ge in the SiGe-dioxide and minimizes the non-uniformity of the oxide composition with depth. The morphology and composition of the SiGe-dioxide was also observed to depend on the microstructure of the Si_{1-}

${}_xGe_x$ layers grown by MBE. Effective oxidation of GaAs and formation of an insulating film made of Ga_2O_3 and As_2O_3 can be achieved by IBO if the ion energy is low enough (≤ 200 eV).

6. THEORETICAL MODELLING OF THE IBO PROCESS

Ion Beam Oxidation (IBO) is a low temperature growth technique where a low energy (≤ 1 keV) ion beam introduces the oxygen into the substrate and athermally activate the chemical reaction leading to the oxide growth. In this work, IBO of Si, Ge, $Si_{1-x}Ge_x$ and GaAs was investigated experimentally as a function of ion energy from 100 eV to 1 keV. The results presented in the previous chapter show a strong dependence of the materials properties such as phase formation, stoichiometry, and thickness on the ion energy.

In this chapter, theoretical modelling of the IBO process is studied with the objective to account for the various experimental observations. Our approach to describe the IBO process is the following. Based on the general presentation of chapter 3, the effects of the three physical phenomena involved in IBO are successively investigated, namely:

1) ion incorporation and sputtering: model IS
2) model IS + Replacement / Relocation events (or ion beam mixing effects): model ISR
3) model ISR + oxygen diffusion and chemical reaction: model ISRD

The purpose of constructing models of increasing complexity as more phenomena are included is to identify the respective role and importance of each of these steps in the IBO process. For each model, a brief explanation of the program implementation is first presented, followed by the main results and correlations with the experimental observations.

6.1. IMPLANTATION / SPUTTERING MODEL: MODEL IS

a. DESCRIPTION OF THE MODEL IS

The IBO process can first be thought as a competing process between sputtering and oxygen implantation. Once the oxygen is incorporated, it will bond with available substrate atoms to form an oxide molecule. Upon oxidation, the volume expands, leading to net surface growth in the initial stage of IBO. The experimentally observed saturation of the IBO growth rate then results from the balance between the sputtering rate of the oxide layer at the surface and the oxidation rate of the substrate accompanied by volume expansion at the back interface. This balance results in a fixed and constant thickness of the IBO film which, in the IS model, depends solely on the ion-solid interaction, i.e. ion implantation and sputtering. The thickness is determined by the relative magnitude of the range and range straggling of the ion incorporation profile and of the sputtering yields of the different elements.

In the IS model, excess O_2 incorporated after saturation of the IBO growth is assumed to diffuse quickly to the surface and to desorb completely.

A similar IS model was developed by Todorov.et al. [127] for IBO of Si with similar assumptions for the chemical reaction, volume expansion and excess oxygen. An analytical formula was used to calculate the implantation profile and experimental values for the sputtering rate of SiO_2 and Si.

In the present IS model developed for IBO of single (Si, Ge) and multi-element ($Si_{1-x}Ge_x$, GaAs) targets, TRIMCSR is used to calculate the ion-solid interactions, i.e. the oxygen implantation profile and the sputtering profile. The sputtering profile provides the depth of origin of the sputtered recoil, usually involving the first two to three monolayers:

$$Y = \int_0^\infty y(z)\,dz$$

This enables the IS model to predict stoichiometry modification at the surface due to differences in sputtering yields with depth (y(z)). From the implantation and sputtering profiles calculated by TRIMCSR for homogeneous elemental and compound targets, a simple interpolation with renormalization to the ion dose is used to determine the implantation and sputtering profiles in the target when the composition varies during IBO. This procedure was found to be acceptable when checked with the more advanced model ISR which includes a dynamic version of TRIMCSR.

b. IS SIMULATION RESULTS

1. IS PREDICTIONS FOR IBO OF SI

The IS model can account for the 3 stages experimentally observed during IBO of Si: 1) formation of substoichiometric oxides, 2) rapid conversion into SiO_2 and 3) saturation of the IBO growth (Fig. 6.1).

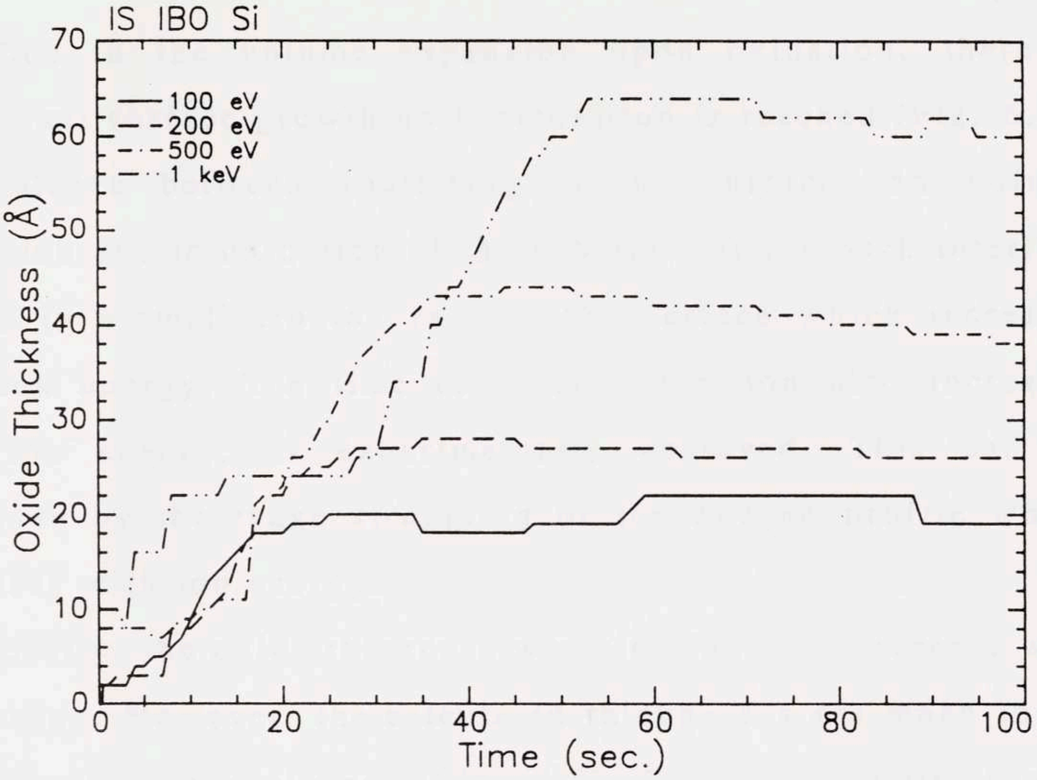

Figure 6.1. Oxide growth calculated by IS for IBO of Si at different ion energies

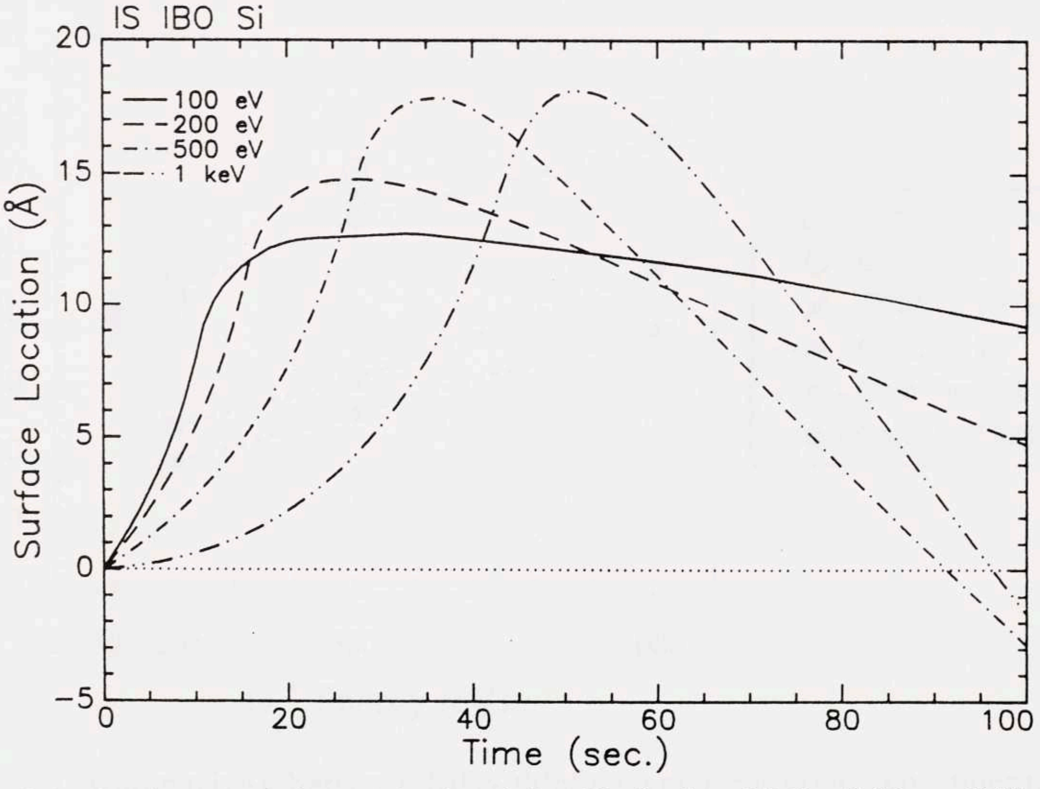

Figure 6.2. Surface location calculated by IS during IBO of Si at different ion energies

Due to the volume expansion upon oxidation, there is significant surface growth until saturation is reached (Fig. 6.2). The balance between sputtering at the surface and volume expansion due to oxidation of the substrate at the back interface results in a small erosion rate of the surface which increases with ion energy. The time to reach saturation also increases with ion energy, as experimentally observed. This can be explained by the range straggling of the oxygen profile which increases with ion energy.

Lastly, the oxide thickness was also found to increase with ion energy. However, the calculated thicknesses are much lower than the experimental ones (Fig. 6.3). This is in contrast with the model of Todorov et al. They claimed a good correlation

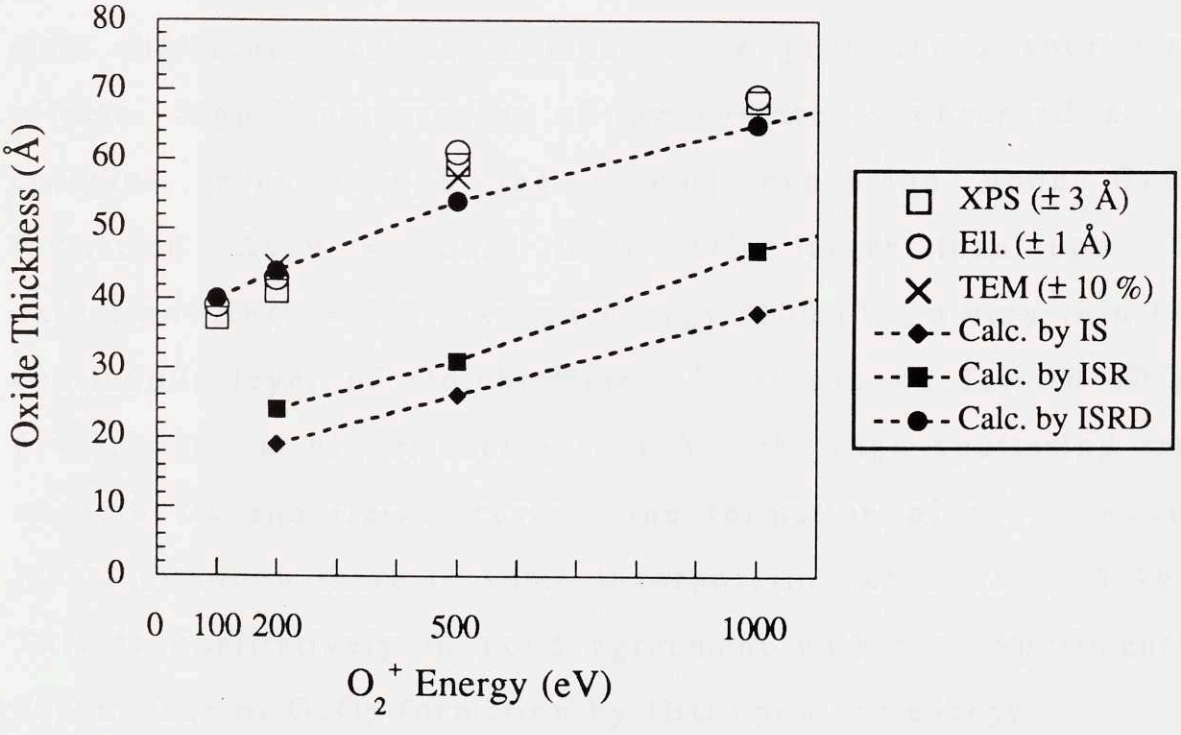

Figure 6.3. Comparison between SiO_2 thicknesses measured experimentally and calculated by the three models IS, ISR, ISRD.

between calculated and experimental thicknesses for ion energies between 60 and 100 eV. This might be due to the fact that they calculated the implantation profile using analytical formulas which are known to overestimate the range of the ions, especially at low energy. The rather large discrepancy between SiO_2 thicknesses observed in our experiments and calculated by our IS model indicates that the IBO process is not governed only by the competing processes of implantation and sputtering, but that a more refined and complete model needs to be developed.

2. IS PREDICTIONS FOR IBO OF GE

The IS results for IBO of elemental Ge are quite interesting and rather different from those for IBO of Si. The main difference resides in much more pronounced sputtering effects. Significant erosion of the surface is observed at all energies, even though the volume expansion upon GeO_2 formation ($\Delta V/V = 2.33$) is slightly larger than upon Si oxidation ($\Delta V/V = 2.2$). At low energy (100 eV), a very thin but continuous layer of stoichiometric GeO_2 can be formed (Fig. 6.4a), while at higher energy (1 keV), the high sputtering rate of both Ge and GeO_2 prevents the formation of a continuous layer, although there is some incorporation of O (Fig. 6.4b). This is qualitatively in good agreement with the experimental dependence of GeO_2 formation by IBO upon ion energy.

The IS model, although relatively simple, can thus provide insight into the phase formation by IBO.

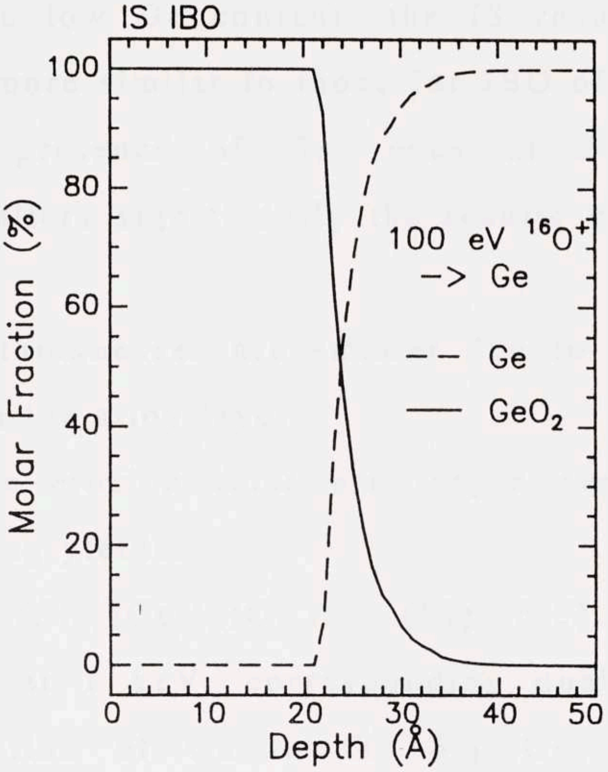

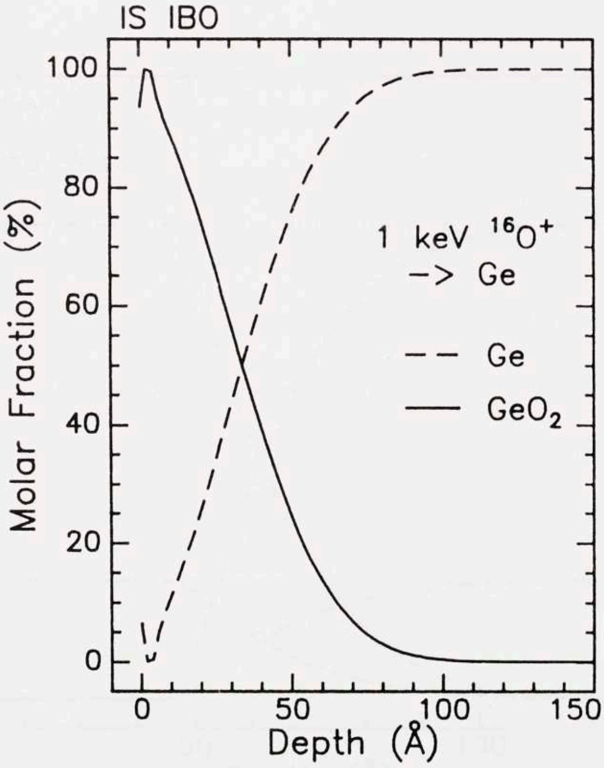

Figures 6.4. IS calculations of IBO of Ge at 100 eV and 1 keV

3. IS PREDICTIONS FOR IBO OF $SI_{0.8}GE_{0.2}$

Due to the low Ge content, the IS results for IBO of $Si_{0.8}Ge_{0.2}$ are more similar to those for IBO of Si than of Ge. However, the presence of Ge, even at a relatively low concentration, alters significantly the results compared to IBO of elemental Si:

- the oxide thicknesses are smaller due to the smaller ion range in the alloy layer
- the surface erosion rates are larger due to the larger sputtering yields.

A uniform $(Si_{0.8}Ge_{0.2})O_2$ film (Fig. 6.5) is formed at all energies, even at 1 keV, corresponding qualitatively to the enhanced oxidation of Ge in the $Si_{1-x}Ge_x$ layer observed

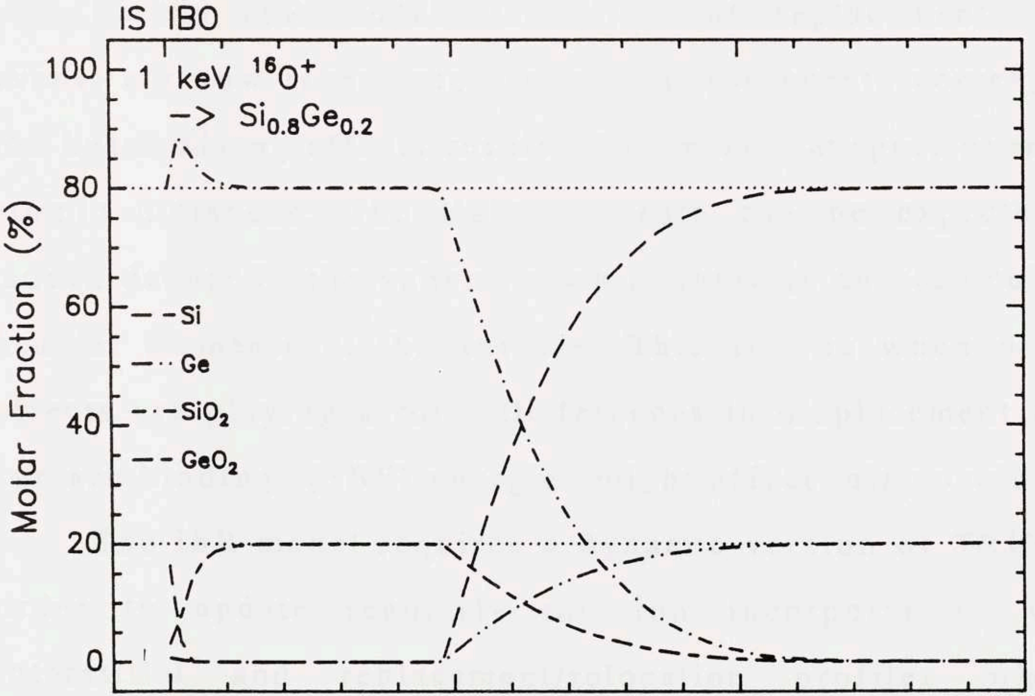

Figure 6.5. IS calculation of IBO of $Si_{0.8}Ge_{0.2}$ at 1 keV

experimentally. Variation with depth of the $Si_{0.8}Ge_{0.2}$-dioxide composition is only observed at the very shallow surface, due to differences in sputtering rates between Si and Ge, and does not correlate with the rather strong non-uniformity of the oxide composition with depth observed experimentally by XPS.

The advantage of the IS model is to be simple, fast and able to give some insight into the mechanism of phase formation resulting from the competing processes of oxidation and sputtering. However, it cannot account for the experimental thicknesses and depth composition of the IBO oxides.

6.2. MODEL IS + ION BEAM MIXING EFFECTS: MODEL ISR

a. DESCRIPTION OF THE MODEL ISR

In the ISR model, the effect of replacement/relocation events are now taken into account. These events corresponds to ion beam mixing effects resulting in mass transport over several atomic distances. The light elements can be expected to be moved deeper in the substrate while there is an accumulation of heavier elements at the surface. This is true when only mass effects are playing a role. Differences in displacement (E_d) and surface binding (SBE) energies might affect this conclusion.

The ISR model requires a dynamic version of TRIMCSR in order to update regularly the ion incorporation, vacancy, interstitial and replacement/relocation profiles while the composition of the substrate varies as IBO proceeds. The same assumptions as in the IS model are made however regarding the oxidation process itself: all the oxygen is bonded to the available substrate atoms and the excess oxygen is assumed to diffuse to the surface and to desorb completely.

ISR was mainly used to simulate IBO of Si and $Si_{0.8}Ge_{0.2}$ in order to evaluate the role of the ion beam mixing effects.

b. ISR SIMULATION RESULTS

1. ISR PREDICTIONS FOR IBO OF SI

The main effect of ion beam mixing in IBO of elemental Si is a significant increase of the SiO_2 thicknesses by about 20 % (Fig. 6.3). Some of the previously implanted oxygen is pushed deeper in by new incoming oxygen ions. The calculated thicknesses are however still significantly smaller than the observed thicknesses, indicating that other processes are taking place, such as oxygen diffusion.

2. ISR PREDICTIONS FOR IBO OF $SI_{0.8}GE_{0.2}$

As in the case of Si IBO, there is an increase in the oxide thicknesses, although less substantial (11 %). More importantly, the composition of the SiGe-dioxide is now strongly varying with depth (Fig. 6.6). Ion beam mixing leads to significant redistribution of the Si and Ge in the oxide layer. The surface region is depleted in Ge, while deeper in the oxide, there is an enrichment in Ge. This redistribution is quite opposite to the ion beam mixing intuitively expected based on mass effect consideration. It can be understood by the higher

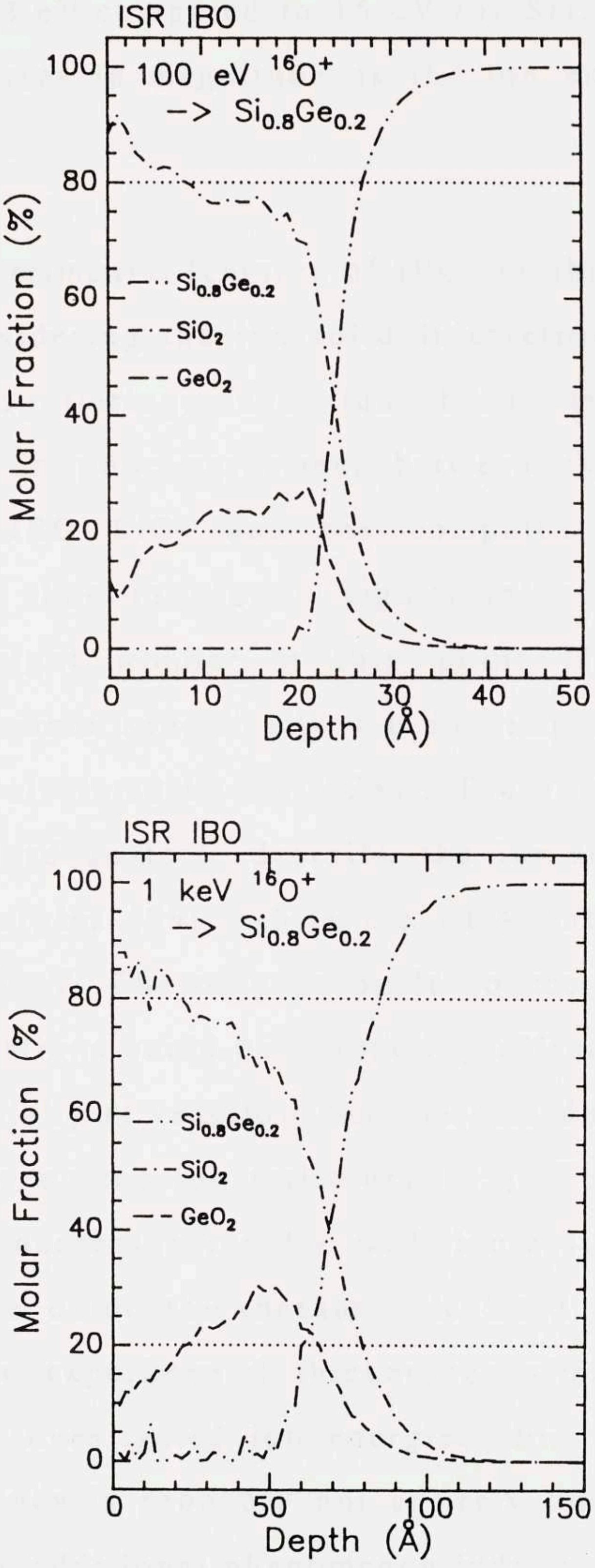

Figures 6.6. ISR calculations of IBO of $Si_{0.8}Ge_{0.2}$ at 100 eV and 1 keV

sputtering rate for Ge and GeO_2 and the lower displacement energy for Ge (13 eV compared to 15 eV for Si). The depth non uniformity increases in magnitude as the ion energy increases (Fig. 6.6).

Several experimental features of IBO can thus be accounted for only by considering the ion-solid interactions, namely ion incorporation, sputtering, and ion beam mixing effects. However, there is poor agreement between the experimental thicknesses of IBO SiO_2 and the computed ones. Oxygen diffusion seems thus to play a significant role in the IBO process. One might wonder at this point if the ion-solid interactions and more specifically the ion implantation profile are accurate as calculated by TRIMCSR. The universal potential has been proven adequate to describe the ion-solid interaction down to low energies [89], while the BCA only breaks down below 50 to 100 eV. The only probable source of error in the TRIMCSR calculations could be channeling effects which can be significant especially at very low ion energies due to increasing collective effects on the ion trajectory [85]. These channeling effects however decreases rapidly with increasing ion energy. The fact that the oxide thicknesses calculated by IS and ISR deviate from the experimental thicknesses similarly over the whole range of investigated ion energies (Fig. 6.3) indicates that the discrepancy is probably not entirely due to channeling effects, but to an additional phenomenon independent of the ion-solid interaction, which has to be taken into account.

6.3. MODEL ISR + OXYGEN DIFFUSION AND CHEMICAL REACTION: MODEL ISRD

a. DESCRIPTION OF THE MODEL ISRD

In the ISRD model, the ion-solid interactions as well as the oxygen diffusion and the chemical reaction are described simultaneously. The following continuity equations are solved numerically to describe the IBO of a two-element target (elements s and g):

Unreacted s: ss
$$\frac{\partial C_{ss}}{\partial t} = -k_{so} C_{ss} C_{oo} + g_{ss}$$

Unreacted g: gg
$$\frac{\partial C_{gg}}{\partial t} = -k_{go} C_{gg} C_{oo} + g_{gg}$$

Oxide phase of s: so
$$\frac{\partial C_{so}}{\partial t} = +k_{so} C_{ss} C_{oo} + g_{so}$$

Oxide phase of g: go
$$\frac{\partial C_{go}}{\partial t} = +k_{go} C_{gg} C_{oo} + g_{go}$$

Free oxygen: oo
$$\frac{\partial C_{oo}}{\partial t} = \frac{\partial}{\partial z}\left(D_o(z) \frac{\partial C_{oo}}{\partial z} \right) + g_{oo} - 2 k_{so} C_{ss} C_{oo} - 2 k_{go} C_{gg} C_{oo}$$

The substrate and oxygen atoms are either free or unbonded (ss, gg, oo) or they are bonded in an oxide phase (so, go). The above continuity equations contain three types of terms: 1) term k for the oxidation reaction, 2) term g for the ion-solid interaction, and 3) term D for the diffusion. These terms can be described as follows.

Term k: In ISRD, specific rates for the oxidation reactions are taken into account (k_{so}, k_{go}). The assumption that all the oxygen is bonded is eliminated: the concentration of unbonded or free oxygen is reduced by oxidation of the available substrate atoms. In a first approximation, the oxidation reaction is modeled as a chemical reaction of first order in the substrate atom and free oxygen concentrations

Term g: All the ion-solid interactions are taken into account in ISRD and calculated by the same dynamic version of TRIMCSR as in ISR. For each species, a generation term (g) represents its respective vacancies and interstitials creation and the ion beam mixing as a function of depth. For example, an oxygen vacancy corresponds to an oxygen taken away from an oxide molecule. In that case, the assumption is made that the entire oxide molecule is decomposed and that a free substrate atom and another free oxygen are created. This is of course the worst case situation for oxide growth, but is a reasonable way to take into account the ion beam induced decomposition of some oxide molecules.

Term D: in this version of ISRD, only the diffusion of free oxygen is modeled. The diffusion of unbonded substrate atoms and oxide molecules is not considered because it is not expected to be significant.

The diffusion of free oxygen is assumed to occur via two mechanisms represented by:

$$
\begin{aligned}
D_O &= D_{thermal} + D_{rad.enh.} \\
&= D_{O,sg}\, x_{sg} + D_{O,ox}\, x_{ox} + D_{enh.}\, (n_{vac}+n_{istl})/n_{ion}
\end{aligned}
$$

- the first diffusion mechanism ($D_{thermal}$) is conventional thermal diffusion described by a constant diffusion coefficient for atomic oxygen in the substrate ($D_{o,sg}$) and in the oxide layer ($D_{o,ox}$). A linear interpolation is made to determine the thermal diffusion coefficient of O as the composition in the structure varies.

- the second component to O diffusion is what can be called "radiation enhanced" diffusion ($D_{rad.enh.}$): during the ion-solid interaction, point defects are instantaneously created and can mediate the O diffusion. A nominal value (D_{enh}) is assumed and the radiation enhanced diffusion coefficient is made directly proportional to the number of defects (vacancies and interstitials) created by the ions at a specific depth. It is thus a strong function of depth, but with no effect beyond the end of range of the damage.

The free oxygen, allowed to diffuse in the ISRD model, can move towards the deep interface where it can react with the underlying substrate, or towards the top surface where it can eventually desorb. The surface boundary condition represents the assumption made on the O desorption. A fixed value for the surface flux can be chosen positive (incorporation) or negative (desorption), or the concentration of free oxygen at the surface can be set to 0, corresponding to a "fast" desorption only limited by the arrival of O from the bulk by diffusion.

A last option included in ISRD is the association of free oxygens into O_2 molecules which has its own diffusion equation. The corresponding continuity equations are the following:

Free oxygen: oo
$$\frac{\partial C_{oo}}{\partial t} = \frac{\partial}{\partial z}\left(D_o(z) \frac{\partial C_{oo}}{\partial z} \right) + g_{oo} - 2\,k_{o2} C_{oo} - 2\,k_{so} C_{ss} C_{oo} - 2\,k_{go} C_{gg} C_{oo}$$

O_2 molecules: o2
$$\frac{\partial C_{o2}}{\partial t} = \frac{\partial}{\partial z}\left(D_{o2}(z) \frac{\partial C_{o2}}{\partial z} \right) + k_{o2} C_{oo}$$

where k_{o2} is the chemical rate constant for the association of oxygen into O_2. This option was not exploited any further in the present study.

The five (or six) continuity equations form a set of non-linear and coupled differential equations. A finite element method is used for the discretization in space and an implicit forward Euler scheme for the discretization in time. The numerical equations are then solved using a self-consistent iteration method.

b. ISRD PREDICTIONS FOR IBO OF SI

The ISRD model was used primarily to account for the experimental observations made during IBO of elemental Si, and especially to obtain quantitative predictions for the IBO SiO_2 thicknesses as a function of ion energy.

In all simulations, a relatively large reaction constant k_{so} ($10^4/\Omega_{so}$ cm^3/sec, where Ω_{so} is the molecular density of SiO_2) for oxidation was assumed. This choice was based on the well-established knowledge of a strong driving force for Si oxidation, and experimental evidences such as the formation of buried oxides by high energy oxygen implantation (SIMOX) [128] performed at liquid nitrogen temperature (77 K) [129].

The effects of oxygen diffusion, both thermal and enhanced, and of the O desorption at the surface were investigated. Three cases were considered (Fig. 6.7): 1) only thermal diffusion and no enhanced diffusion, 2) no thermal diffusion and only enhanced diffusion, and 3) both thermal and enhanced diffusion.

1. ONLY THERMAL DIFFUSION AND NO ENHANCED DIFFUSION

If the free oxygen is allowed to diffuse thermally in the oxide ($D_{O,ox} > 10^{-15}$ cm^2/sec), the oxide keeps growing with time (almost linearly) with a rate proportional to the diffusion coefficient and no saturation regime of the IBO growth is observed (Fig. 6.7). Assuming a large desorption flux does not change this conclusion. If, on the other hand, the O thermal diffusion is small ($D_{O,ox} < 10^{-15}$ cm^2/sec), the oxide thickness does not increase significantly with time and remains equal to the thickness given by the ISR model. However, the concentration of free oxygen increases in the subsurface region to very high levels (up to 5×10^{23} O/cm^3), which is physically unrealistic. Assuming a high desorption rate is not changing this conclusion either, since the free oxygen cannot outdiffuse.

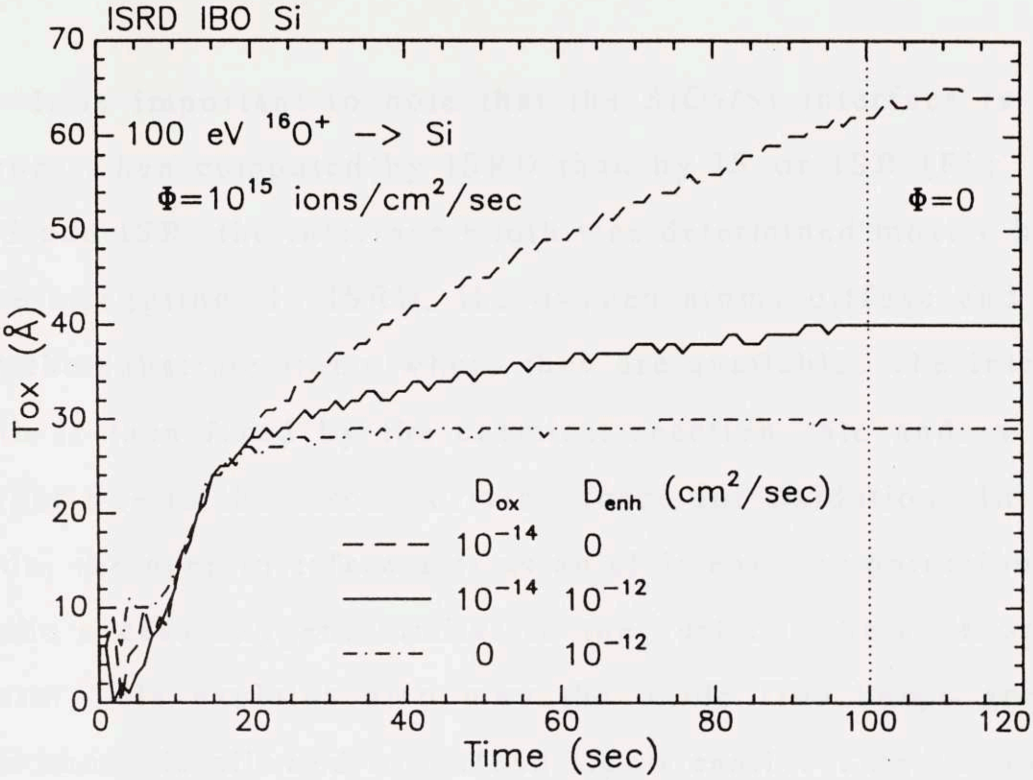

Figure 6.7. SiO_2 IBO growth calculated by ISRD assuming different thermal and enhanced diffusivities for oxygen

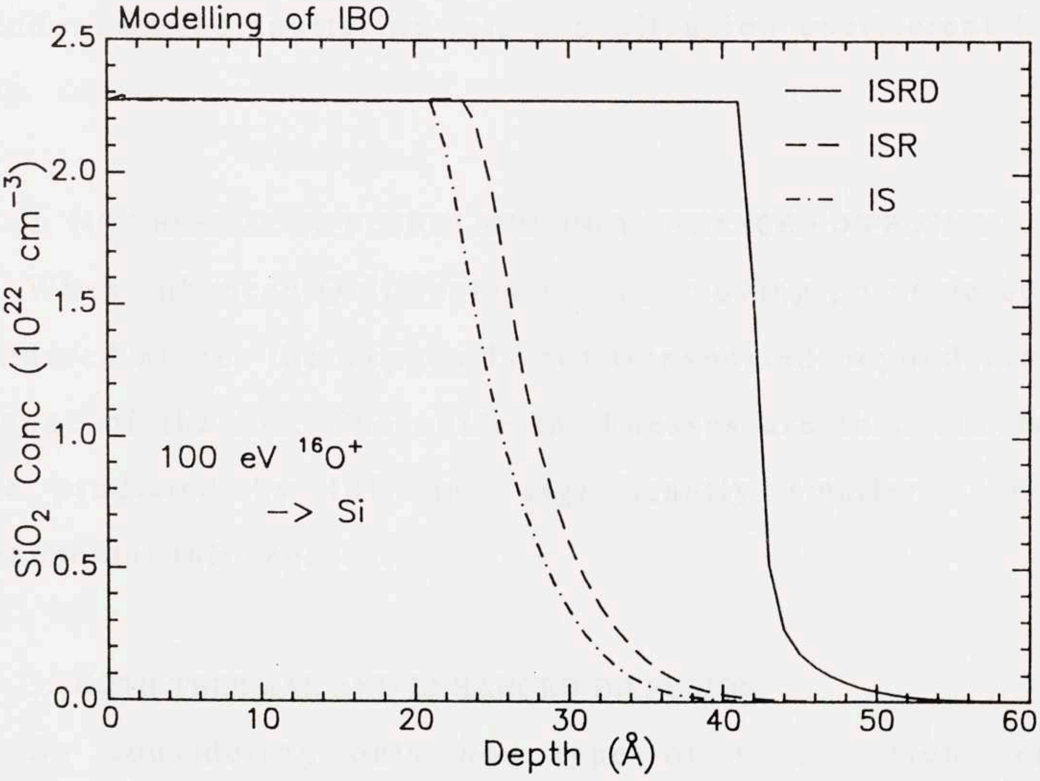

Figure 6.8. Comparison of the SiO_2 profile as a function of depth calculated by the three models IS, ISR, ISRD

It is important to note that the SiO_2/Si interface is much sharper when computed by ISRD than by IS or ISR (Fig. 6.8). In IS and ISR, the interface width was determined mostly by the range straggling. In ISRD, the oxygen atoms diffuse and react with the substrate atoms where they are available. The interface width is then fixed by the chemical reaction rate and is much sharper due to the strong driving force for oxidation. In other words, the deep interface acts as an efficient recombination sink for the excess oxygen, similar to the surface where desorption occurs. This explains also why the oxide film keeps growing when the O is allowed to diffuse significantly. This is actually the basic idea of the analytical model for high dose nitridation developed by O.C. Hellman [1]. The growth rate is then only dependent on the sputtering rate and diffusion coefficient in the oxide.

2. NO THERMAL DIFFUSION AND ONLY ENHANCED DIFFUSION

When enhanced O diffusion by fast moving point defects is considered alone, the oxygen is not transported beyond the end of range of the ion. The oxide thicknesses are then similar to those predicted by ISR and significantly smaller than the experimental thicknesses.

3. BOTH THERMAL AND ENHANCED DIFFUSION

By considering only one type of O diffusion, either thermal or point defect enhanced, one cannot account simultaneously for both the IBO saturation regime and the oxide thicknesses. This indicates that both types of diffusion are playing an important role. Indeed, by assuming both significant thermal diffusion in the oxide ($D_{o,ox} = 10^{-14}$ cm^2/sec) and point defect mediated diffusion ($D_{enh} = 10^{-12}$ cm^2/sec), the oxide thicknesses were found to be larger than calculated by ISR, but did not keep increasing with time, corresponding to the saturation regime (Fig. 6.7). This can be explained as follows. The thermal diffusion transports the O over some distance, making the SiO_2 thicker than predicted by the ion-solid interactions (ISR). However, the creation of defect close to the surface favors the migration of free oxygen towards the surface with subsequent desorption and impedes further incorporation of O deeper in the structure, leading to the saturation of the oxide growth. The point defect mediated diffusion of O thus acts as a depth dependent diffusivity preferentially directed towards the surface. It is interesting to note that a stress dependent diffusivity would have the same effect.

Assuming a thermal and enhanced diffusion coefficients equal to 2×10^{-14} and 10^{-12} cm^2/sec respectively, a remarkably good agreement (Fig. 6.3 & 6.9) can be observed between the calculated values and the experimental thicknesses measured in our study at low energy (100 eV - 1 keV) and by Augustus et al. [123] for an IBO SiO_2 film formed with 4 keV O_2^+.

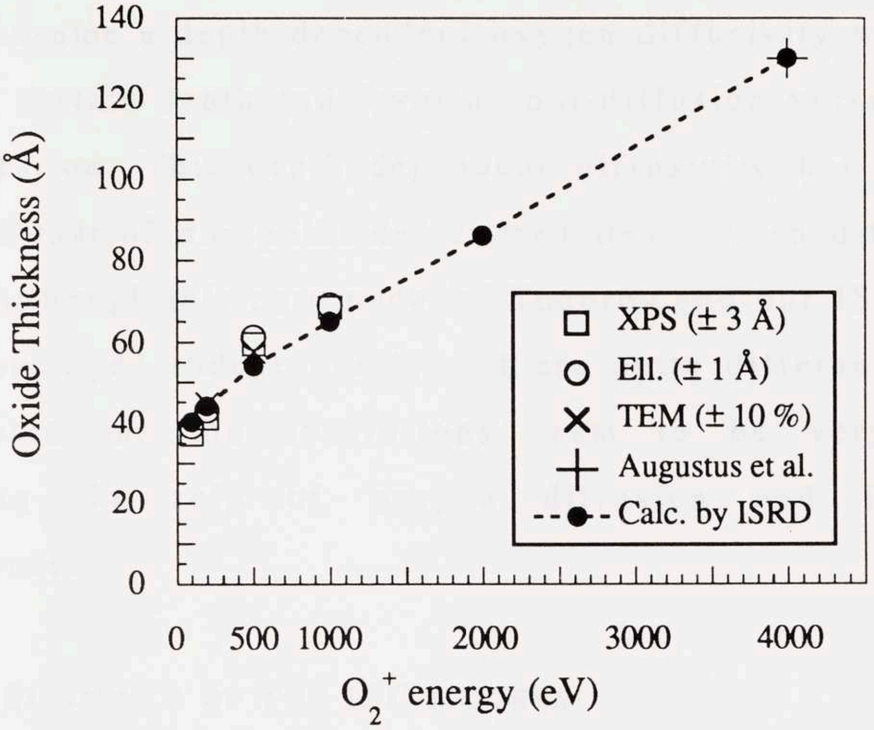

Figure 6.9. IBO SiO_2 thicknesses calculated by ISRD and measured experimentally as a function of ion energies between 100 eV and 4 keV

The ISRD model can thus account for all the experimental observations made for IBO of Si: the three stages of IBO growth (Fig. 6.7), the dependence of SiO_2 thickness with ion energy (Fig. 6.9) and the formation of a sharp interface with the substrate (Fig. 6.8). The ISRD model also shows that the saturation regime is not the consequence of a competing process between oxidation and sputtering (model IS), but results from two competing mechanisms of oxygen diffusion.

Very recently, Todorov et al. [130] improved their IS model by using TRIM to calculate the O incorporation profile and including oxygen diffusion. To predict correctly the thickness of an IBO SiO_2 layer formed with 100 eV O_2^+, they had to assume a depth dependent oxygen diffusivity with a cut-off at a certain depth and favoring out-diffusion versus further incorporation. This depth dependent diffusivity has a similar effect to that of our point defect mediated oxygen diffusion in ISRD. Although this new model of Todorov and our ISRD model were developed independently and are quite different in their implementation, the conclusions seem to be very similar regarding the role of oxygen diffusion and its depth dependence.

6.4. SUMMARY OF THE IBO MODELS

In order to investigate the kinetics of IBO and to account for the observed relationship between ion energy and films properties, three models of increasing complexity were developed. These models progressively take into account the ion incorporation and sputtering, the ion beam mixing effects, and the diffusion and chemical reaction leading to the oxide formation. This allowed us to highlight the role of each phenomenon in the IBO process. The programs can simulate single (Si, Ge) or multi-element targets ($Si_{1-x}Ge_x$ alloy, GaAs). The simulation results show that a model based only on implantation and sputtering cannot explain the thicknesses observed experimentally, but can give qualitative information on the phases formed by IBO (e.g. IBO of Ge). Ion beam mixing effects bring a first correction and are especially important in the spatial redistribution of the elements in compound targets resulting in a change of stoichiometry with depth (e.g. IBO of $Si_{0.8}Ge_{0.2}$). Oxygen thermal and radiation enhanced diffusions and the strong driving force for oxidation must be taken into account to simulate the observed thicknesses and sharp interfaces. Good correlations can be made regarding the dependence of phase formation and stoichiometry on the ion energy and the overall kinetics of the IBO process in three stages.

7. CONCLUSIONS ON THE EXPERIMENTAL AND THEORETICAL WORK.

In this chapter, we want to give conclusive remarks between the experimental results and the theoretical models for the different materials (Si, Ge, $Si_{1-x}Ge_x$, GaAs) and low energy ion beam techniques (IBD, IBO, IBN) investigated.

7.1. SIMILARITIES BETWEEN $SI_{1-X}GE_X$ AND GAAS

There are important similarities between IBO of the alloy $Si_{1-x}Ge_x$ and the III-V compound GaAs. In both systems, one of the constituents, Si in $Si_{1-x}Ge_x$ and Ga in GaAs, can form a stable and refractory oxide (SiO_2, Ga_2O_3 respectively), while the other constituent (Ge, As) is more volatile in both elemental and oxide forms. During IBO of both materials, we observe a decrease in concentration of the more volatile element due to preferential sputtering effects and a non-uniformity of composition with depth due to ion beam mixing effects. When the IBO energy is decreased, these effects decrease in importance. The formation of the alloy or compound oxide is then controlled primarily by the incorporation of oxygen and the strong driving force to form oxides. More stoichiometric and more uniform oxides are thus formed at lower energies, emphasizing the importance of performing IBO at low energies ($\leq$ 200 eV).

7.2. COMPARISON BETWEEN IBO AND IBN

In this section, important similarities and differences between IBO and IBN of Si, Ge and $Si_{1-x}Ge_x$ performed in the same conditions are pointed out, with special emphasis on the role of ion energy on phase formation.

IBN of Si using N_2^+ ions with energies from 100 eV to 1 keV [1] results in the formation Si_3N_4 films with an amorphous Si layer underneath. Most of the amorphous layer is nitrogen poor. The thickness of the amorphous layer is increasing at lower energies and higher implanted doses, while the nitrogen-rich region seems to increase in thickness with energy. This was revealed by combining characterization by XPS, cross-section TEM, and RBS. The dependence of the nitride film thickness and composition on the ion energy and substrate temperature suggests that the growth kinetics of IBN is different than that of IBO. In IBN, the diffusion is found to play a more predominant role than the chemical reaction, probably due to the smaller driving force for nitridation than for oxidation [131].

In the case of IBN of elemental Ge, the energy dependence of the nitride phase formation is even stronger than in IBO. Ge exhibits signs of nitridation only at 100 eV and the Ge_3N_4 film has poor insulating properties. Above 100 eV, no significant nitridation of Ge is detected. This can be attributed to the very small enthalpy of formation for Ge_3N_4 (15.6 kcal/mole) compared to GeO_2 (128.4 kcal/mole) [132]. In addition, the dissociation energy for Ge_3N_4 is negative (-102 kcal/mole

[133]) indicating that this phase can be easily dissociated with no energy barrier.

IBN of $Si_{1-x}Ge_x$ presents several similarities with IBO of $Si_{1-x}Ge_x$. During IBN of the $Si_{1-x}Ge_x$ layer, the presence of Si in the alloy enhances the nitridation of Ge and insulating SiGe-nitride films are formed at all energies studied (100 eV - 1 keV). Preferential sputtering of Ge and its nitride with respect to Si and Si_3N_4 makes the Ge content decrease in the alloy nitride. At the lower energies, the sputtering effects decrease and the remaining fraction of Ge in the SiGe-nitride increases. However, the retention of Ge is lower in the alloy nitride than in the alloy oxide. This can be put in parallel with the dependence of phase formation observed in IBO and IBN of elemental Ge, which shows that Ge_3N_4 is more difficult to form than GeO_2.

7.3. COMMON FEATURES TO IBD AND IBO

In both models for IBD (DRIVIC) and IBO (ISRD), the thin film growth kinetics could be accounted for only if the diffusion of the active species (interstitial in IBD and free oxygen in IBO) was appropriately described. We also showed the importance of using ions with low energy in order to confine the ion-solid interaction to the subsurface region. In IBD, this results in favoring surface recombination and vacancy annihilation of the interstitials. In IBO, the radiation enhanced diffusion of the free oxygen in the subsurface region leads to the desorption of the excess oxygen and to the saturation of the oxide growth.

There is also a parallelism to be noticed between the vacancy-interstitial recombination in IBD and the oxidation reaction in IBO. In both cases, the strong driving force for these point defect reactions plays a major role in the thin film formation and is responsible for the good material properties of the layer formed, such as depth uniformity, sharpness of the interface, elimination of excess defects and in the case of the oxide, stoichiometry. This driving force seems to be less effective in IBN, resulting in larger parasitic effects of processes such as diffusion and accumulation of defects, leading to poor or different properties such as amorphization of Si and non-stoichiometric nitride films.

8. ELECTRICAL CHARACTERIZATION OF THE IBO OXIDES

Advanced MOS technologies, such as submicron delta-doped Si MOSFET's for ULSI and emerging heterostructures $Si_{1-x}Ge_x$ MOS devices, require the ability to grow thin (≤ 100 Å) oxide layers of high electronic quality. Direct Ion Beam Oxidation (IBO) is a low temperature (300 - 700 K) technique which uses a low energy (≤ 1 keV) ion beam to introduce oxygen directly into the substrate and to activate athermally the chemical reaction, leading to a thin oxide growth. The low temperature nature of IBO is a key advantage to preserve the integrity of temperature sensitive structures such as delta-doped Si and strained $Si_{1-x}Ge_x$ layers. The low energy of the ions also insures a minimal injection of defects into the substrate. Lastly, the confinement of the ion beam avoids any contamination by oxygen, allowing epitaxy and oxidation to be done in a unique UHV chamber. This was our ultimate motivation for the investigation of IBO of Si and $Si_{1-x}Ge_x$. We therefore wanted to conclude our Ph.D. research by assessing the electronic properties of the IBO oxides and possibly the viability of IBO in device processing.

This chapter presents the results of the electrical characterization of the IBO MOS structures and circuits that we fabricated. These results are however far from those expected. Strong non-idealities were indeed observed in the characteristics of the MOS structures. Part of these non-idealities are probably intrinsic to the IBO oxides, but it appeared that we also suffered from rather important contamination problems which were extrinsic to the IBO process. Quantitative analysis of the electrical properties of the IBO oxides was therefore hindered and only qualitative trends will be discussed, when possible. We felt nevertheless it was important to report these relatively poor results because the identification of their origin can help in improving the electronic characteristics of IBO MOS structures in future experiments.

Two types of electrical characterization were performed in parallel. Capacitance-Voltage (CV) and Current-Voltage (IV) measurements were made on the as-grown IBO samples. MOS test circuits with the IBO oxides of Si and $Si_{1-x}Ge_x$ used as the gate dielectrics were also fabricated and characterized. For both types of characterization, thin thermal oxides (60 - 70 Å), grown by dry oxidation at 900 °C for 10 min of a 2" Si (100) wafer, served as a reference to compare the electronic properties of the IBO oxides.

8.1. CV AND IV MEASUREMENTS

CV and IV curves were measured using a HP probe station consisting of a multifrequency LCR meter (HP 4275A), a pA-meter (HP 44140B) and a semiconductor parameter analyzer (HP 4145A). The contacts were taken on the as-grown MOS structures (thermal dry oxide and IBO oxides) with an indium wire, which is a soft metal, in order to avoid damaging or punching through the very thin oxide layers. The drawback of using a wire tip is that the contact area is not known and seems to vary quite significantly from one measurement to another (by a factor of up to 5), even if the procedure to place the wire is systematized. The results can nevertheless be interpreted qualitatively, with the thermal oxide serving as a reference.

a. IBO OF SI

Fig. 8.1 shows the CV curves measured at 1 MHz on the IBO Si oxide formed at 100 eV. In general, similar curves could be obtained for the other IBO SiO_2 films. The three regions of accumulation, depletion and inversion, characteristic of high frequency CV curves, are observed. However, some non-idealities can be detected as well:

- the flat band voltage is relatively negative, indicating a large amount of fixed oxide charges
- the slope of the CV curve in the depletion region is not as steep as can be expected for oxide layers of such small thickness (40 - 70 Å), indicating probably a large amount of interface states
- hysteresis and instabilities in the CV (not seen in Fig. 8.1) can also be observed, corresponding to contamination by mobile charges and/or carrier injection and trapping in the oxide.

These 3 non idealities are typically encountered for SiO_2/Si structures of low quality.

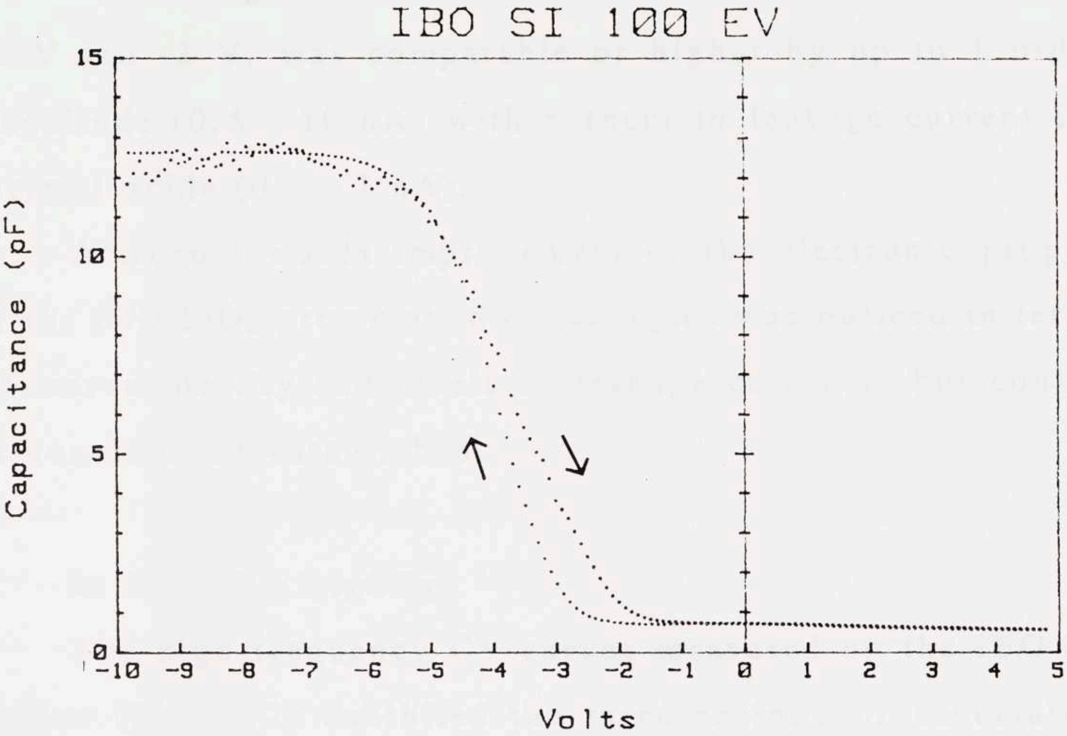

Figure 8.1. 1 MHz CV curve of 100 eV IBO SiO_2

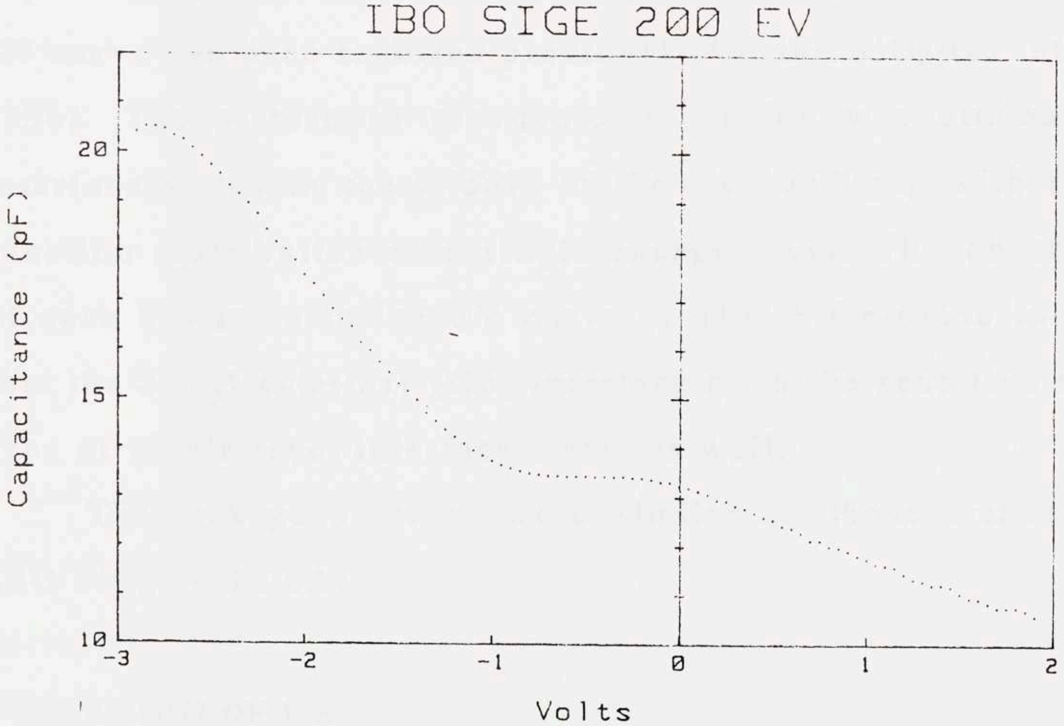

Figure 8.2. 400 kHz CV curve of 200 eV IBO SiGe-oxide

The leakage current in the IBO SiO_2 layers as measured at +2 V and -2 V, was comparable or higher by up to 1 order of magnitude (0.5 - 10 nA) with respect to leakage current in the thermal oxide (0.1 - 1 nA).

A trend towards improvement of the electronic properties of the IBO SiO_2 grown at lower energies was noticed in terms of CV curve ideality and levels of leakage currents, but could not be conclusively established.

b. IBO OF $SI_{1-X}GE_X$

The high frequency CV curves measured on the IBO SiGe-oxides (Fig. 8.2) exhibited the three regions of accumulation, depletion and inversion, but a plateau in the middle of the depletion region was also observed. This kind of double-plateau CV curve has been reported previously for the SiO_2/Ge interface [134]. The plateau in the depletion region was attributed to interface states in the middle of the Ge band gap with a delta function distribution at a single energy level. The observation of such a plateau in the CV curve of IBO SiGe-oxide indicates that the $Si_{1-y}Ge_yO_2/Si_{1-x}Ge_x$ interface might be sensitive to this type of single level interface states as well.

The leakage currents were similar to those measured in IBO SiO_2 (< 10 nA)

c. IBO OF GE

The IBO GeO_2 formed at 100 eV was also characterized. No CV curve could be observed and the leakage current was three orders of magnitude higher (1 - 10 μA) than for the IBO SiO_2

8.2. MOS TEST CIRCUIT

a. FABRICATION

Test circuits comprising MOS capacitors and MOS Field Effect Transistors (FET) of different geometries were also fabricated to assess the electrical characteristics of MOS devices having IBO oxides as gate material. The detailed process sequence of this modified 10 μm NMOS technology is given in the appendix A.3 with relevant observations and intermediate characterizations and only the most important features are presented here.

Three wafers were processed in parallel with three types of gate oxide:

- thermal oxide grown by dry oxidation at 900 °C for 10 min to serve as a reference for the circuit fabrication.
- IBO SiO_2 formed with 200 eV $^{18}O_2^+$ at 400 °C, capped by a 200 Å amorphous Si grown at 150 °C by MBE
- IBO $Si_{1-x}Ge_xO_2$ with 200 eV $^{18}O_2^+$ at room temperature, capped by a thin room temperature IBO SiO_2 and a 200 Å a-Si layer grown at 150 °C by MBE

The a-Si cap was deposited in order to protect the gate dielectric from atmospheric contamination until deposition of the polysilicon gate.

The circuit fabrication was specially designed in regard to the $Si_{1-x}Ge_x$ layers and their known thermal unstability [135].

High temperature steps above the MBE growth temperature of 500 °C were eliminated at the exception of the polysilicon gate deposition by LPCVD at 625 °C for a total time of 45 min. They were replaced either by using low temperature techniques such as deposition of the passivation oxide by low temperature CVD (400 °C, PYROX oxide), or by using rapid thermal processing such as RTA at 900 °C for 10 sec for dopant activation, recrystallization of the source and drain regions (S&D) and densification of the passivation oxide. The total thermal budget seen by the $Si_{1-x}Ge_x$ layer after MBE growth was thereby kept to a very small value. Relaxation of the strained layer, if any, can thus be expected to be minimum.

We did not encounter major problems during the processing of the circuits and the fabrication was in overall a success. The sheet resistivities of the S&D and of the polysilicon gate as well as the contact resistances were within the expected values (see appendix A.3).

b. ELECTRICAL CHARACTERIZATION OF THE MOS TEST CIRCUIT

Fig. 8.3 to 8.6 compare the characteristics of MOS capacitors (500x500 μm^2) and MOSFET's (W/L = 1) with the thermal oxide (≈ 70 Å) (figures a) and the IBO SiO_2 (≈ 40 Å) (figures b) as the gate oxide.

Fig. 8.3 show the CV curves measured at different frequencies. Although the individual curves look ideal with little hysteresis, there is a large frequency dependence of the capacitance at accumulation. Such a frequency dispersion is

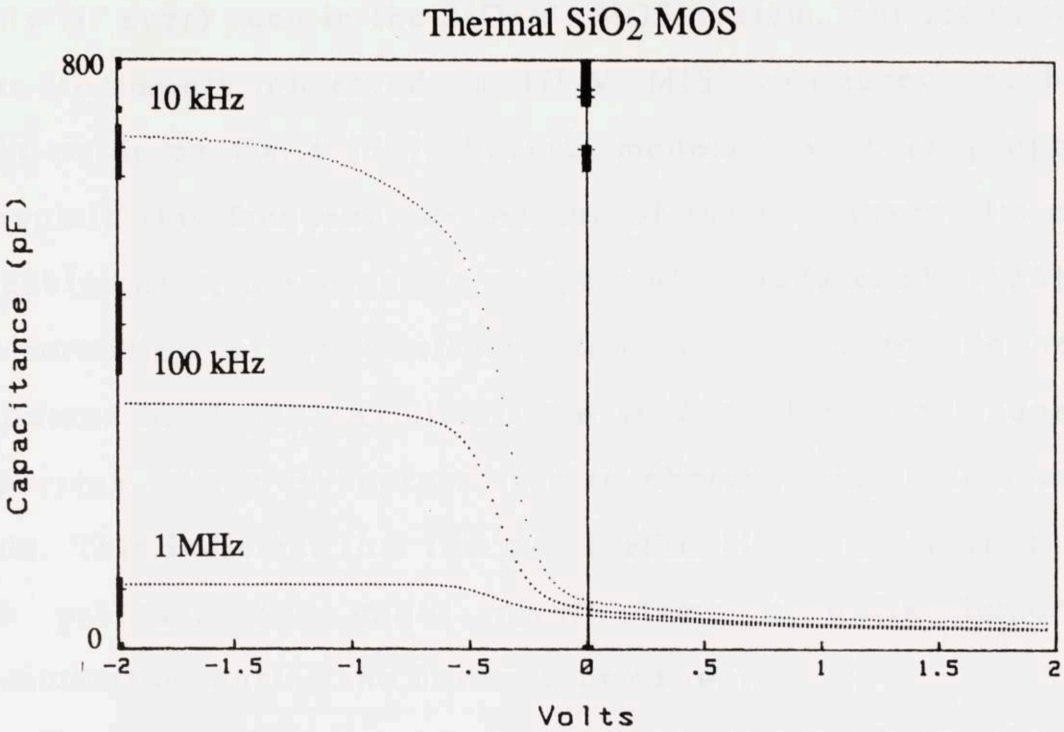

Figure 8.3a. CV curves at different frequencies for thermal SiO_2 MOS capacitor

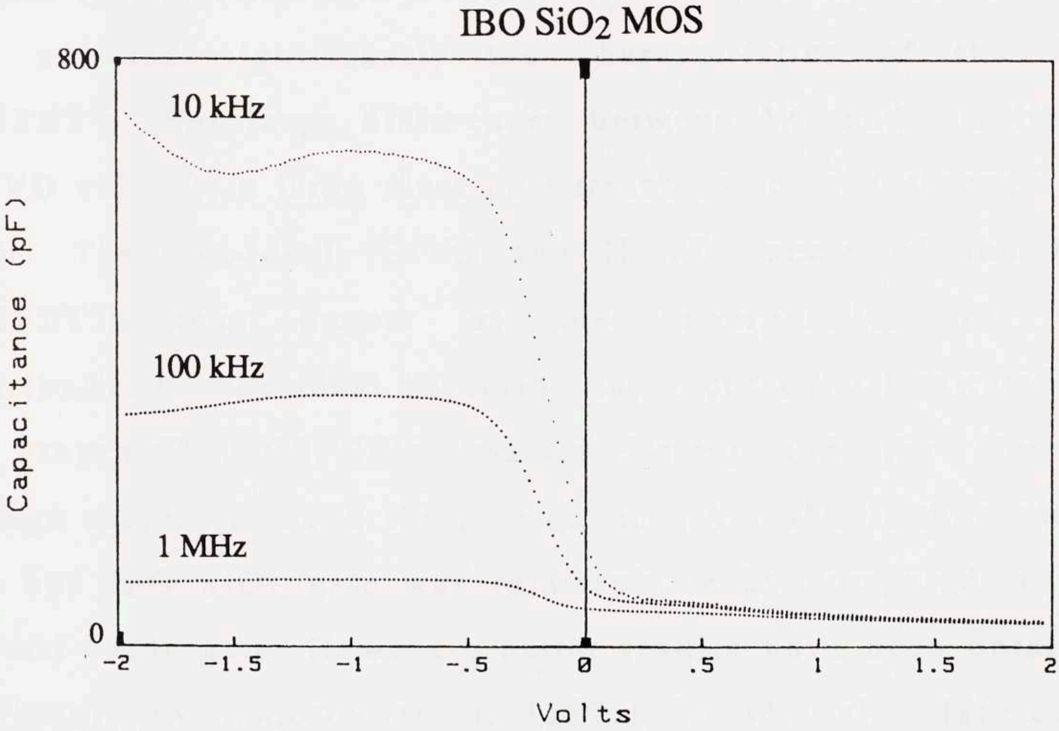

Figure 8.3b. CV curves at different frequencies for IBO SiO_2 MOS capacitor

rarely (if ever) seen in the SiO_2/Si MOS system, but seems to be quite commonly observed in III-V MIS structures, such as GaAs-oxide on GaAs [51]. Several models have been proposed to explain this frequency dispersion of the CV curves. Its most probable cause, based on the analysis of Sawada et al. [136], is the formation of an interface state mini-band in the semiconductor band gap. As illustrated in Fig. 8.3, the frequency dispersion of the CV curves is also observed with the thermal oxide. This indicates that this non ideality is not intrinsic to the IBO process, but might result from a quite important contamination during the device fabrication.

Despite the frequency dispersion observed in the CV curves, MOSFET operation could be obtained with both types of devices (thermal and IBO oxides). However, leakage through the gate affected significantly the characteristics of the IBO MOSFET's. For large differences between VG and VD (large VG-VD values), a large electron current could leak through the oxide. The non-ideal ID-VG and ID-VD curves of the IBO MOSFET's then appear as the superposition of two contributions: the ideal inversion layer current (illustrated by the "thermal" MOSFET's characteristics) and the electron leakage current through the gate at large VG-VD. It thus seems that our IBO SiO_2 gate was relatively leaky compared to the thermal oxide gate. However, better results have been obtained previously by Todorov et al. [137,138] who also fabricated MOSFET's with thin IBO SiO_2. Our relatively poor results are thus not entirely representative of the IBO oxide properties.

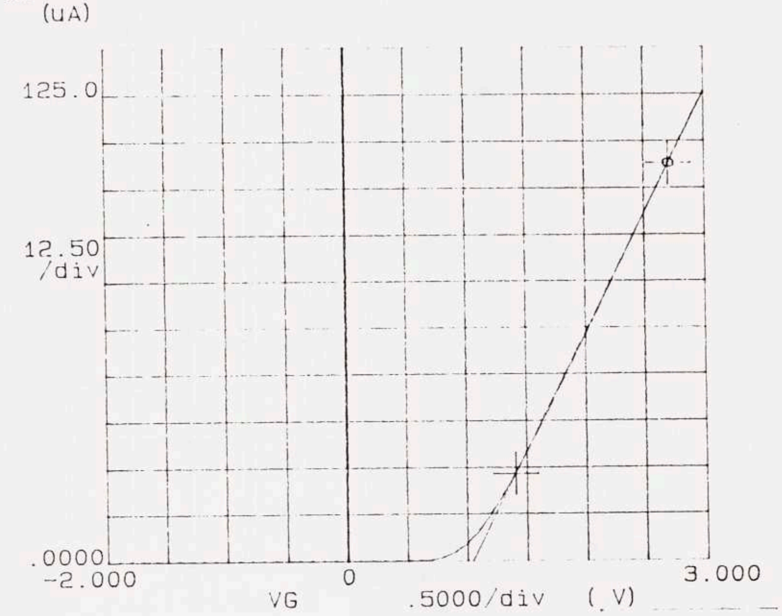

Figure 8.4a. ID-VG curve for thermal SiO_2 MOSFET's

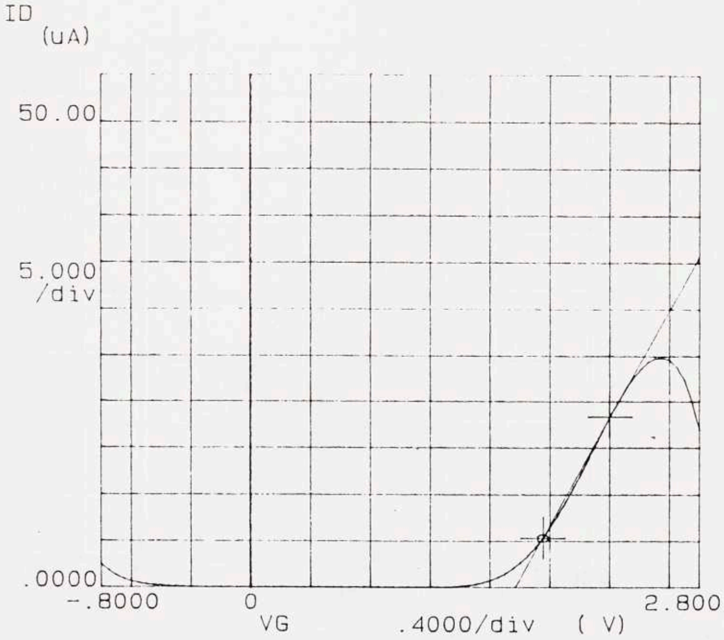

Figure 8.4b. ID-VG curve for IBO SiO_2 MOSFET's

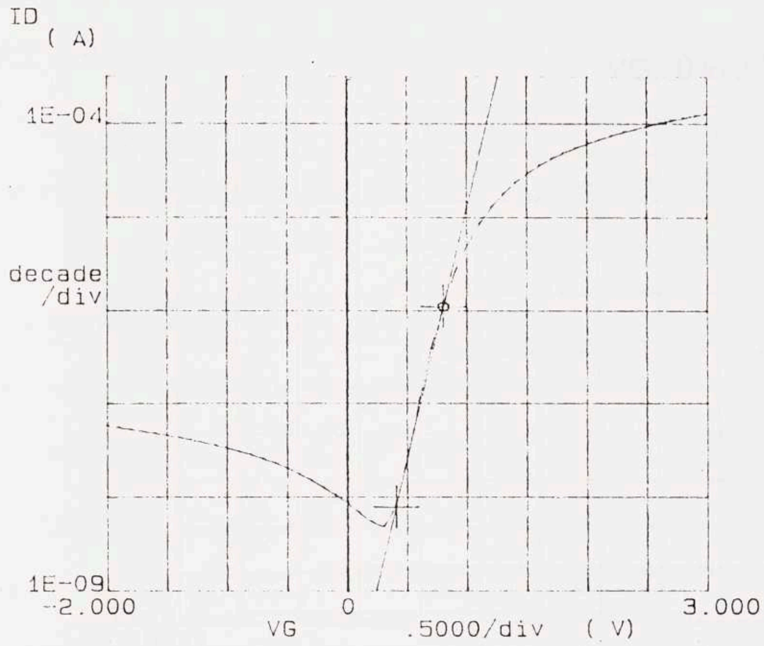

Figure 8.5a. Log(ID)-VG curve for thermal SiO_2 MOSFET's

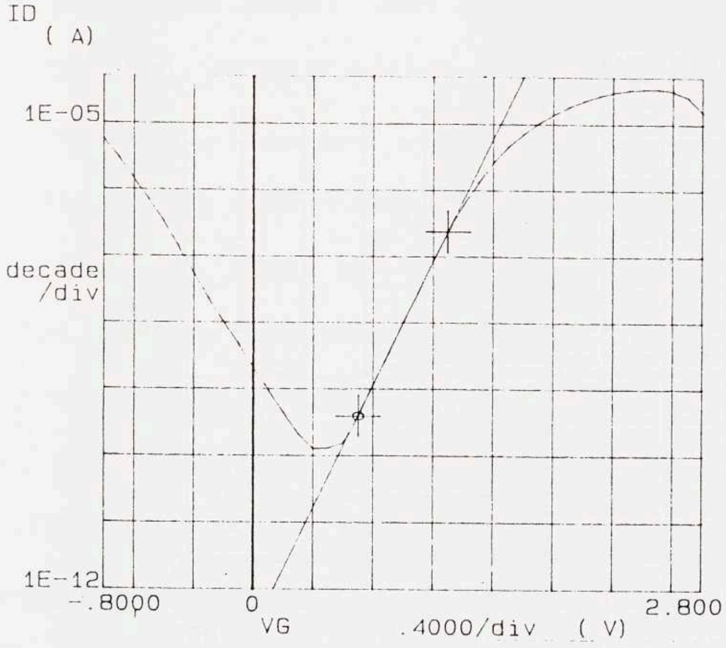

Figure 8.5b. Log(ID)-VG curve for IBO SiO_2 MOSFET's

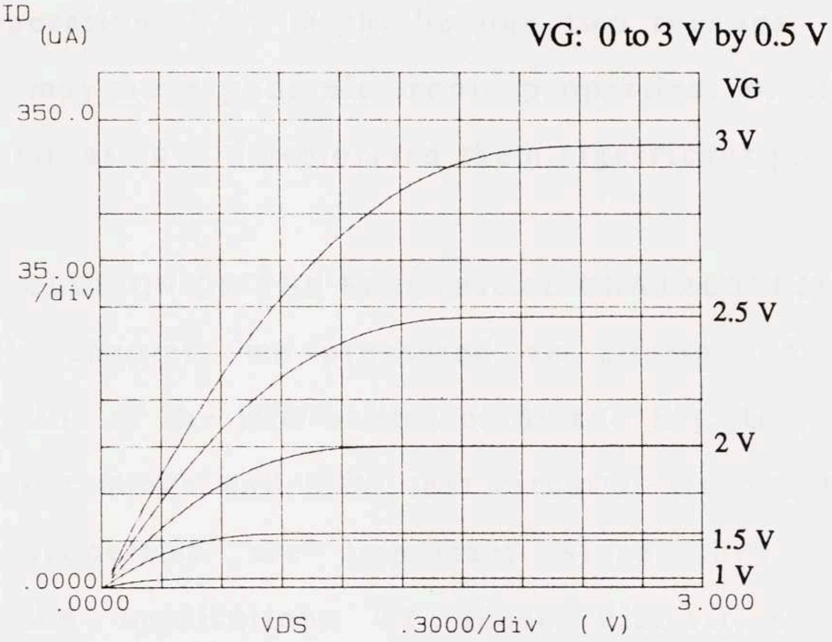

Figure 8.6a. ID-VD curves for thermal SiO_2 MOSFET's

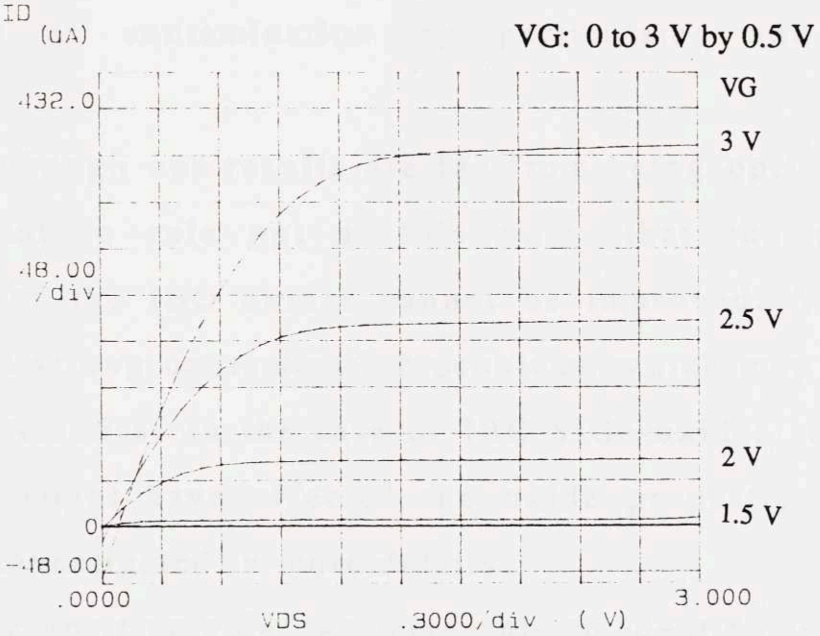

Figure 8.6b. ID-VD curves for IBO SiO_2 MOSFET's

In the case of the IBO SiGe circuit, the leakage through the gate oxide was too high and prevented any MOS and MOSFET operation. This might be due two reasons: the IBO SiGe-oxide may have poor electronic properties, or the device processing might have deteriorated them significantly.

8.3. CONCLUSION ON THE ELECTRICAL CHARACTERIZATION

In this chapter, we presented an attempt of electrical characterization of the IBO oxides of Si and $Si_{1-x}Ge_x$ using CV and IV measurements and MOS test circuits. On one hand, the electronic properties are important since they ultimately determine the applications of these dielectrics in MOS technologies. On the other hand, these electronic properties are the most sensitive properties not only to the characteristics of the IBO technique itself, but also to other issues extrinsic to IBO (such as contamination by particulates and metallic impurities).

Even though our results are far from being optimistic, we do not want to rule out at this point that the electronic properties of the IBO oxides cannot be improved. We indeed suffer from strong contamination problems which may mask the real characteristics. In the case of IBO SiGe-oxides, the device processing might have affected the oxide properties and this should be investigated in more details.

On the positive side, we were able to identify several non idealities affecting the MOS CV characteristics. Two of these non idealities, the plateau in the depletion region and the frequency dispersion of the CV curves, are quite uncommon to the SiO_2/Si MOS system, but are important to consider in other systems.

9. SUMMARY AND SUGGESTIONS FOR FUTURE WORK

Ion Beam Deposition (IBD) is a low temperature growth technique where a thin film is grown directly from a low energy ion beam (< 1 keV). The main advantage of IBD resides in its athermal nature which results from the modification of the growth kinetics induced by the ion-solid interaction. The rate-limiting steps in IBD are either athermal steps or steps with a low activation energy. This enables the growth of epitaxial films at lower temperatures than in Molecular Beam Epitaxy (MBE) or Chemical Vapor Deposition (CVD), and the formation of compound layers such as oxides at room temperature. In this work, several aspects of IBD growth of semiconductor-based epitaxial and oxide layers were investigated theoretically and experimentally.

A quantitative model DRIVIC was first developed to describe homodeposition by IBD and to account for experimental observations made for IBD epitaxial growth of Si on Si. DRIVIC takes into account the ion-solid interactions and the thermal diffusion and recombination of point defects during thin film growth by IBD. The simulation results for IBD of Si on Si show that the IBD growth mechanism is mediated by fast diffusing interstitials and establish an upper limit for the ion energy to achieve epitaxial growth by IBD, which depends on the point defect diffusivities. More specifically, the defect generation has to be confined in the subsurface region in order to favor interstitial recombination with the surface leading to net thin film growth, and vacancy annihilation to prevent amorphization. The effect of point defect diffusivities on the IBD growth process was investigated as well. We find that a model including mobile interstitials can account for various experimental observations specific to IBD growth. Monte-Carlo simulations of IBD of Si on Si were also conducted. They give an atomistic picture of the IBD epitaxial process which agrees with the predictions of the continuum model DRIVIC.

In the experimental part of this work, low energy Ion beam Oxidation (IBO) of Si, Ge, $Si_{1-x}Ge_x$ and GaAs at room temperature was investigated as a function of ion energy from 100 eV to 1 keV. We demonstrate for the first time the formation by IBO at room temperature of new SiGe-dioxide layers. The experimental results show a strong dependence on the ion energy of the materials properties such as phase formation, stoichiometry, film thickness and interface width. Low energies ($\leq$ 200 eV) are also found to be crucial for the formation by IBO of uniform and stoichiometric oxide layers.

To explore the kinetics of IBO and to account for the observed relationship between ion energy and films properties, computer models were developed for IBO of two-element targets, taking progressively into account oxygen incorporation and sputtering (model IS), ion beam mixing (model ISR), and oxygen diffusion and chemical reaction (model ISRD). The simulation results show that the model IS based only on implantation and sputtering cannot explain the thicknesses observed experimentally, but can give insight into the mechanism of phase formtion by IBO. Ion beam mixing effects introduced in the ISR model bring a first correction and are especially important to account for the spatial redistribution of the elements in compound targets, which results in a depth-dependent stoichiometry. The oxygen diffusion and the strong driving force for oxidation taken into account in the ISRD model are shown to be essential to describe accurately the experimental observations such as the three stages of IBO growth, the dependence of film thickness upon ion energy, and the formation of a sharp interface with the substrate.

We conclude our theoretical and experimental investigation of IBD with three comments of a more general character. Similarities between IBO of $Si_{1-x}Ge_x$ and GaAs are first pointed out and explained by the thermodynamic properties of the elemental and oxide phases involved, such as their respective sublimation energy, vapor pressures and stability. The observations made for Ion Beam Nitridation of Si, Ge, and $Si_{1-x}Ge_x$ [1] are then summarized and compared to IBO of the same materials. The differences between IBO and IBN can be explained by the difference in the relative importance of chemical reaction and diffusion in the thin film formation kinetics. Lastly, based on the theoretical computer modelling and the experimental observations, epitaxial growth by IBD and oxide layer formation by IBO are compared in terms of the role played by the point defect creation, diffusion and annihilation. We also stress on the importance of using low energies in both techniques in order to achieve the desired properties, epitaxy in IBD and uniformity and stoichiometry in IBO.

In the last chapter, the electrical properties of IBO Si- and SiGe-dioxide films were characterized. A preliminary MOS test circuit was also fabricated using the IBO films as the gate dielectric. The SiGe-based MOS structures are found to be sensitive to non-idealities uncommon to the SiO_2/Si system.

By our research, we attempted to gain insight into the kinetics of epitaxial growth and oxide formation by IBD. Although significant results were obtained both theoretically and experimentally and improved the understanding of the IBD thin film growth process, new questions have been raised and need to be addressed in future work.

For example, while studying the epitaxial growth by IBD using the DRIVIC model, we pointed out the possibility to obtain information on the point defect diffusivities by combining new IBD experiments and predictions by DRIVIC. Monte-Carlo simulations seem also worth to exploit further to understand the microscopic mechanisms and rate-limiting steps in epitaxial growth by IBD.

Our study of IBO could be continued by investigating different IBO processing conditions, such as lower ion energies (50 eV) and higher substrate temperatures, and/or IBO of other substrates, such as $Si_{1-x}Ge_x$ layers with higher Ge fractions and InP. The theoretical tools (models IS, ISR and ISRD) that we developed can be used to gain insight into these new IBO experiments.

We also started to investigate the technological applications of our research. New electronic devices based on heteroepitaxial $Si_{1-x}Ge_x$ strained layers are indeed the object of intense research. Further developments of MOS technologies based on $Si_{1-x}Ge_x$ layers rely on the ability to grow at low temperature SiGe-oxide films with good interfacial and dielectric properties. IBO could be the only technique to grow such SiGe MOS structures, but this needs to be proven.

We also introduced the concept of a new growth technique, Combined Ion and Molecular beam Deposition (CIMD). CIMD combines MBE and IBD in the same UHV chamber, offering unique possibilities in thin film growth at low temperatures and thereby a whole new research field. However, we already provided at least some experimental guidelines and theoretical tools, both for epitaxial growth (DRIVIC) and oxide formation (ISRD), that could be used in future CIMD investigations.

APPENDICES

A.1. ION BEAM CHARACTERIZATION

The ion beam was characterized for both ions (O_2^+ and N_2^+) using a home-built Faraday cup (FC). Besides the ion beam characterization, the FC assembly also allowed the calibration of the XPS with and the alignment of the three main components of the XPS system: the X-ray beam, the ion beam and the small analysis area (seen by the optical microscope). Fig. A.1 shows a mapping of the ion beam current density for a N_2^+ beam of 1.2 keV, rastered 50 %. The central region shows the relatively good uniformity of the current density when the beam is rastered. The ion beam current density was a strong function of the ionizer gas pressure (Fig. A.2a) and beam voltage (Fig. A.2b), and to a lesser degree of the emission current (Fig. A.2c). The focus was chosen so that the ion beam current density would be the most uniform when the beam was rastered. In the case of nitrogen, the beam was rather stable over time and significant beam density could be obtained. However, with oxygen, the gun was degrading steadily over time. Fig. A.2a also show that the optimum pressure was rather low for O_2^+, while it was well above 30 mPa for N_2 (not shown). This limited the O_2^+ current density and made quite difficult the operation with O_2^+ since this optimum pressure was not stable over the period of time of an IBO experiment. The ionizer gas pressure had to be constantly adjusted to avoid a sharp decrease in the ion beam current density. We tried to improve the performance of the ion gun by replacing the thoriated tungsten filament sensitive to oxidation by an iridium filament coated with thoria. Even though, the performances of the ion gun were degrading rather rapidly over time. At the next opening, we noticed that the ionizer assembly of the gun was completely corroded: the extraction plate was actually coated with an insulating layer, which could explain the low current density obtained. We therefore replaced the ionizer assembly but with no great improvment of the O_2^+ beam characteristics. We attribute this to a degradation of other parts of the ion gun optics. This gun is usually used with inert gases such as Ar and He. The specifications indicate that N_2^+ and O_2^+ can be used but we do not think that special care was taken in the design of the gun to work with such gases, at least not with O_2^+.

This actually brought a rather difficult problem in the quantification of the ion dose. The Faraday cup measurements were more useful for the N_2^+ beam than for the O_2^+ beam. However, the FC characterization helps better estimate the beam density even though it is not stable. The current at the target during IBD is actually the sum of 2 currents (Fig. A.2d): the ion beam current which can be measured by biasing the FC at -100 V, and a current of electron attracted to the sample when positively biased. This primary electron current reduces by about 40 % the measured ion beam current when the sample is biased at 1 kV during the IBO experiments.

The ion dose was estimated using the combination of the FC characteriazation and the measurement of the current during

IBO and of the area of the IBO spot. Still a significant error (≈ 30 %) on the ion dose can be expected.

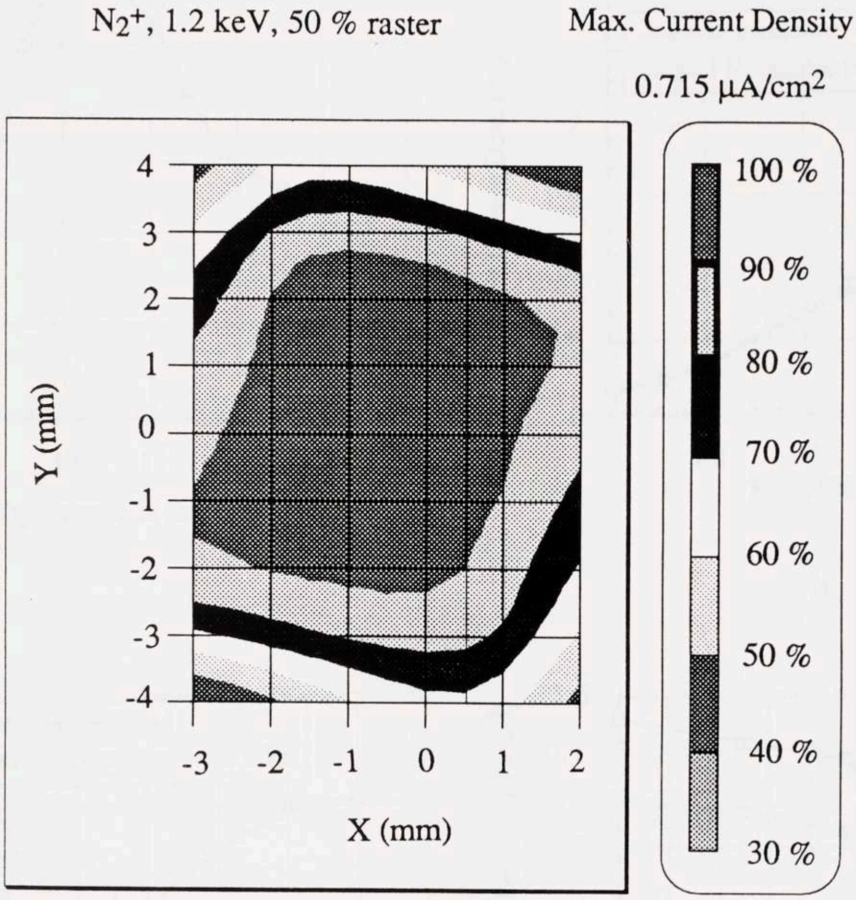

Figure A.1. Mapping of the ion beam current density at 1.2 keV, 50 % raster

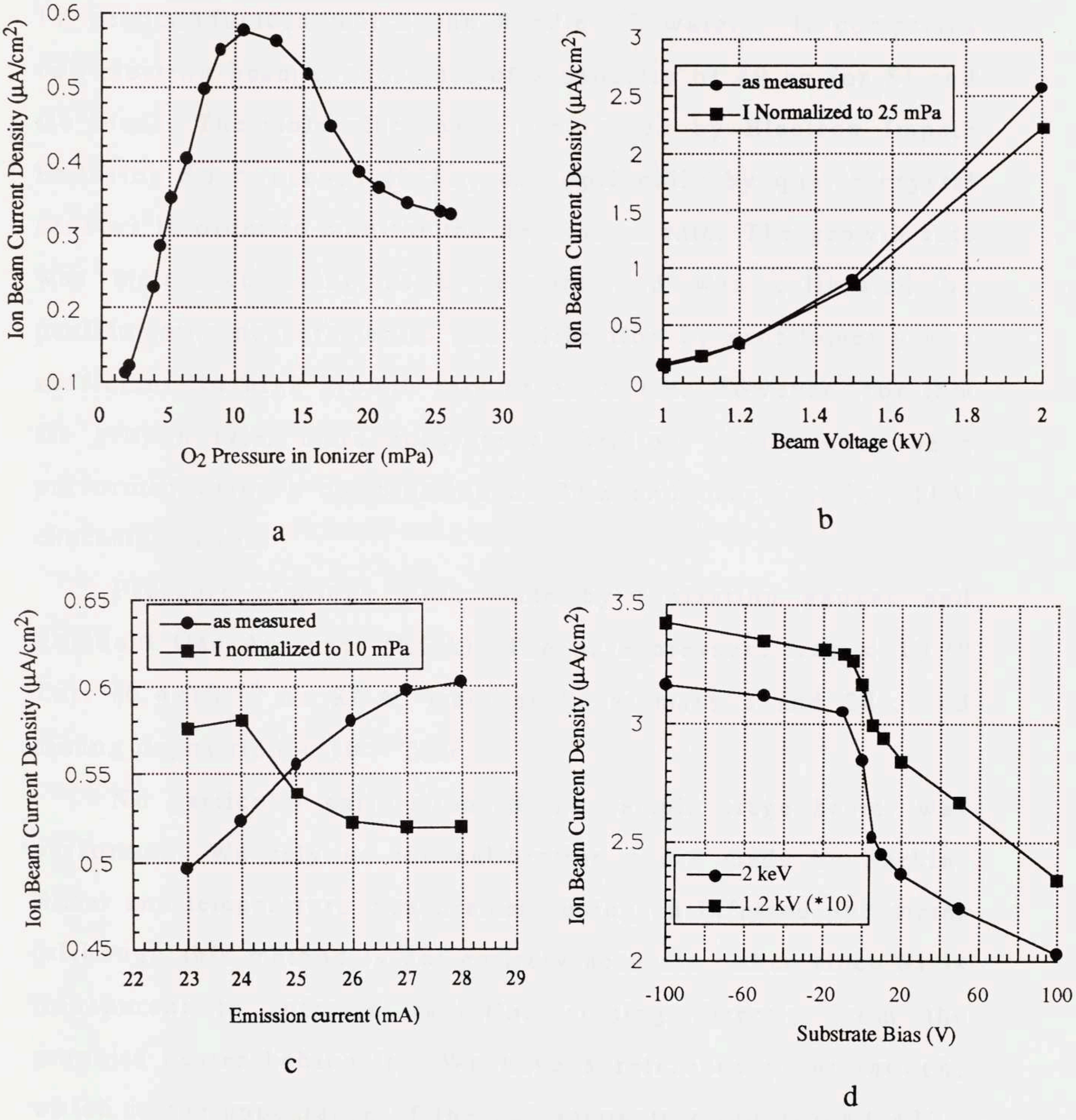

Figures A.2. $^{18}O_2^+$ ion beam characterization

A.2. MBE CALIBRATION

The growth chamber is an MBE system dedicated to group IV semiconductors which can handle 3” wafers. It comprises two electron-beam evaporators of a capacity of 40 cc for Si and Ge loads. The molecular beams are sensed by Electron Impact Emission Spectroscopy (EIES) and optionally by quartz crystal sensors in order to monitor the deposition rate. The growth rate was monitored using EIES sensors and was calibrated by profilometry measurements. The calibration by profilometry was sufficient for high growth rate of Si or Ge. However, for low Ge growth rate, more accurate calibration should have been performed using a combination of RBS and cross-section TEM characterization.

Pressure readings were made by ionization gauges and Residual Gas Analyzer (RGA). The base pressure was < 10^{-10} Torr (0.4×10^{-10} on RGA, main peaks at mass 2 and 28), and during deposition < 10^{-8} Torr.

No particular calibration of the sample stage heater was performed. We rely on the calibration curve made by Perkin-Elmer and temperature measurement using an infrared pyrometer (although this method is not entirely accurate either since Si is transparent to infrared radiation coming directly from the graphite heater behind it). We have a reference point though, which is the appearance of the 2x1 reconstruction around 430 - 450 °C at the same temperature reported by Grunthaner. This indicates that the temperature can be trusted within 30 °C.

The key point in MBE was to obtain a clean surface allowing epitaxy. RHEED was available as an in situ to verify the epitaxial nature of the deposited films. Once the 2x1 reconstruction could be observed on the starting Si wafer, epitaxial growth was obtained at high enough temperature. A buffer Si layer was usually grown first to provide a new template for the SiGe layers. (see RHEED pattern with second order spots) Si growth was performed at 600 °C while growth of the $Si_{1-x}Ge_x$ layers and Ge films were done at 500 °C. RHEED was used to check the crystallinity after growth.

During the characterization of the IBO/IBN samples, some of the samples grown in MBE were characterized by RBS and TEM. The crystalline quality of the layers was in general good, with few or no defects originating from the original surface. This indicates that the short cleaning was indeed sufficient to allow epitaxy. However, the thickness as measured by TEM and the composition of the $Si_{1-x}Ge_x$ layers as determined by RBS were significantly off the preset values, indicating that a more carefull and more frequent calibration of the MBE deposition rate is necessary.

A.3. IBO SIGE & IBO SI MOS PROCESS

Modified NMOS Technology (minimum feature size: 10 μm)

0. Si wafer, 2", p (100), 10 -15 Ω cm

1.A. MBE & IBO of SiGe

1.A.1. Cleaning: 2' Methanol, 15" HF in ethanol, 1' methanol, dry N_2

1.A.2. MBE deposit : Si buffer: 100 Å, 600 °C

$Si_{0.8}Ge_{0.2}$ film: 300 Å, 500 °C

1.A.3. IBO of $Si_{0.8}Ge_{0.2}$: R.T., 200 eV, estimated dose (XPS to check)

1.A.4. MBE deposit: 40 Å Si, 150 °C

1.A.5. IBO of Si cap: 500 eV 3 hr, 1 keV 1 hr (XPS to check)

1.A.6. MBE deposit of Si thin cap 200 Å, 150 °C

1.A.7. RCA clean

N.B.: IBO spot appeared + some inhomogeneities (≠ thicknesses)

1.B. IBO of Si

1.B.1. Cleaning: 2' Methanol, 15" HF in ethanol, 1' methanol, dry N_2

1.B.2. IBO of Si: 200 eV, 400 °C, estimated dose (XPS to check)

1.B.3. MBE deposit of Si thin cap 200 Å, 150 °C

1.B.4. RCA clean

N.B.: IBO spot appeared

1.C. Thermal oxide (reference)

1.C.1. RCA clean

1.C.2. Dry oxidation: 900 °C, 10 min.: 66 -68 Å SiO_2

2. Clean room processing (all wafers)

2.1. Gate deposit: LPCVD of polysilicon, 3000 Å

loading of the wafers
purge: 625 °C, 10 min
LPCVD deposit: 625 °C, 21 min, 0.4 Torr
purge: 625 °C, 10 min
unloading

N.B.: IBO spots pink

2.2. Implant # 1: gate, N-type, Arsenic, double implant:

$1\text{x}10^{15}$ ion/cm^2, 40 keV + $1\text{x}10^{15}$ ion/cm^2, 100 keV

Sheet resistivity after implant: $> 10^7\ \Omega/\square$

2.3. Photolithography # 1: Gate definition (NP mask)

Photolithography procedure includes:

- Dehydration bake: 30 min, 200 °C
- Coat wafer: 5000 RPM, 30 sec, positive photoresist
- Soft bake: 2 min, room temperature
  25 min, 90 °C
- Exposure: 406 nm, 2.5 sec
- Develop: 55 sec
- DI rinse and blow dry + inspection
- Hard bake: 25 min, 135 °C

2.4. Gate definition: plasma etch of polySi:

plasma etcher, SF_6, 100 mTorr, 100 W, 3.5 min

PolySi thickness measurement after RIE: 3200 - 3400 Å

+ photoresist strip: Piranha etch (H_2SO_4:H_2O_2, 3:1), 1 min

2.5. Photolithography # 2: Active region definition (ND mask)

N.B.: SiGe active region slightly misaligned

2.6. Implant # 2: source & drain region, N-type, Arsenic, double implant:

$1\text{x}10^{15}$ ion/cm^2, 40 keV + $1\text{x}10^{15}$ ion/cm^2, 100 keV

N.B.: PolySi above active region is implanted a second time

Junction Depth: 2200 Å from SUPREM 3

Sheet resistivity after implant: S & D Si: 320 $\Omega/\square$
PolySi: $> 10^7\ \Omega/\square$

2.7. Photoresist removal:

Piranha etch: 2 hr 30 min

Plasma etch: O_2, 100 mTorr, 100 W, 5 min

2.8. Passivation oxide deposit: Pyrox Oxide (undoped): 400 °C, 10 min

Ellipsometry after deposit: Nf = 1.4496, Tox = 4524 Å

2.9. Rapid Thermal Anneal (RTA): for dopant activation & densification of Pyrox
900 °C, 10 sec.
Sheet resistivity after RTA:
S & D Si: 60 - 62 Ω/□ (= 60.9 Ω/□ from SUPREM 3)
PolySi implanted once: 535 Ω/□ (527 Ω/□ after a second RTA 900°C, 10 sec)
PolySi implanted twice: 360 Ω/□
Ellipsometry after RTA: Nf = 1.4412, Tox = 4234 Å

2.10. Photolithography # 3: Contact openings (NC mask)

2.11. Contact opening: BOE etch, 5 min.
+ photoresist strip: Piranha etch, 1 min

2.12. Metallization: thermal evaporation of Al, room temperature, $< 2\ 10^{-6}$ Torr
Al thickness: 5900 - 7200 Å (ave: 6519 Å, stdev: 8.3 %)

2.13. Photolithography # 4: Metal definition (NM mask)
- dehydration: only 10 min, 90 °C
- exposure: 2.3 sec

2.14. Metal etch: PAN etch (phosphoric:acetic:nitric acid,), 6 -7 min
+ photoresist strip: organic stripper

2.15. Anneal & sintering by RTA: 350 °C, 10 sec
Contact resistance on thermal oxide wafer:
Before RTA: non linear and strongly resistive around 0 V: 4.2 kΩ
After RTA: linear, 18.2 - 29 Ω most of the wafer
(higher near the flat, up to 92 Ω)

BIBLIOGRAPHY

[1] O.C. Hellman, "Kinetics of Formation and Properties of Silicon and Silicon-Germanium Alloy Based Insulators Grown Using Low Energy Ion Beam Nitridation", Ph.D. Thesis, M.I.T. (1991)

[2] N. Herbots, O.C. Hellman, "Combined ion and molecular beam apparatus and method for depositing materials", U.S. patent # 4,800,100 (January 24, 1989)

[3] K. Miyake, T. Tokuyama, "Germanium and Silicon Ion Beam Deposition", Thin Solid Films **92**, 123 (1982)

[4] P.C. Zalm, L.J. Beckers, "Ion Beam Epitaxy of Silicon on Ge and Si at Temperature of 400 K", Appl. Phys. Lett. **41**, 168 (1982)

[5] N. Herbots, B.R. Appleton, T.S. Noggle, R.A. Zuhr, S.J. Pennycook, "Ion-Solid Interactions During Ion Beam Deposition of ^{74}Ge and ^{30}Si at Very Low Ion Energies (0-200 eV Range)", Nucl. Instrum. Meth. **B13**, 250 (1986)

[6] N. Herbots, B.R. Appleton, T.S. Noggle, S.J. Pennycook, R.A. Zuhr, D.M. Zehner, "Epitaxial Growth and Heterostructure Synthesis by Ion Beam Deposition (IBD)", in Semiconductor-Based Heterostructures: Interfacial Structure and Stability, ed. by M.L. Green, J.E.E. Baglin, G.Y. Chin, H.W. Deckman, W. Mayo, D. Narasinham, The Metallurgical Society, 335 (1986)

[7] N. Herbots, O.C. Hellman, P.A. Cullen, O. Vancauwenberghe, "Semiconductor-Based Heterostructure Formation Using Low Energy Ion Beams: Ion Beam Deposition (IBD) and Combined Ion and Molecular Beam Deposition (CIMD)", in Deposition and Growth: Limits for Microelectronics, ed. G.W. by Rubloff, American Vacuum Society Series **4**, 259 (1988)

[8] R.A. Zuhr, S.J. Pennycook, T.S. Noggle, N. Herbots, T.E. Haynes, B.R. Appleton, "Ion Beam Deposition in Materials Research", Nucl. Instrum. Meth. **B37/38**, 16 (1989)

[9] K.G. Orrman-Rossiter, A.H. Al-Bayati, D.G. Armour, S.E. Donnelly, J.A. van den Berg, "Ion Beam Deposited Epitaxial Thin Silicon Films", Nucl. Instrum. Meth.**B59/60**, 197 (1991)

[10] O. Tabata, S. Kimura, M. Kishimoto, M. Takahashi, A. Nomura, S. Suzuki, "Deceleration of Ion Beams for Film Deposition by an Electrostatic Field", Nucl. Instrum. Meth. **B37/38**, 906 (1989)

[11] T. Tokuyama, K. Yagi, K. Miyake, M. Tamura, N. Natsuaki, S. Tachi, "Low-Energy Mass-Separated Ion Beam Deposition of Materials", Nucl. Instrum. Meth. **182/183**, 241 (1981)

[12] R.A. Zuhr, D. Fathy, O.W. Holland, "Silicides Formed by Direct Ion Beam Deposition", in Processing and Characterization of Materials Using Ion Beams, ed. by L.E. Rehn, J.E. Greene, F.A. Smidt, Mat. Res. Soc. Symp. Proc. vol. **128**, 119 (1989)

[13] T.E. Haynes, R.A. Zuhr, S.J. Pennycook, "Heteroepitaxy of GaAs on Silicon and Germanium by Low-Energy Ion Beam Deposition Using Alternating Beams", in Advances in Materials, Processing and Devices in III-V Compound Semiconductors, ed. by D.K. Sadana, L. Eastman, R. Dupuis, Mat. Res. Soc. Symp. Proc. vol. **144**, 311 (1989)

[14] S. Tamura, M. Hyouzho, K. Yokota, S. Katayama, "Growth of Crystalline GaAs Films on Si Substrates by Ga and As Ion Beams", Nucl. Instrum. Meth. **B37/38**, 862 (1989)

[15] S. Aisenberg, R. Chabot, "Ion-Beam Deposition of Thin Films of Diamond-like Carbon", J. Appl. Phys. **42**, 2953 (1971)

[16] E.G. Spencer, P.H. Schmidt, D.C. Joy, F.J. Sansalone, "Ion-Beam-Deposited Polycrystalline diamond-like Films", Appl. Phys. Lett. **29**, 118 (1976)

[17] E.F. Chaikovskii, V.M. Puzikov, A.V. Semenov, "Deposition of Diamond Films from Beams of Carbon Ions", Sov. Phys. Crystallogr. **26**, 122 (1981)

[18] J.H. Freeman, W. Temple, G.A. Gard, "The Epitaxial Synthesis of Diamond by the Deposition of Low Energy Carbon Ions", Vacuum **34**, 305 (1984)

[19] T. Miyazawa, S. Misawa, S. Yoshida, S. Gonda, "Preparation and Structure of Carbon Film Deposited by a Mass-Separated C^+ Ion Beam", J. Appl. Phys. **55**, 188 (1984)

[20] J. Ishikawa, Y. Takeiri, T. Takagi, "Mass-Separated Negative-Ion-Beam Deposition System", Rev. Sci. Instrum. **57**, 1512 (1986)

[21] J.L. Robertson, S.C. Moss, Y. Lifshitz, S.R. Kasi, J.W. Rabalais, G.D. Lempert, E. Rapoport, "Epitaxial Growth of Diamond Films on Si(111) at Room Temperature by Mass-Selected Low-Energy C^+ Beams", Science, 1047 (February 24, 1989). Disclaim in ref. [22]

[22] J.L. Robertson, S.C. Moss, Y. Lifshitz, S.R. Kasi, J.W. Rabalais, G.D. Lempert, E. Rapoport, "Epitaxial Growth of Diamond Films on Si(111) by Mass-Selected Low-Energy C^+ Beams", Paper withdrawn from the 1989 Materials Research Society Spring Meeting, Symposium H & Q (H1.2/Q1.2), April 24-29, 1989, San Diego, CA

[23] N. Herbots, "Silicon and Germanium Oxide Formation by Ion Beam Deposition (IBD)", paper presented at the 1988 Materials Research Society Spring Meeting, Symposium on Advanced Surface Processes for Optoelectronics , April 4-8, 1988, Reno, NV

[24] S.S. Todorov, E.R. Fossum, "Room Temperature Growth of Silicon Dioxide Using a Low Energy Ion Beam", in Photon, Beam and Plasma Stimulated Chemical Processes at Surfaces, ed. by V.M. Donnelly, I.P. Herman, M. Hirose, Mat. Res. Soc. Symp. Proc. vol. **75**, 349 (1987)

[25] S.S. Todorov, C.F. Yu, E.R. Fossum, "Direct formation of dielectric thin film on silicon by low energy ion beam bombardment", Vacuum **36**, 929 (1986)

[26] O. Vancauwenberghe, present work

[27] O. Vancauwenberghe, O.C. Hellman, N. Herbots, "New SiGe Dielectric Grown at Room Temperature by Low Energy Ion Beam Oxidation and Nitridation", Appl. Phys. Lett., October 21, 1991 (in press)

[28] O. Vancauwenberghe, N. Herbots, H. Manoharan, M. Ahrens, "Ion beam oxidation of GaAs: The role of ion energy", J. Vac. Sci. Technol. **A9**, 1035 (1991)

[29] J.A.Taylor, G.M. Lancaster, A. Ignatiev, J.W. Rabalais, "Interactions of ion beams with surfaces. Reactions of nitrogen with silicon and its oxides", J. Chem. Phys. **68**, 1776 (1978)

[30] J.A.Taylor, G.M. Lancaster, J.W. Rabalais, "Chemical reactions of N_2^+ ion beams with group IV elements and their oxides", J. Electron Spectro. Rel. Pheno. **13**, 435 (1978)

[31] R. Hezel, N. Lieske, "Room temperature formation of Si-nitride films by low energy nitrogen ion implantation into silicon", J. Electrochem. Soc. **129**, 379 (1982)

[32] W.M. Lau, "Ion bombardment effects on GaAs using 100 eV nitrogen ions", in Processing and Characterization of Materials Using Ion Beams, ed. by L.E. Rehn, J.E. Greene, F.A. Smidt, Mat. Res. Soc. Symp. Proc. vol. **128**, 695 (1989)

[33] G.H. Takaoka, K. Matsugatani, J. Ishikawa, T. Takagi, "Silicon nitride and oxide film formation by the simultaneous use of a microwave ion source and an ICB system", Nucl. Instrum. Meth. **B37/38**, 783 (1989)

[34] R.P. Netterfield, P.J. Martin, W.G. Sainty, "Synthesis of silicon nitride and silicon oxide films by ion-assisted deposition", Applied Optics **25**, 3808 (1986)

[35] K.S. Grabowski, A.D.F. Kahn, E.P. Donovan, C.A. Carosella, "Thermal stability of silicon nitride coatings produced by ion assisted deposition", Nucl. Instrum. Meth. **B39**, 190 (1989)

[36] H. Ito, Y. Minowa, "Dual ion beam deposition of oxide, nitride, and carbide films", J. Vac. Sci. Technol. **B7**, 1963 (1989)

[37] T. Tsukizoe, T. Nakai, N. Ohmae, "Ion-Beam Plating Using Mass-Analyzed Ions", J. Appl. Phys. **48**, 4770 (1977)

[38] J.S. Colligon, W.A. Grant, J.S. Williams, R.P.W. Lawson, "Deposition of Thin Films by Retardation of an Isotope Separator Beam", in Applications of Ion Beams to Materials 1975, Proceedings of the Institute of Physics Conference Series **28**, 357 (1976)

[39] J. Amano, "Direct Ion Beam Deposition for Thin Film Formation", Thin Solid Films **92**, 115 (1982)

[40] I. Yamada, H. Inokawa, T. Takagi, "Film Deposition and Buried Layer Formation by Mass-Analyzed Ion Beams", Nucl. Instrum. Meth. **B6**, 439 (1985)

[41] T.S. Noggle, B.R. Appleton, N. Herbots, R.A. Zuhr, "Epitaxial Growth of ^{57}Fe Films on Silver by Ion Beam Deposition", Paper presented at the March Meeting of the American Physical Society, March 31 - April 4, 1986, Las Vegas, NV, Bulletin of the American Physical Society (1986)

[42] J. Ahn, R.P.W. Lawson, K.M. Yoo, K.A. Stromsmoe, M.J. Brett, "Deposition of Metastable Binary Alloy Thin Films Using Sequential Ion Beams from a Single Ion Source", Nucl. Instrum. Meth. **B17**, 37 (1986)

[43] D.G. Armour, "Ion Beam Deposition: Damage and Epitaxy", in Fundamentals of Beam-Solid Interactions and Transient Thermal Processing, ed. by M.J. Aziz, L.E. Rhen, B. Stritzker, Mat. Res. Soc. Symp. Proc. vol. **100**, 127 (1988)

[44] D.G. Armour, P. Bailey, G. Sharples, "The Use of Ion Beams in Thin Film Deposition", Vacuum **36**, 769 (1986)

[45] J.M.E. Harper, M. Heiblum, J.L. Speidell, J.J. Cuomo, "Ion Beam Oxidation", J. Appl. Phys. **52**, 4118 (1981)

[46] Y. Yoshida, T. Ohnishi, Y. Hirofuji, H. Iwasaki, T. Ikeda, "Low-Energy Double-Ion-Beam Deposition System", Jpn. J. Appl. Phys. **27**, 140 (1988)

[47] Y. Yoshida, T. Ohnishi, T. Sekihara, Y. Hirofuji, "Low-Energy Double Ion-Beam Deposition of Compound Films", Nucl. Instrum. Meth. **B37/38**, 866 (1989)

[48] W. Reuter, "A SIMS-XPS study on silicon and germanium under O_2^+ bombardment", Nucl. Instrum. Meth. **B15**, 173 (1986)

[49] Y. Lifshitz, S.R. Kasi, J.W. Rabalais, "Subplantation Model for Film Growth from Hyperthermal Species: Application to Diamond", Phys. Rev. Lett. **62**, 1290 (1989)

[50] D.J. Eaglesham, H.J. Gossman, M. Cerullo, "Limiting thickness h_{epi} for epitaxial growth and room temperature Si growth on Si (100)", Phys. Rev. Lett. **65**, 1227 (1990)

[51] W.F. Croydon, E.H.C.Parker, Dielectric films on GaAs, (Gordon and Breach, New York, 1981)

[52] Physics and Chemistry of III-V Compound Semiconductor Interfaces, ed. by Wilmsen C.W. (Plenum Press, 1985)

[53] J.T. Law, P.S. Meigs, "Rates of oxidation of Germanium", J. Electrochem. Soc. **104**, 155 (1957)

[54] F.K. LeGoues, R. Rosenberg, and B.S. Meyerson, "Kinetics and mechanism of oxidation of SiGe: dry versus wet oxidation", Appl. Phys. Lett. **54**, 644 (1989)

[55] P.L.F. Hemment, "Internal oxidation of Si by Ion Beam Synthesis", in Properties of Si, ed. by INSPEC, 710 (1988)

[56] see for example: Ion Beam Assisted Film Growth, ed. by T. Itoh (Elsevier, Amsterdam, 1989)

[57] The Technology and Physics of Molecular Beam Epitaxy, ed. by E.H.C. Parker (Plenum Press, 1985)

[58] Molecular Beam Epitaxy and Heterostructures, ed. by L.L. Chang, K. Ploog, NATO ASI Series, Series E: Applied Sciences **87** (Nijhorf, 1985)

[59] J.C. Bean, "Growth of Doped Silicon Layers by Molecular Beam Epitaxy", in Impurity Doping Processes in Silicon, ed. by F.F.Y. Wang (North-Holland, 1981), Chapter 4

[60] S.S.Iyer, "Silicon Molecular Beam Epitaxy", in Epitaxial Silicon Technology, ed. by B.J. Baliga (Academic Press, 1986), Chapter 2

[61] Emerging Technologies for In-Situ Processing, ed. by D.J. Ehrlich, V.T. Nguyen, NATO ASI Series, Series E: Applied Sciences **139** (Nijhorf, 1987)

[62] T. Itoh, T. Nakamura, M. Muromachi, T. Sugiyama, "Low Temperature Silicon Epitaxy by Partially Ionized Vapor Deposition", Jpn. J. Appl. Phys. **16**, 553 (1977)

[63] S. Shimizu, S. Komiya, "Epitaxial Growth of Si on (1012) Al_2O_3 by Partially Ionized Vapor Deposition", J. Vac. Sci. Technol. **17**, 489 (1980)

[64] H. Gotoh, T. Suga, H. Suzuki, M. Kimata, "Low Temperature Growth of Gallium Nitride", Jpn. J. Appl. Phys. **20**, L545 (1981)

[65] Y.Ota, "Silicon Molecular Beam Epitaxy with Simultaneous Ion Implant Doping", J. Appl. Phys. **51**, 1102 (1980)

[66] R.G. Swartz, J.H. McFee, A.M. Voshchenkov, S.N. Finegan, Y. Ota, "A Technique for Rapidly Alternating Boron and Arsenic Doping in Ion-Implanted Silicon Molecular Beam Epitaxy", Appl. Phys. Lett. **40**, 239 (1982)

[67] H. Sugiura, "Silicon Molecular Beam Epitaxy with Antimony Ion Doping", J. Appl. Phys. **51**, 2630 (1980)

[68] J.C. Bean, "Silicon Molecular Beam Epitaxy: Highlights of Recent Work", J. Electronic Materials **19**, 1055 (1990)

[69] K. Moriwaki, Y. Enomoto, S. Kubo, T. Murakami, "As-Deposited Superconducting $Ba_2YCu_3O_{7-y}$ Films Using ECR Ion Beam Oxidation", Jpn. J. Appl. Phys. **27**, L2075 (1988)

[70] D. Pavuna, B.J. Kellett, B. Dwir, J.H. James, A. Gauzzi, J. Faulkner, M. Affonte, F.K. Reinhart, "Ion beam codeposition of HTSC films on $SrTiO_3$ and

ITO/Si", in Growth of Semiconductor Structures and High-Tc Thin Films on Semiconductors, ed. by A. Madhukar, SPIE Proc. **1285**, 248 (1990)

[71] S. Shimizu, O. Tsukakoshi, S. Komiya, Y. Makita, "A Molecular and Ion-Beam Epitaxy System for the Growth of III-V Compound Semiconductors Using a Mass-Separated, Low-Energy Group-V Ion Beam", Jpn. J. Appl. Phys. **24**, 1130 (1985)

[72] S. Shimizu, O. Tsukakoshi, S. Komiya, Y. Makita, "Molecular Beam Epitaxy of GaAs Using a Mass-Separated, Low-Energy As^+ Ion Beam", J. Vac. Sci. Technol. **B3**, 554 (1985)

[73] S. Maruno, Y. Morishita, T. Isu, Y. Nomura, H. Ogata, "Molecular Beam Epitaxy of InP Using Low-Energy P^+ Ion Beam", J. Crystal Growth **81**, 338 (1987)

[74] Y. Morishita, S. Maruno, T. Isu, Y. Nomura, H. Ogata, "Electrical and Optical Properties of InP Grown by MBE Using P^+ Ion Beam", J. Crystal Growth **88**, 215 (1988)

[75] O.W. Holland, C.W. White, and D. Fathy, "Novel oxidation process in Ge^+-implanted Si and its effect on oxidation kinetics", Appl. Phys. Lett. **51**, 520 (1987)

[76] W.S. Liu, G. Bai, M-A. Nicolet, C.H. Chern, V. Arbet and K.L. Wang, "Oxidation of Ge_xSi_{1-x}", to be published in Silicon Molecular Beam Epitaxy, ed. by J.C. Bean, E.H.C. Parker, S.S. Iyer, Y. Shiraki, E. Kasper, K. Wang, Mater. Res. Soc. Proc. Vol. **220** (1991)

[77] R. People, "Physics and Application of Ge_xSi_{1-x}/Si Strained-Layer Heterostructures", IEEE J. Quantum Electronics **QE-22**, 1696 (1986)

[78] K.R. Hoffmann, "Charge control in SiGe quantum-well MOSFET's and MODFET's", to be published in Silicon Molecular Beam Epitaxy, ed. by J.C. Bean, E.H.C. Parker, S.S. Iyer, Y. Shiraki, E. Kasper, K. Wang, Mater. Res. Soc. Proc. Vol. **220** (1991)

[79] C.D. Thurmond, G.P. Schwartz, G.W. Kammlott, B. Schwartz, "GaAs oxidation and the Ga-As-O equilibrium phase diagram", J. Electrochem. Soc., **127**, 1366, (1980)

[80] J.A. Van Vechten, "A simple man's view of the thermochemistry of semiconductors", in Handbook of Semiconductors Vol. 3, ed. by S.P. Deller, (North Holland, New York, 1980)

[81] U. Landman, W.D. Luedtke, M.W. Ribarsky, "Structural and dynamical consequences of interactions in interfacial systems", J. Vac. Sci. Technol. **A7**, 2829 (1989)

[82] J.P. Biersack, W. Eckstein, "Sputtering Studies with the Monte-Carlo Program TRIM.SP", Appl. Phys. **A34**, 73 (1984)

[83] J.P. Biersack, L.G. Haggmark, "A Monte-Carlo Computer Program for the Transport of Energetic Ions in Amorphous Targets", Nucl. Instrum. Meth. **174**, 257 (1980)

[84] J.F. Ziegler, J.P. Biersack, U. Littmark, The Stopping and Range of Ions in Solids (Pergamon Press, New York, 1985)

[85] B.W. Dodson, "Atomistic Simulations of Silicon Beam Deposition", Physical Review **B36**, 1068 (1987)

[86] B.W. Dodson, "Atomistic simulations of low energy beam deposition", in Fundamentals of Beam-Solid Interactions and Transient Thermal Processing, ed. by M.J. Aziz, L.E. Rhen, B. Stritzker, Mat. Res. Soc. Symp. Proc. Vol. **100**, 139 (1988)

[87] B.W. Dodson, "Atomic scale modeling of low energy ion-solid processes", in Processing and Characterization of Materials Using Ion Beams, ed. by L.E. Rehn, J.E. Greene, F.A. Smidt, Mat. Res. Soc. Symp. Proc. vol. **128**, 137 (1989)

[88] B.J. Garrison, M.T. Miller, D.W. Brenner, "Kinetic Energy Enhanced Molecular Beam Epitaxial Growth on Si (100)", in Atomic Scale Calculations in Materials Science, ed. J. Tersoff, D. Vanderbilt, V. Vitek, Mat. Res. Soc. Symp. Proc., vol. **141**, 419 (1989)

[89] A. Tenner, Rainbow Scattering, Ph.D. Thesis, FOM-Instituut, Amsterdam (1986)

[90] P.S. Chou, N.M. Ghoniem, "Application of the Monte-Carlo code TRIPOS to surface and bulk ion-transport problems", Nucl. Instrum. Meth. **B28**, 175 (1987)

[91] N. Laegreid, G.K. Wehner, "Sputtering yields of metals for Ar+ and Ne+ ions with energies from 50 to 600 eV", J. Appl. Phys. **32**, 365 (1961)

[92] A.L. Southern, W.R. Willis, M.T. Robinson, "Sputtering experiments with 1 to 5 keV Ar^+ ions", J. Appl. Phys. **34**, 153 (1963)

[93] T.R. Waite, "Theoretical Treatment of the Kinetics of Diffusion-Limited Reactions", Phys. Rev. **107**, 463 (1957)

[94] D.A. Antoniadis, I. Moskowitz, "Diffusion of Substitutional Impurities in Silicon at Short Oxidation Times: An Insight into Point Defect Kinetics", J. Appl. Phys. **53**, 6788 (1982)

[95] U. Gösele, W. Frank, A. Seeger, "An Entropy Barrier Against Vacancy-Interstitial Recombination in Silicon", Solid State Communication **45**, 31 (1983)

[96] D. Mathiot, J.C. Pfister, "Diffusion Mechanisms and Non-equilibrium Defects in Silicon", in Impurity Diffusion and Gettering in Silicon, ed. by R.B. Fair, C.W. Pearce, J. Washburn , Mat. Res. Soc. Symp. Proc. vol. **36**, 117 (1985)

[97] S. Mottet , A. Roizes, "Defect Formation Kinetics in Irradiated Silicon at 300 K", in Defects and Radiation Effects in Semiconductors 1978, The Institute of Physics Conference Series **46**, 281 (1979)

[98] T.Y. Tan, U. Gösele, "Point defects, Diffusion Processes, and Swirl Defect Formation in Silicon", Applied Physics **A37**, 1 (1985)

[99] S.T. Pantelides, "Atomic Diffusion in Silicon: What Theory Hath Wrought", in Proceedings of the Thirteenth International Conference on Defects in Semiconductors (ICDS '84), ed. by L.C. Kimerling, J.M. Parsey Jr., The Metallurgical Society of AIME, 151 (1985)

[100] C.P. Flynn, Point Defects and Diffusion (Clarendon Press, Oxford, 1972)

[101] H.J. Rath, J. Reffle, D. Huber, P. Eichinger, F. Iberl, H. Bernt, "Characterization of denuded zones in silicon wafers", in Impurity Diffusion and Gettering in Silicon, ed. by R.B. Fair, C.W. Pearce, J. Washburn , Mat. Res. Soc. Symp. Proc. vol. **36**, 193 (1985)

[102] P. Sigmund, "Sputtering by ion bombardment: Theoretical concepts", in Sputtering by Particle Bombardment I: Physical Sputtering of Single-Element Solids, ed. by R. Behrisch, Topics in Applied Physics **47** (Springer Verlag, Berlin, 1981), Chapter 2

[103] R. Kelly, "Thermal effects in sputtering", Surface Science **90**, 280 (1979)

[104] Y. Limoge, J.L. Bocquet, "Monte-Carlo simulation in diffusion studies: time scale problems", Acta Metall. **36**, 1717 (1988)

[105] J.W. Corbett, J.P. Karins, T.Y. Tan, "Ion-induced defects in semiconductors", Nucl. Instrum. Meth. **182/183**, 457 (1981)

[106] U. Schmid, N.C. Myers, J.A. Van Vechten, "VISDIM: A Monte-Carlo program for the simulation of atomic diffusion in diamond and zinc-blende structures", Computer Physics Communications **58**, 329 (1990)

[107] M. Kitabatake, P. Fons, J.E. Greene, "Molecular dynamics and quasidynamics simulations of the annealing of bulk and near-surface interstitials formed in molecular beam epitaxial Si due to low energy particle bombardment during deposition", J. Vac. Sci. Technol. **A9**, 91 (1991)

[108] A. Rockett, "Monte-Carlo simulations of the growth of diamond-structure semiconductors and surface reflected electron-beam intensities during molecular beam epitaxy", J. Vac. Sci. Technol. **B6**, 763 (1988)

[109] S.A. Barnett, A. Rockett, "Monte Carlo simulations of Si(001) growth and reconstruction during molecular beam epitaxy", Surface Science **198**, 133 (1988)

[110] E. Chason, B.W. Dodson, "Effect of step edge transition rates and anisotropy in simulations of epitaxial growth", to be published in J. Vac. Sci. Technol. (1991)

[111] B.J. Garrison, "Molecular dynamics simulations of reactions at silicon surfaces", to be published in J. Vac. Sci. Technol., (1991)

[112] M. Kitabatake, J.E. Greene, "Simulations of low energy ion/surface interaction effects during epitaxial film growth", to be published in Low Energy Ion Beam and Plasma Modification of Materials, ed. by J.M.E. Harper, K. Miyake, J.R. McNeil, S.M. Gorbatkin, Mat. Res. Soc. Symp. Proc. Vol. **223** (1992)

[113] see for example Silicon Molecular Beam Epitaxy, ed. by J.C. Bean, L.J. Schowalter, The Electrochemical Society vol **88-8** (1988)

[114] A. Ishizaka, Y. Shiraki, "Low temperature surface cleaning of Silicon and its application to Silicon MBE", J. Electrochem. Soc. **133**, 666 (1986)

[115] P.J. Grunthaner, F.J. Grunthaner, R.W. Fathauer, T.L. Lin, M.H. Hecht, L.D. Bell, W.J. Kaiser, F.D. Schowengerdt, J.H. Mazur, "Hydrogen-terminated Silicon substrates for low temperature Molecular Beam Epitaxy", Thin Solid Films **183**, 197 (1989) and references therein

[116] P.J. Grunthaner, F.J. Grunthaner, R.W. Fathauer, T.L. Lin, F.D. Schowengerdt, B. Pate, J.H. Mazur, "Low temperature substrate cleaning technology for Si MBE", in Silicon Molecular Beam Epitaxy, ed. by J.C. Bean, L.J. Schowalter, The Electrochemical Society vol **88-8**, 375 (1988)

[117] M.P. Seah, "Quantification of AES and XPS", in Practical Surface analysis, 2nd ed., ed. by D. Briggs, M.P. Seah (J. Wiley, 1990), chapter 5

[118] F.J. Himpsel, F.R. McFeely, A. Taleb-Ibrahimi, J.A. Yarmoff, G. Hollinger, "Microscopic structure of the SiO_2/Si interface", in The Physics and Chemistry of SiO_2 and the Si-SiO_2 interface, ed. by C.R. Helms, B.E. Deal, (Plenum Press, New York, 1988), 219

[119] J.M. Hill, D.G. Royce, C.S. Fadley, L.F. Wagner and F.J. Grunthaner, "Properties of oxidized silicon as determined by angular-dependent X-ray photoelectron spectroscopy", Chem. Phys. Lett. **44**, 225 (1976)

[120] F.J. Grunthaner and P.J. Grunthaner, "Chemical and electronic structure of the SiO_2/Si interface", Materials Science Reports **1**, 65 (1986)

[121] D. Schulze, J. Finster, E. Hensel, W. Skorupa, and U. Kreissig, "XPS studies of SiO_2 surface layers formed by oxygen ion implantation into silicon", Phys. Stat. Sol. **A76**, K21 (1983)

[122] G. Holmen, H. Jacobsson, "Ion beam induced oxidation of silicon", Appl. Phys. Lett. **53**, 1838 (1988)

[123] P.D. Augustus, G.D.T. Spiller, M.G. Dowsett, P. Kightley, G.R. Thomas, R. Webb, E.A. Clark, "Cross-sectional Transmission Electron Microscopy and Auger Electron Spectroscopy studies of primary beam damage at the bottom of SIMS craters eroded in Si", in Secondary Ion Mass Spectrometry (SIMS VI), ed. by A. Benninghoven, A.M. Huber, H.W. Werner, (Wiley, Chichester 1988), 485

[124] J.E. Castle, H.D. Liu, J.F. Watts, J.P. Zhang, P.L.F. Hemment, S.M. Newstead, A.R. Powell, T.E. Whall and E.H.C. Parker, "Synthesis of oxides in $Si_{0.5}Ge_{0.5}$ alloy by high dose oxygen ions implantation" presented in Symposium D: Ion Beam Synthesis of Compound and Elemental Layers, European Materials Research Society 1991 Spring Meeting, 27 - 31 May, Strasbourg, France

[125] G.P. Schwartz, G.J. Gualtieri, G.W. Kammlott, B. Schwartz, "An X-ray Photoelectron Spectroscopy study of native oxides on GaAs", J. Electrochem. Soc. **126**, 1737 (1979)

[126] F.J. Grunthaner, P.J. Grunthaner, R.P. Vasquez, B.F. Lewis, J. Maserjian, A. Madhukar, "Local atomic and electronic structure of oxide/GaAs and SiO_2/Si interfaces using high-resolution XPS", J. Vac. Sci. Technol. **16**, 1442 (1979)

[127] S.S. Todorov, E.R. Fossum, "Oxidation of Silicon by a low energy ion beam: experiment and model", Appl. Phys. Lett. **52**, 48 (1988)

[128] J.A. Kilner, "Models of buried layer formation", Vacuum **42**, 391 (1991) and ref. therein

[129] F. Namavar, J.I. Budnick, F.H. Sanchez, H.C. Hayden, "Formation of buried SiO_2 by high dose implantation of oxygen at room and liquid nitrogen temperatures", in Semiconductor-On-Insulator and Thin Film Transistor Technology, ed. by A. Chiang, M.W. Geis, L. Pfeiffer, Mat. Res. Soc. Symp. Proc. Vol. **53**, 233 (1986)

[130] S.S. Todorov, I.R. Chakarov, D.S. Karpuzov, "Low energy ion beam oxidation of silicon surfaces: ballistics, diffusion and chemistry", to be published in Nucl. Instrum. Meth. B (1992)

[131] I.H. Wilson, "Synthesis of dielectric layers in silicon by ion implantation", in Ion Beam Modification of Insulators, ed. P. Mazzoldi, G. Arnold (Elsevier, Amsterdam, 1987), Chapter 7, 245

[132] H. Hahn, R. Juza, "Untersuchungen über die Nitride von Cadmium usw.", Z. Anorg. Allg. Chem. **244**, 122 (1940)

[133] O.H. Johnson, "Germanium and its inorganic compounds", Chem. Rev. **51**, 431 (1952)

[134] T.O. Sedgwick, "Dominant surface electronic properties of SiO_2-passivated Ge surfaces as a function of various annealing treatments", J. Appl. Phys. **39**, 5066 (1968)

[135] see for example: Silicon Molecular Beam Epitaxy, Thin Solid Films **183** (1989)

[136] T. Sawada, H. Hasegawa, "Interface state band between GaAs and its anodic native oxide", Thin Solid Films **56**, 183 (1979)

[137] S.S. Todorov, S.L. Shillinger, E.R. Fossum, "Low-Energy Ion Beam Oxidation of Silicon", IEEE Electron Device letters **EDL-7**, 468 (1986)

[138] D.J. Dumin, E.R. Fossum, S.S. Todorov, "Comparison of the electrical properties of thermal and ion beam oxides", in Materials modification and growth using ion beams, ed. by U. Gibson, A.E. White, P.P. Pronko, Mat. Res. Soc. Symp. Proc. Vol. **93**, 137 (1987)

BIOGRAPHICAL NOTE

Olivier Vancauwenberghe is originally from Saint-Sauveur, a small village near Tournai in Belgium.

He attended secondary school in the Latin-Greek program at the Collège Saint-Julien in Ath, from which he received the Gold Medal for Outstanding Results. He completed his secondary education by a specialization year in Mathematics at the Institut Saint-Louis in Brussels.

He was admitted to the Faculté des Sciences Appliquées (FSA) of the Université Catholique de Louvain (UCL) in Louvain-La-Neuve in September 1982 and obtained his degree of Ingénieur en Science des Matériaux in June 1987.

He was awarded a prestigious fellowship by the Belgian American Educational Foundation (BAEF) to pursue his studies in the United States.

In September 1987, he joined Professor Nicole Herbots in the Department of Materials Science and Engineering at the Massachusetts Institute of Technology (MIT) in Cambridge, MA, to work on his Ph.D. His Ph.D. research focused on several theoretical and experimental aspects of the growth of semiconductor-based epitaxial and oxide films from low energy ion beams. He completed his Ph.D. in September 1991.

During his Ph.D., Olivier Vancauwenberghe received three fellowships recognizing his academic merits and the quality of his research: the Materials Processing Center fellowship, the DeCorte fellowship and an outstanding predoctoral fellowship from IBM.